# Computational Methods for Reconstruction of Nanoscale Strain Fields via Multi-Grain Bragg Coherent Diffraction Imaging

Submitted in partial fulfillment of the requirements for

the degree of

Doctor of Philosopy

in

Materials Science and Engineering

Matthew J. Wilkin

B.S., Nuclear Engineering, Texas A&M University
M.S., Materials Science and Engineering, Carnegie Mellon University

Carnegie Mellon University
Pittsburgh, PA

May 2022

**Abstract**

Bragg coherent diffraction imaging (BCDI) has the potential to provide significant insight into the structure-properties relationship for crystalline materials by imaging, with nanoscale resolution, three-dimensional (3D) strain fields within individual grains and nanoparticles. Recent methods for coupling reconstructions from several peaks to determine the full elastic strain tensor have been developed and applied to synthetic data, but have not been applied to experimental data. Using a coupled genetic reconstruction algorithm, this work presents reconstructions of an experimental data set and demonstrates improvements in the ability to resolve vector-valued displacement fields internal to the particle. For experimental data, reconstructions from the coupled Bragg peak algorithm show improvements over the non-coupled independent reconstruction method of 5% in terms of accuracy and 53% in terms of consistency. Additionally, this work presents the ability of this genetic algorithm to accurately reconstruct displacement fields about dislocations, showing a success rate of 90%. Finally, this work demonstrates a method for reconstructing neighboring grains simultaneously, improving the reconstructions by 13.5% in terms of reconstruction accuracy, and laying the foundation for polycrystal BCDI.

# ACKNOWLEDGEMENTS

This research was funded by the U.S. Department of Energy, Office of Science under a Basic Energy Sciences grant, award number DESC0019096. This research used resources of the Advanced Photon Source, a U.S. Department of Energy (DOE) Office of Science User Facility operated for the DOE Office of Science by Argonne National Laboratory under Contract No. DE-AC02-06CH11357. I wish to thank My advisor and committee chair, Anthony D. Rollett, for his constant support and stimulating conversation. My thanks to my committee members, Prof. Robert M. Suter, Prof. Marc DeGraef, and Prof. Elizabeth Holm of Carnegie Mellon University, as well as Dr. Stephan Hruszkewycz of Argonne National Laboratory, for their time and consideration in making this a worthwhile piece of research. Thanks to Siddharth Maddali, who held my hand from day one. I would like to thank the members of the Rollett group for their many small contributions to my work. I would like to thank my family for putting up with my nonsense and my wife Amber for her love during stressful times and for bringing me cups of water while I wrote. Lastly, I give thanks to the Lord God, whose goodness and mercy have surely followed me all the days of my life.

*Matthew J. Wilkin May 2022*
*Pittsburgh, PA*

**List of Publications Resulting from this Work**

The following papers related to the work presented in this thesis have been published or submitted:

1. Wilkin, M. J., Maddali, S., Hruszkewycz, S. O., Pateras, A., Sandberg, R. L., Harder, R., ... & Rollett, A. D. (2021). Experimental demonstration of coupled multi-peak Bragg coherent diffraction imaging with genetic algorithms. Physical Review B, 103(21), 214103.

# TABLE OF CONTENTS

# LIST OF TABLES

# LIST OF FIGURES

# CHAPTER I

# Introduction

## 1.1 Motivation and Introduction

There has been a recent push in Materials Science, outlined in several DOE reports, for lightweight, high-strength structural materials for applications such as energy and aerospace [1–4]. Initiatives such as the Materials Genome Initiative focus on illuminating in greater detail the structure-property relationship in such materials through the use of first-principles and ab-initio calculations, as well as mesoscale simulations. This work seeks to address these goals through the development of x-ray diffraction tools for high-resolution strain imaging. In particular, we propose the study of slip transmission across grain boundaries through a novel multi-grain Bragg coherent diffraction imaging (BCDI) experiment and a multi-grain reconstruction routine for the handling of complicated BCDI datasets.

Bragg coherent diffraction imaging is an experimental tool for non-destructive imaging of the shape and displacement fields of a 3D crystal from a coherent Bragg peak [5]. Recent work has demonstrated its viability for the study of dislocation dynamics, stacking faults, and twinning at the nanoscale through reconstruction of a single Bragg peak [6–13]. Tools such as Laue diffraction [14] and High Energy Diffraction Microscopy (HEDM) [15,16] have demonstrated the potential to locate neighboring grains and nanoparticles of interest on the length scales required for BCDI, opening the door for multi-grain experiments, where grain boundary phenomena can be studied in 3D with unrivaled resolution. With the enhanced x-ray brightness and coherence from upcoming fourth-generation synchrotrons, this technique will be capable of achieving significant improvements in throughput and spatial resolution, with the potential to help validate theoretical models on atomistic and mesoscopic length

scales [17–19].

The phase retrieval process applied to a BCDI dataset measured at a single Bragg reflection returns a three-dimensional image sensitive to a single component of the lattice distortion field, from which the corresponding strain projection can be calculated [20, 21]. Three or more BCDI datasets from non-colinear Bragg reflections contain enough information to determine the entire displacement vector field, and by extension, the full six-component strain tensor [22, 23]. Though this has typically been accomplished through independent reconstruction of each Bragg Peak, recently developed phase retrieval methods propose coupling multiple BCDI datasets [24–26], sharing information among peaks within the image reconstruction algorithm. While reconstructing Bragg peaks independently is more straightforward in practice, coupling reconstructions from multiple Bragg peaks from the same crystal has the potential to significantly reduce the error of the retrieved strain field and crystal shape by increasing the number of constraints on the reconstructed object. These methods have proven effective in the reconstruction of simulated datasets, but as yet, none have been used on experimental data, which typically present more challenges than simulated data [27]. Demonstration of such a method on experimental data is vital for turning these coupled reconstruction algorithms into robust experimental tools which can, in turn be used to characterize grain boundary strain.

Once this has been accomplished, an extension can be made to simultaneous reconstruction of neighboring grains, where phase retrieval on each grain is constrained at the interface. Grain boundary voxels are typically the lowest fidelity voxels in a BCDI reconstruction, due to imprecise nature of shape-function definition during phase retrieval. While this issue has not been an issue during the study of internal defects, it becomes an essential problem during the the study of grain boundaries. To get the most accurate reconstruction of the grain boundary, a new approach must be defined. In this work, new approaches are detailed based on the following hypotheses.

## 1.2 Hypotheses

1. It is hypothesized that coupling the reconstructions of multiple Bragg datasets from the same grain, with the help of a genetic algorithm, will improve the reconstruction

accuracy of experimental data by 10% and reconstruction consistency by 20%.

2. It is hypothesized that the same routine, when applied to datasets with dislocations, will improve the success rate for dislocation reconstruction by 20%

3. It is hypothesized that coupling the reconstructions of two neighboring grains and applying shape and displacement continuity conditions at the grain boundary will improve the reconstructions of both by 10% in all confidence metrics, including accuracy in Fourier Space, accuracy in Real space, and consistency between reflections.

## 1.3 Contribution to Field

This work will represent a significant contribution to the coherent x-ray diffraction field in the form of tools which provide higher fidelity data analysis than any in current use. The implementation of genetic algorithms for coupled phase retrieval will provide higher multi-peak reconstruction confidence and represent a significant step forward from independent reconstruction. The reconstruction of the full displacement field in two neighboring crystals has not been attempted until now, and the proposed algorithm here is the first of its kind. It is expected that this work will provide a foundation on which to build for others in the community and will mark an important first step toward the realization of BCDI as a true polycrystal characterization tool. BCDI experiments have focused on isolated nanocrystals to this point and have not been used to study interactions at grain boundaries. The tools developed herein promise to make such studies a reality, allowing for experimental validation of theoretical plasticity models for atomistic simulation tools.

# CHAPTER II

# Background

## 2.1 Need for 3D Validation of Plasticity Models

Structural materials tend to be crystalline, meaning they plastically deform by the movement of dislocations through slip. Thus, any discussion of material strength must include a discussion of dislocation dynamics [28,29]. A dislocation is a half-plane of atoms inserted into a crystalline volume. Dislocations can be characterized by two vectors, the dislocation line vector: $\mathbf{l}$ and the Burgers vector $\mathbf{b}$. $\mathbf{l}$ is the line along the half plane of atoms from the surface of the crystal to the edge of the half plance. In Fig. 2.1, $\mathbf{l}$ would be perpendicular to the plane of atoms in the diagram. The Burgers vector $\mathbf{b}$ is defined as the displacement caused by a dislocation in a closed loop within the crystal volume about the dislocation center. Dislocations exist in three types: edge, screw, and mixed. In edge dislocations, $\mathbf{l}$ is perpendicular to $\mathbf{b}$. In screw dislocations, $\mathbf{l}$ is parallel to $\mathbf{b}$. Most dislocations, however exhibit a mixed character, containing parts of both edge and screw dislocations.

Dislocations were first postulated to account for plastic deformation in crystals. Crystals deform plastically as atomic planes slide past each other in a process known as "slip." Slip in a perfect crystal requires the simultaneous and coordinated motion of all atoms in a lattice plane. This means that all bonds must be broken for a plane to slip by a single lattice spacing. The predicted shear strength of such slip is, however, several orders of magnitude larger than the experimentally observed shear strength, leading scientists to seek another answer. Independently, Orowan, Polanyi, and Taylor accounted for the discrepancy in theoretical and measured displacement by the presence of dislocations [28, 30–32]. Today, we know that slip occurs as a dislocation travels along a slip plane throughout a crystal

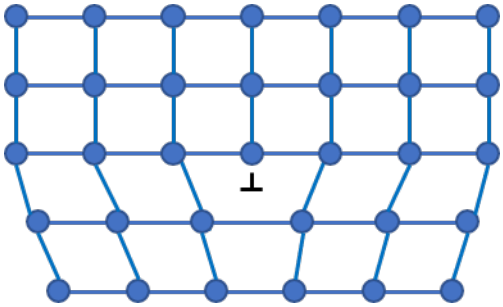

Figure 2.1: Schematic of an edge dislocation

volume. It can be seen in 2.1 that the number of bonds which must be broken for a dislocation to travel one Burger's vector length is one per unit length $\mathbf{l}$, a number several orders of magnitude smaller than what would need to be broken in the coordinated slip case, where all atoms shift at once.

Slip occurs on specific sets of planes in specific materials. In order for slip to occur on a particular plane, the Burger's vector must be in the plane, according to:

$$\mathbf{b} \cdot \mathbf{n} = 0 \tag{2.1}$$

where $\mathbf{n}$ is the plane normal. Together, a Burger's vector and crystallographic plane normal make up a slip system. For slip to occur on a particular slip system, a characteristic shear stress is required, called the critical resolved shear stress (CRSS). The shear stress, resolved on a slip plane in the slip direction can be found by the following relation

$$\tau = \frac{F}{A} \cos\phi \cos\lambda, \tag{2.2}$$

where $F$ is an applied force, $A$ is the cross-sectional area of the sample orthogonal to $F$, $\phi$ is the angle between $F$ and the slip plane normal, and $\lambda$ is the angle between $F$ and the slip direction. $\cos\phi\cos\lambda$ is known as the Schmid factor and can be used to determine which slip systems are active, given an applied load. When the resolved shear stress ($\tau$) exceeds the CRSS for a slip system, slip occurs. In each crystal structure, slip is preferred on a specific family of slip systems, corresponding to those with the lowest CRSS. Under a uniform stress, the slip system which will be activated first is the one for which the resolved

shear stress is the highest.

While the movement of dislocations is fairly well understood individually and within crystal volumes, gaps remain where dislocations interact with grain boundaries. There are numerous discrepancies in the literature as to the nature and energy requirements of slip transmission. The classical understanding of slip transmission across grain boundaries is presented by Livingstone and Chalmers [33] and elaborated on by Shen [34]. These efforts propose that slip transmission can be characterized by the following formalism:

$$\tau b_1^2 \geq \tau_{pass} b_1^2 = \omega E_{gb} b_1 + \alpha G (\Delta b)^2, \tag{2.3}$$

where $\tau$ is the resolved shear stress, $\tau_{pass}$ is the critical stress for transmission of a dislocation through a grain boundary, $b_1$ is the Burgers vector of the incoming dislocation, $E_{gb}$ is the grain boundary energy, $G$ is the shear modulus, $\Delta b$ is the difference in Burgers vector across the grain boundary, $\omega$ captures the energy lost in the interaction of the dislocation with the grain boundary, and $\alpha$ is a material dependent coefficient. There is a significant amount of disagreement, however, as to which terms are the most important. Some suggest that grain boundary geometry predicts slip transmission while others cite grain boundary energy and type as the determining factors [17, 34, 35]. Still others insist that the first term dominates and that transmission depends primarily upon grain boundary energy and character. Molecular Dynamics simulations [36], [37] have been performed to predict the motion of dislocations at grain boundaries, but discrepancies still exist. Given the state of uncertainty surrounding slip transmission, the need for true 3D experimental validation of dislocation movement at grain boundaries is crucial. In order to validate these models, it is necessary to observe the movement of dislocations in three dimensions at grain boundaries and we believe that Bragg coherent diffraction imaging is in a unique place to provide such data.

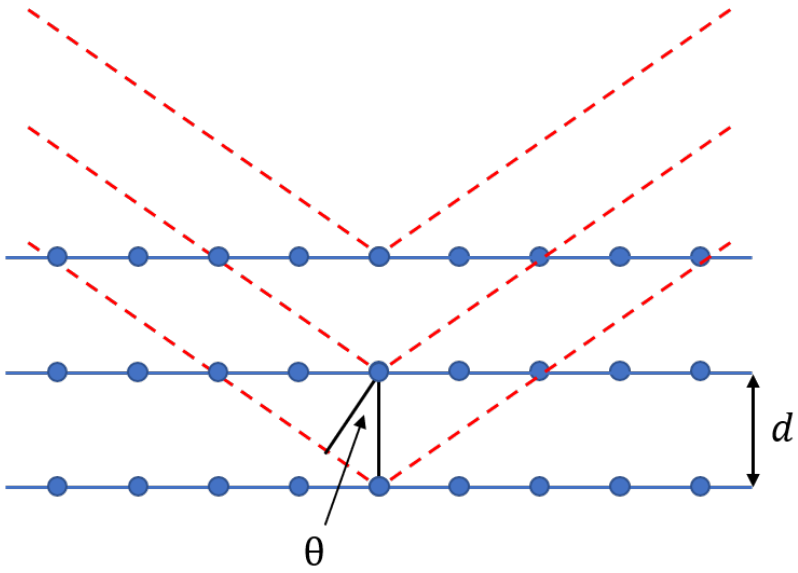


Figure 2.2: Bragg's Law. Diffraction occurs when waves scattering at different planes in a crystalline lattice remain in phase, constructively interfering with one another to produce a diffraction pattern in the far field.

## 2.2 Bragg Coherent Diffraction Imaging

### 2.2.1 Bragg's Law and Crystalline Diffraction

A common tool for characterizing crystalline materials is x-ray diffraction, wherein x-rays interacting with an ordered lattice constructively interfere in certain crystal directions to produce a diffraction peak. When an incident monochromatic x-ray beam illuminates a crystal, the scattering waves will constructively interfere only when scattering off crystallographic planes in the Bragg condition, which is depicted in Fig. 2.2.

Bragg's Law is defined as

$$n\lambda = 2d\sin\theta, \tag{2.4}$$

where $\lambda$ is the x-ray wavelength, $\theta$ is the angle seen in Fig. 2.2, $n$ is an integer and $d$ is the lattice spacing. Thus, if the wavelength of the incoming beam is known, as well as the lattice parameter, the Bragg condition is determined merely by the angle of diffraction $\theta$. Assuming a monochromatic, coherent incoming plane-wave and detection in the optical far-field limit, this scattering can be described by

$$\mathbf{Q} = \mathbf{k}_f - \mathbf{k}_i \tag{2.5}$$

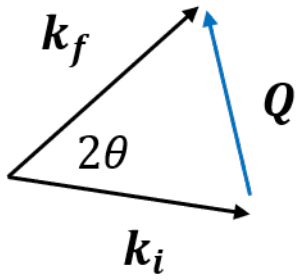


Figure 2.3: Pictorial derivation of the scattering vector **Q**

where **Q** is the scattering vector, $\mathbf{k}_i$ the incident beam direction, and $\mathbf{k}_f$ the exit beam direction, with magnitude $\frac{2\pi}{\lambda}$. When the Bragg condition is met, **Q** is equal to a crystallographic plane-normal $\mathbf{G}_{hkl}$. Constructive interference necessary for diffraction only occurs when interacting waves are in phase, meaning the wave functions are shifted from one another by an integer multiple of $2\pi$. To calculate the phase difference between waves scattering off different lattice planes (same **Q**) at points $\mathbf{x}_1$ and $\mathbf{x}_2$ we find the path length difference along **Q** between the two waves. A diagram of two such scattering events can be seen in Fig. 2.4.

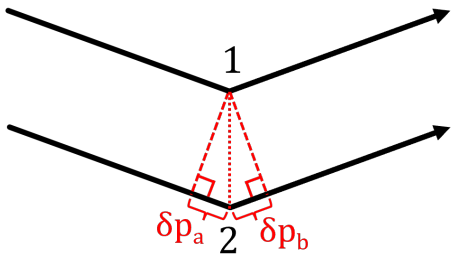


Figure 2.4: Diagram of two neighboring scattering events.

The difference between the path length to a far-away detector through point 1 and that through point 2, according to the diagram, is given as

$$\Delta p = \delta p_a + \delta p_b \tag{2.6}$$

The phase shift is thus

$$\Delta\phi = 2\pi\frac{\Delta p}{\lambda} = \phi_2 - \phi_1 = \mathbf{Q}\cdot(\mathbf{x}_2 - \mathbf{x}_1), \tag{2.7}$$

where $\phi_1$ and $\phi_2$ are the respective phases of waves 1 and 2, and $\mathbf{x}_1$ and $\mathbf{x}_2$ are the spatial positions of the two scattering events. It can be seen that, for scattering events on crystal planes in the Bragg condition, $\Delta p$ will be an integer multiple of $\lambda$, causing them to remain in phase with each other and allowing their amplitudes to add. On any planes not in the Bragg condition, $\Delta p$ is not an integer multiple of the wavelength, and the waves destructively interfere, resulting in no diffraction.

The Born approximation can be used to define the amplitude of a scattered wave off a finite crystal, and is given as

$$\hat{\psi}(\mathbf{Q}) = \int_{V_c} d^3\mathbf{x}\, \rho(\mathbf{x})\, e^{i\mathbf{Q}\cdot\mathbf{x}}. \tag{2.8}$$

where $V_c$ is the coherence volume, and $\rho(\mathbf{x})$ is the electron density at position $\mathbf{x}$. It can be seen that $\hat{\psi}(\mathbf{Q})$ is the Fourier transform (FT) of $\rho(\mathbf{x})$. It is this relationship between the amplitude and electron density which is of greatest interest to those conducting coherent diffraction experiments. If we can find this complex Fourier-space amplitude, we can know the electron density distribution in a crystal, and thus its defect structure.

The coherence volume $V_c$ determines the maximum volume of the incident beam in which diffraction can be considered coherent. The coherence length in the longitudinal direction (parallel to $\mathbf{Q}$) is the propagation distance over which the wave can be assumed coherent and is typically estimated by

$$L_c = \frac{\lambda^2}{\Delta\lambda}, \tag{2.9}$$

where $\lambda$ and $\Delta\lambda$ are the wavelength and bandwidth of the source. The calculation of the horizontal and vertical transverse coherence lengths is more complicated and is out the scope of this work. For now it is sufficient to assume that scattering occurring in a crystal smaller than $L_c$ in all dimensions will be considered coherent.

### 2.2.2 Bragg Coherent Diffraction Imaging and Phase Retrieval

Bragg Coherent Diffraction Imaging (BCDI) is a non-destructive three-dimensional x-ray imaging tool first demonstrated in 2001 by Robinson et al. [38]. In BCDI, a compact single crystal is illuminated by a nominally monochromatic and spatially coherent x-ray beam

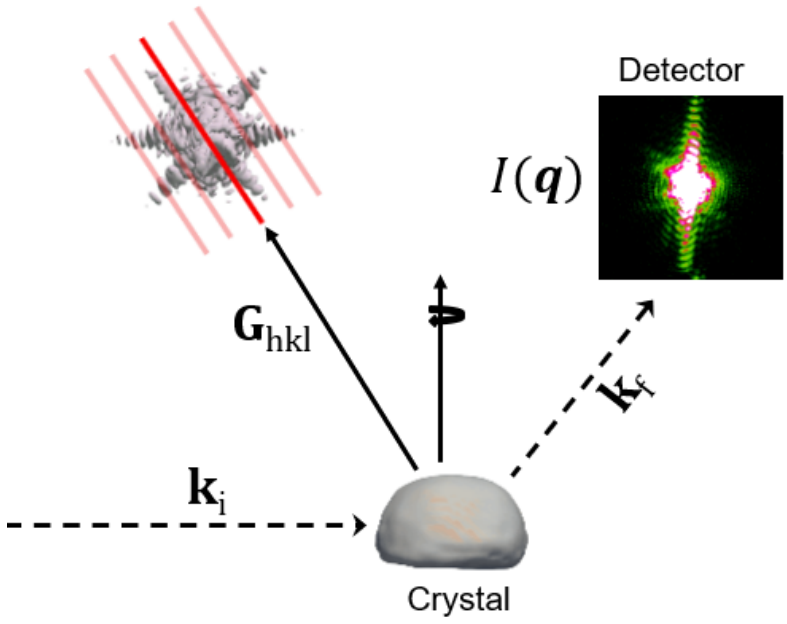


Figure 2.5: Diagram of general BCDI setup

such that $V_c$ in E1. 2.8 is larger than the crystal volume. As the crystal is rotated through one of its Bragg conditions, corresponding to reciprocal lattice vector $\mathbf{G}_{hkl}$, the 3D coherent diffraction pattern is sampled in a series of detector images with the detector in the optical far-field or Fraunhofer regime , as seen in Fig. 2.5 [21].

In this limit, the scattered amplitude, $\hat{\psi}(\mathbf{q})$, with $\mathbf{q} = \mathbf{Q} - \mathbf{G}_{hkl}$ being the deviation from the nominal Bragg condition in reciprocal space, can be approximated as the Fourier Transform (FT) of the exit wave field at the location of the particle.

The real-to-reciprocal space relationship can be denoted in shorthand as:

$$\hat{\psi}(\mathbf{q}) = \mathrm{FT}\left[\psi(\mathbf{x})\right] \tag{2.10}$$

Given that BCDI measurements consist of pixelated detector images measured at regular angular intervals, the fields $\psi(\mathbf{x})$ and $\hat{\psi}(\mathbf{x})$ are discrete and span a finite range in $\mathbf{x}$ and $\mathbf{q}$, and we designate this discretization (or voxelization) of these spaces with the subscript $n$, (*i.e.* $\mathbf{x}_n$). Thus, we define the discrete complex-valued sample exit field corresponding to a given Bragg peak as

$$\psi(\mathbf{x}_n) = \rho(\mathbf{x}_n)\, e^{2\pi i \phi(\mathbf{x}_n)}. \tag{2.11}$$

Due to limits in x-ray flux, it is not possible to measure large enough $\mathbf{q}$ to achieve atomic resolution, meaning voxel dimensions are typically on the order of tens of nanometers. Thus, $\psi(\mathbf{x}_n)$ in Eq. 2.10 is a continuum approximation of $\rho(\mathbf{x})$ in Eq. 2.8 with each position $\mathbf{x}_n$ representing a box in the crystal containing thousands of atoms. The amplitude $\rho(\mathbf{x}_n)$ corresponds to the material density at $\mathbf{x}_n$, and the phase, $\phi(\mathbf{x}_n)$, is a projection along the scattering vector $\mathbf{G}_{hkl}$ of the mean displacement $\mathbf{u}(\mathbf{x}_n)$ of all atoms in the volume with respect to the unperturbed lattice :

$$\phi_{hkl}(\mathbf{x}_n) = \mathbf{u}(\mathbf{x}_n) \cdot \mathbf{G}_{hkl}. \tag{2.12}$$

The measured intensity of a Bragg peak is related to $\hat{\psi}(\mathbf{q})$ by eq. 2.13.

$$I(\mathbf{q}) = |\hat{\psi}(\mathbf{q})|^2. \tag{2.13}$$

Though $\hat{\psi}(\mathbf{q})$ is complex, the phase information is lost during the measurement, and $\psi(\mathbf{x})$ cannot be recovered from $I(\mathbf{q})$. This is known as the phase problem. To find the phase and amplitude of $\psi(\mathbf{x})$, it is necessary to recover the lost phases of $\hat{\psi}(\mathbf{q})$ via iterative phase retrieval.

Phase retrieval was conceived by an observation from David Sayre [39], when he acknowledged that the Nyquist-Shannon sampling theorem [40] could be applied to x-ray scattering. He proposed that, by oversampling a coherent diffraction pattern at twice the Nyquist frequency ( $f_N = \frac{1}{D}$, where D is the crystal size), the phase can be recovered. To fully understand this, it is helpful to think of the phase problem as a set of nonlinearly coupled equations relating $\hat{\psi}(\mathbf{q})$ to $\hat{\psi}(\mathbf{x})$. We will rewrite Eq. 2.10 as a DFT sampled at the Nyquist frequency:

$$\hat{\psi}(q) = \sum_{x=1}^{N} \psi(x)\, e^{iqx/N} \quad q = 1, ..., N, \tag{2.14}$$

where $x$ and $q$ are pixel coordinates in real space and Fourier space, discretized from 1 to $N$.

It can be seen that while there are $N$ equations, there are $2N$ unknowns because neither the phase nor amplitude of $\psi(x)$ is known. Thus, the system of equations is underdetermined by a factor of 2 and cannot be uniquely solved. To fully determine the system, we sample $\hat{\psi}(q)$ at twice the Nyquist frequency, such that

$$\hat{\psi}(q) = \sum_{x=1}^{N} \psi(x)\, e^{iqx/(2N)} \quad q = 1, ..., 2N. \tag{2.15}$$

Because the real space array must contain the same number of pixels as the Fourier space one, we introduce a function $g(x)$, given as

$$g(x) = \begin{cases} \psi(x), & 0 < x \leq N/2, \\ 0, & N/2 < x \leq N, \end{cases} \tag{2.16}$$

and insert it into Eq. 2.15 as

$$\hat{\psi}(q) = \sum_{x=1}^{2N} g(x)\, e^{iqx/(2N)} \quad q = 1, ..., 2N. \tag{2.17}$$

It can be seen that oversampling introduces a zero-density region in real space such that $\psi(x)$ only spans half the array. This zero-density requirement is known as the support and determines the bounds of the crystal volume in the reconstruction [41, 42]. By setting half the pixels in $g(x)$ to zero, we eliminate half of the unknowns, fully determining the system of equations. There are now $2N$ equations, $N$ unknown phases, and $N$ unknown amplitudes, so Eq. 2.17 can be solved. A 2D schematic of this oversampling phenomenon can be seen in Fig. 2.6

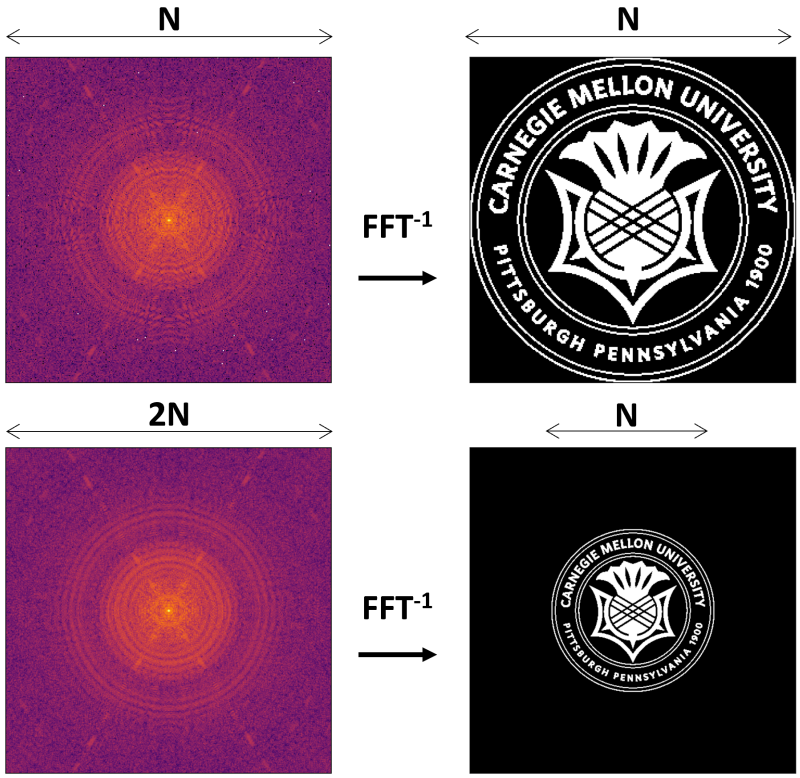


Figure 2.6: Diagram showing the effect of oversampling on the size of the object in the real-space array. Oversampling by a factor of 2 in Fourier space introduces a zero-density region on either side of the object in real space.

Gerchberg and Saxton developed the first phase retrieval algorithm from Sayre's observation, known as the Gerchberg-Saxton algorithm [43]. In this algorithm, an initial guess is made for $\hat{\psi}(\mathbf{q})$ and the object is iteratively tansformed between real space and Fourier space enforcing constraints in both domains until convergence.

The Gerchberg-Saxton algorithm was the basis for two of the most important phase retrieval algorithms, developed by James Fienup: error reduction (ER) [44] and hybrid input-output (HIO) [45]. The ER algorithm can be seen in Fig. 2.7 and consists of the following steps:

1. Make an initial guess for the phase and amplitude of $\psi_i(\mathbf{x})$
2. FT the $\psi_i(\mathbf{x})$ to get $\hat{\psi}_i(\mathbf{q})$
3. Reset the amplitude of $\hat{\psi}_i(\mathbf{q})$ to the measured amplitude $\sqrt{I(\mathbf{q})}$
4. IFT $\hat{\psi}_i(\mathbf{q})$ to get $\psi_i'(\mathbf{x})$

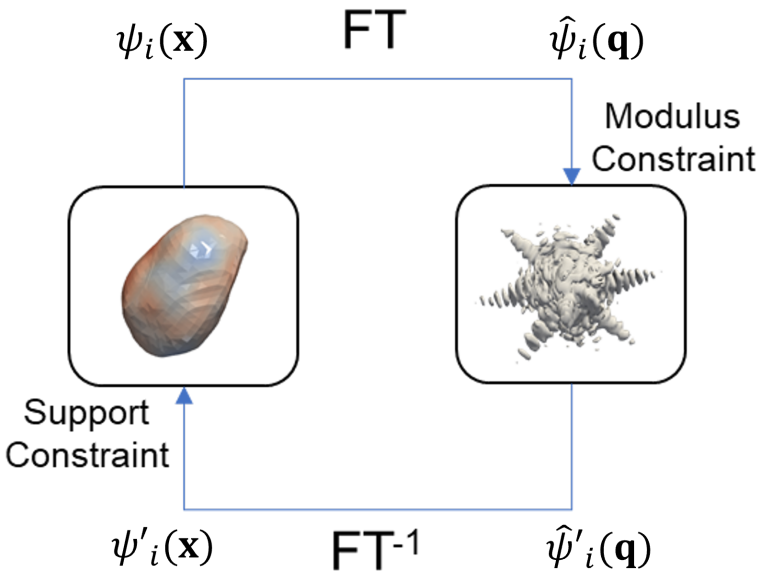


Figure 2.7: Schematic of Fienup's Error Reduction algorithm.

5. Apply support to $\psi'_i(\mathbf{x})$ give new object guess $\psi_{i+1}(\mathbf{x})$

We define a support function which constrains the crystal volume in the sample domain such that

$$\psi_{i+1}(\mathbf{x}) = \begin{cases} 0 & x \notin S \\ \psi'_i(\mathbf{x}) & x \in S \end{cases} \tag{2.18}$$

Over the course of many ER iterations, the support function is allowed to shrink by a process called 'shrinkwrap' [46], wherein the object amplitude in real space, $|\psi(\mathbf{x})|$ is convolved with a Gaussian $f$,

$$\xi(\mathbf{x}) = (f * |\psi(\mathbf{x})|), \tag{2.19}$$

and thresholded, according to

$$S = \begin{cases} 1, & \text{if } \xi(\mathbf{x}) > (th * \xi_{max}), \\ 0, & \text{otherwise,} \end{cases} \tag{2.20}$$

where $th$ is the threshold value as a fraction of the maximum value in $\xi(\mathbf{x})$. ER is repeated

until the solution converges with respect to the error metric $\chi^2$, given as

$$\chi^2 = \sum_{\mathbf{q}} \left( \sqrt{I(\mathbf{q})} - |\hat{\psi}(\mathbf{q})| \right)^2, \tag{2.21}$$

which is a measure of the difference between the forward-modeled modulus and the measured modulus. ER is equivalent to a steepest descent method and necessarily converges, but it has a strong tendency to become trapped in local minima [47]. To deal with these local minima issues, Fienup [48] developed the hybrid input-output algorithm, which consists of the following steps:

1. Make an initial guess for the phase and amplitude of $\psi_i(\mathbf{x})$
2. FT the $\psi_i(\mathbf{x})$ to get $\hat{\psi}_i(\mathbf{q})$
3. Reset the amplitude of $\hat{\psi}_i(\mathbf{q})$ to the measured amplitude $\sqrt{I(\mathbf{q})}$
4. IFT $\hat{\psi}_i(\mathbf{q})$ to get $\psi_i'(\mathbf{x})$
5. Initialize next iteration $\psi_{i+1}(\mathbf{x})$ according to

$$\psi_{i+1}(\mathbf{x}) = \begin{cases} \psi_i'(\mathbf{x}), & \text{if } \psi(\mathbf{x}) \in \mathrm{S}, \\ \psi_i(\mathbf{x}) - \beta\psi_i'(\mathbf{x}), & \text{otherwise}, \end{cases} \tag{2.22}$$

where $\beta$ is a constant typically set to 0.9. In HIO, every output $\psi_i'(\mathbf{x})$ satisfies the Fourier space constraints, but there is no requirement that it satisfies the real space constraints. HIO allows pixels outside the support to evolve over several iterations, moving the solution parallel to the gradient and potentially jogging the solution out of local minima. Using HIO in conjunction with ER is a powerful tool for phase retrieval, as ER converges toward a local minimum and HIO increases the likelihood that the final solution is the global minimum. Together, HIO, ER, and shrinkwrap make up the foundation of the methods presented here, together with a strategy for coupling information from multiple Bragg peaks during the reconstruction process.

BCDI has been used to measure dislocation movement in battery particles, phase transitions, twin boundary evolution, catalysis, and FIB damage fields [49–55]. In these cases,

BCDI has mainly served as an imaging tool. By measuring only one Bragg reflection, thereby showing only a projection of the lattice displacement, single-reflection BCDI does not tell the whole story. The eventual goal is to push BCDI to be a true polycrystal characterization tool and to image neighboring grains to address issues such as those discussed in section 2.1. To truly answer the questions of interest, it will be necessary to retrieve not just a projection of the lattice displacement, but all components.

### 2.2.3 Multi-Peak BCDI

While reconstructing a single Bragg peak can provide a projection of the lattice displacement along the scattering vector, collecting three or more non-colinear Bragg reflections allows for the recovery of the full six-component elastic strain tensor in the crystal. For each peak, the phase value $\phi_{hkl}(\mathbf{x}_n)$, is related to the displacement field $\mathbf{u}(\mathbf{x}_n)$ by Eq. 2.12. As seen in Fig. 2.9, as the spacing between two lattice planes shifts relative to the reference position (corresponding to the unstrained crystal), the path length difference ($\Delta p$) between waves diffracting off consecutive planes is no longer an integer multiple of the wavelength. This results in a phase shift in the exit wave-front.

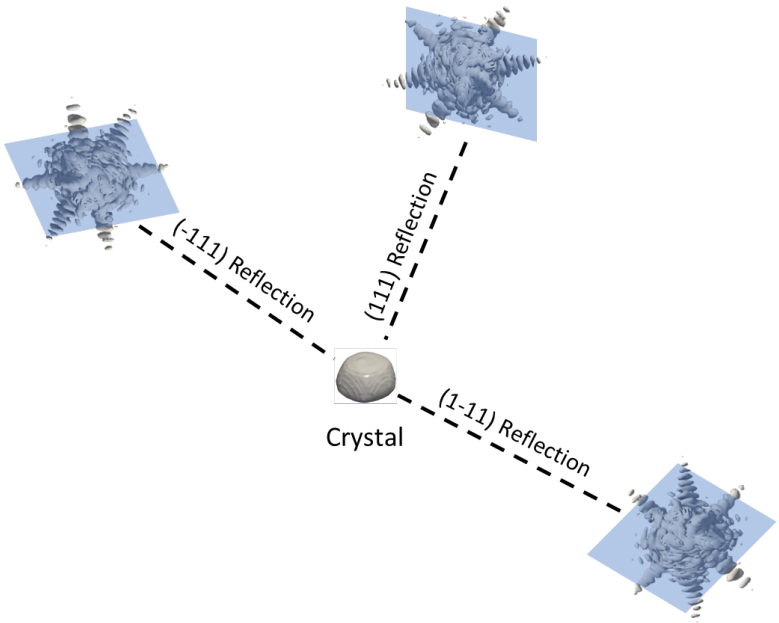


Figure 2.8: Diagram showing diffraction patterns of multiple reflections in Multi-peak BCDI

Because the distance between atoms within each plane does not affect $\Delta p$, BCDI is only

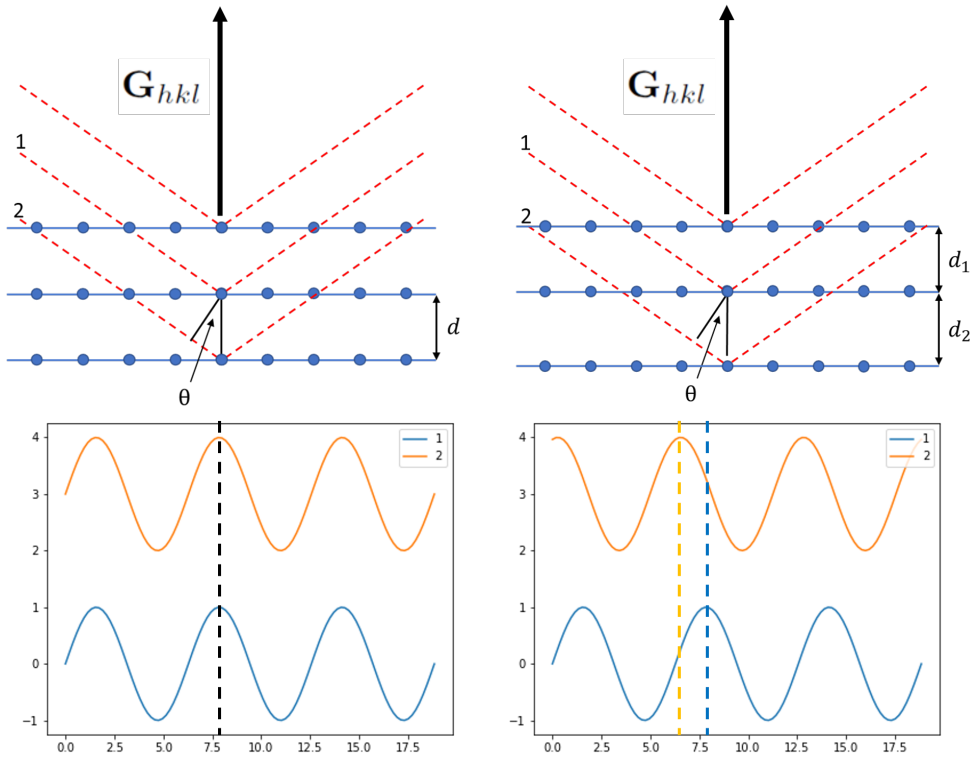


Figure 2.9: Diagram showing the path-length difference between waves scattering at two points along $\mathbf{G}_{hkl}$

sensitive to displacements along $\mathbf{G}_{hkl}$. To recover the full displacement vector at each voxel, multiple Bragg peaks are needed. As there are three components of $\mathbf{u}$, three phases from non-colinear reflections are required to fully constrain the problem. An example of this can be seen in Eq. 2.23.

$$\begin{bmatrix} \mathbf{G}_{111} \\ \mathbf{G}_{1\bar{1}1} \\ \mathbf{G}_{\bar{1}11} \end{bmatrix} \mathbf{u}_n = \begin{bmatrix} \phi_{n,111} \\ \phi_{n,1\bar{1}1} \\ \phi_{n,\bar{1}11} \end{bmatrix}, \tag{2.23}$$

where the subscript $n$ denotes a voxel in the reconstructed array and the reflections [111],[1$\bar{1}$1], and [$\bar{1}$11] were used. Hofmann and Newton [56, 57] demonstrated the benefit of using more than three Bragg peaks to over-constrain the crystal shape and displacement fields. After all Bragg peaks are reconstructed independently, $\mathbf{u}_n$ is found using a least-squares optimization,

$$L_n = \sum_{j=1}^{J} (\mathbf{u}_n \cdot \mathbf{G}_{j,hkl} - \phi_{j,hkl,n})^2, \tag{2.24}$$

where $j$ denotes a particular Bragg reflection, and $J$ is the total number of Bragg reflections. While this method works well if the datasets from each Bragg reflection are of good quality, problems may arise when this is not the case. Issues such as particle drift and an imperfect beam can make datasets difficult to reconstruct. When the results are combined at the end, it is likely that artifacts from the dataset will propagate to the final solution. Because the datasets contain overlapping information, it should be possible to couple them during the reconstruction process, allowing the reconstructions to pass information between each other.

Newton et al. proposed the first such coupling algorithm by interleaving a series of HIO steps between separate crystals and combining the results after each step. In this algorithm, each peak is put through one iteration of HIO. After all peaks have completed this step, the least-squares routine described in 2.24 is used to calculate $\mathbf{u}_n$. This $\mathbf{u}_n$ is then projected along the $\mathbf{G}_{hkl}$ vectors to give an updated guess for $\phi_{hkl,n}$. This method was demonstrated on a simulated dataset, which was simplified to be a cube with a symmetric strain field. Additionally, this method requires that the support be known *a priori*, as no shrinkwrap is applied. While this demonstrated an important first step, these simplifications make it unwieldy for experimental datasets, where the support is not known. Additionally, this algorithm required thousands of iterations to converge. The least-squares calculation is computationally costly on large 3D arrays, so repeating this step after every HIO step makes the method functionally difficult to handle.

To address these issues, Gao et al. demonstrated an approach for reconstructing multiple peaks based on the bisection method. This method combines the results from several Bragg reflections intermittently throughout the phase retrieval process and showed the effectiveness of doing so for reconstructing highly strained crystals. Their approach the electron density and the displacement separately and updates them by combining the amplitudes and phases respectively at specified iterations. They found that coupling reconstructions of multiple peaks from a grain containing a dislocation could improve the rate at which the phase was successfully reconstructed for each peak.

These works have been limited to simulated data, which is simpler to reconstruct than experimental data. To fully trust the efficacy of such methods, it is necessary to demonstrate

them on experimental data. This work demonstrates the first reconstruction algorithm to be used on experimental data and shows its advantages over the current state of the art for multi-peak BCDI.

### 2.2.4 Multi-Grain BCDI

Multi-Grain BCDI is a nascent technique in the BCDI community. Several groups have reconstructed twins using single peak BCDI but none, to our knowledge, have collected multiple peaks from neighboring grains and assembled the corresponding displacement and strain fields. Many challenges exist in the implementation of Multi-Grain BCDI. The first is the required grain size for BCDI beamlines. The size of crystal that can be measured using BCDI is determined primarily by a value called coherence length from Eq. 2.9, which is the maximum distance between the furthest scattering events in a crystal where the exit wave-field can be considered coherent scattering.

The coherence length is $\sim$ 235 nm at 1-ID and $\sim$ 1$\mu$m at 34-ID-C. Few functional materials have grain sizes on this scale [23] and collecting high-fidelity EBSD patterns of such samples can be challenging. If EBSD is successfully captured, preserving these orientations and transforming them into the beamline reference frame is not trivial and has never been successfully accomplished at 34-ID-C. If one were able to orient the crystals, problems remain with aligning them after reconstruction. BCDI diffraction patterns contain only information from a single grain, and though the orientation of each grain can be known, the relative position of one grain with respect to the other cannot be determined with the resolution required for particles smaller than 1$\mu$m.

Nevertheless, the potential to study 3D strain and stress fields at grain boundaries is enticing and the resolution provided by BCDI unparalleled. In this work, we present techniques for locating, reconstructing, and aligning neighboring grains such that multi-grain BCDI becomes imminently feasible.

# CHAPTER III

# Experimental Methods

Before the novel reconstruction methods are presented, we must take stock of the experimental methods required for the collection of multi-peak and multi-grain BCDI datasets. In order to collect such datasets, it is necessary to be able to orient crystals at the beamline. The two beamlines where multi-peak BCDI has been demonstrated are 1-ID-E and 34-ID-C at the Advanced Photon Source. The 1-ID-E beamline is capable of both High Energy Diffraction Microscopy measurements and high-energy BCDI. The 34-ID-C end station has the capability to switch between monchromatic mode for BCDI and polychromatic "pink-beam" mode for Laue diffraction microscopy. Both HEDM and Laue diffraction microscopy can be used to orient crystals in a sample and give approximate locations of their position in the sample.

### 3.0.1 Far-Field High Energy diffraction Microscopy

Far-field high energy diffraction microscopy (ff-HEDM) is a bulk polycrystal characterization tool in use at synchrotrons such as the Cornell High Energy Synchrotron Source (CHESS) and the Advanced Photon Source (APS). [15, 58, 59]. At the APS, ff-HEDM is typically conducted at the 1-ID-E beamline. Samples up to 1 $\mu$m thick are placed into a $\geq$ 50 keV monochromatic beam and a section illuminated in a line scan. These samples are mounted on high-precision stages, and the beam can be focused down to a 1 *micron* beam height, allowing a specific portion of the sample to be illuminated. Because the x-rays are $\geq$ 50 keV, they are capable of penetrating through the entire thickness of the sample, allowing diffraction to occur on all grains throughout the sample's thickness. The sample is then rotated 360 degrees in $\omega$ (as shown in Fig. 3.1) with a step size $\delta\omega \geq 0.05$. ff-HEDM

typically uses large area detectors (2048 × 2048 pixels) with a 200 $\mu$m pixel pitch. These detectors are placed approximately 1 m from the sample. A diagram of the HEDM set-up at 1-ID-E can be seen in Fig. 3.1. As the sample is rotated, various planes from the grains in the illuminated portion of the sample enter the Bragg condition and diffract. The 360° scan range allows all possible reflections to be measured on a detector in the far-field. Depending on the lattice parameter of the material being measured, several Debye Scherrer rings may be captured on the far-field detector. At the end of the scan, diffraction data has been collected for a number of $\omega$ steps along in a 360° range. Reciprocal lattice vectors (RLVs) are computed for every diffraction spot collected and used to determine crystal orientations. In crystalline materials, peaks from the same crystal will be related to one another via symmetry, and comparison of RLVs allows them to be grouped and their orientations indexed. The center of mass for each grain is determined by accounting for the precession of diffraction spots as the sample is rotated.

If a grain is strained, its peaks will deviate from the expected scattering angle by a small amount. These distances for each diffraction spot can be fit to a strain tensor, giving the average strain in each grain. These tools are extremely helpful for BCDI, given that the grain size necessary for BCDI makes samples typically difficult to characterize using conventional tools such as electron back-scatter diffraction (EBSD). ff-HEDM at 1-ID-E allows us to bring a fairly unknown sample to the beamline, quickly determine the orientations and grain-averaged strains in every grain in the sample, and select the most interesting grain from a list to measure in BCDI.

After a grain is selected, the far-field detector is moved back, allowing the diffracted beams to propagate to the back wall of the beamline hutch, where a BCDI detector sits. This is necessary because of the compression of Fourier Space at high energies. The energy used for BCDI at 1-ID-E is 52 keV, a value which was optimized to ensure maximum coherence from the x-ray source [60,61]. In order to fully resolve a BCDI diffraction pattern at 52 keV, it is necessary to sample the pattern further downstream than the far-field HEDM detector, so the BCDI detector is placed $\sim$ 7 m from the sample. This BCDI detector is attached to an arm which extends radially from the incoming beam axis, allowing us to gather BCDI data from several Debye-Scherrer rings. Because ff-HEDM provides a list of

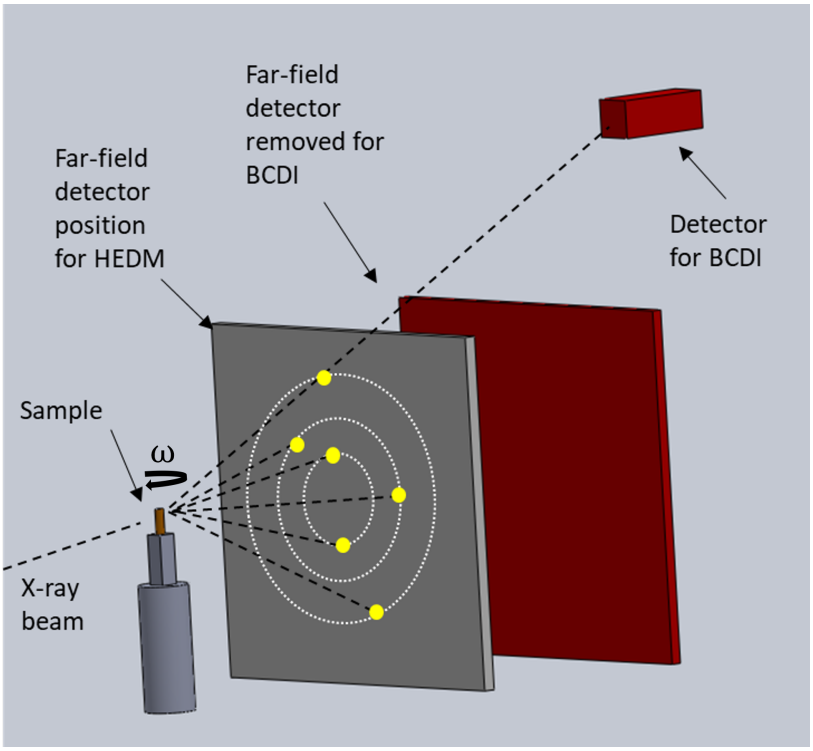


Figure 3.1: Diagram of the HEDM/BCDI configuration at 1-ID-E

grains and their orientations, it is trivial to search for and measure peaks from twin-related grains. This will be described in greater detail in the next section. The set-up at 1-ID-E also allows for a furnace to be inserted over the top of the sample. This furnace is typically used for HEDM experiments, but is also adaptable for HE-BCDI experiments, as will be described in Chapter IV.

### 3.0.2 Laue Diffraction Microscopy

The 34-ID-C beamline at the APS is the premier beamline in the world for BCDI. Its experimental geometry allows for a large portion of reciprocal space to be measured and its confocal microscope makes locating grains of interest straightforward. A diagram of the experimental geometry at 34-ID-C can be seen in Fig. 3.2

At the 34-ID-C beamline at the APS, ff-HEDM is not possible, given the configuration of the beamline and the relatively low energy of the x-rays. While it is possible to make an orientation map of a sample using the micro-Laue setup at the 34-ID-E, there are difficulties with ensuring that the reference frames are the same between the beamlines. Additionally,

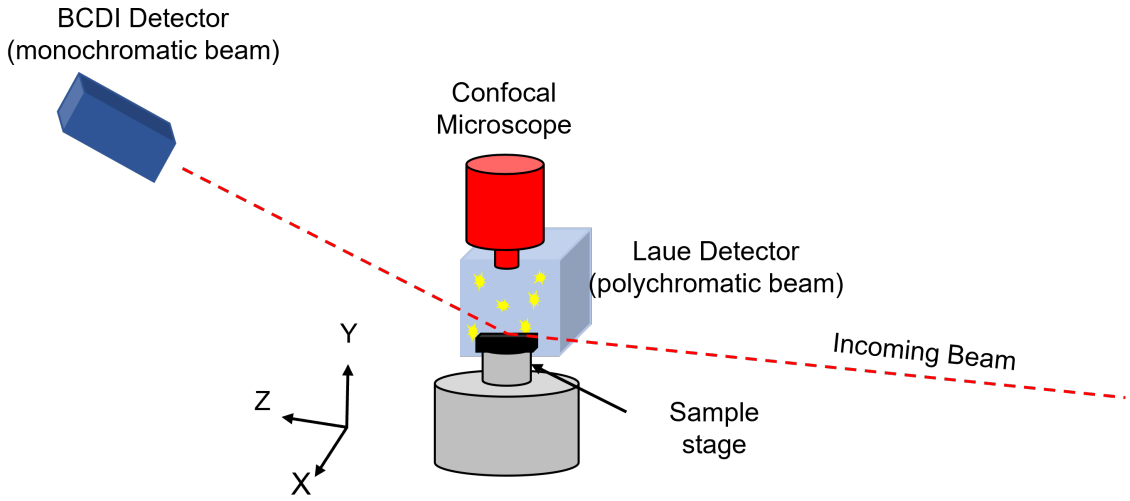


Figure 3.2: Diagram of the Laue/BCDI configuration at 34-ID-C. The monochromater can be switched between polychromatic mode and monochromatic mode to accommodate Laue Diffraction Microscopy and BCDI respectively.

taking a sample to the 34-ID-E beamline takes up valuable beam time and is not feasible for an experiment containing many samples.

To remedy this, a movable monochromater was installed in the hutch in 2020, allowing the beamline to operate in two modes: monochromatic and polychromatic. In monochromatic mode, x-rays are a single energy (usually 9 keV for BCDI), and coherent diffraction measurements can be conducted. In polychrmatic mode, the beam contains a spectrum of energies from 6 keV to 24 keV, enabling Laue Diffraction microscopy. While ff-HEDM fixes $\lambda$ by using a monochromatic beam and exploits Bragg's law by rotating the sample 360°, effectively changing $\theta$ in Eq. 2.4, Laue diffraction fixes $\theta$, and provides a continuous wavelength spectrum for $\lambda$. Because of this continuous energy range, when a crystal is illuminated, many reflections will be in the Bragg condition at the same time, producing a diffraction dataset like the one seen in Fig. 4.8. The locations of these peaks can be used to determine the orientation of the diffracting crystal and allow us to orient crystals at 34-ID-C in the same experimental configuration that will be used for BCDI.

Typically, orientations are found by "twiddling" the beam on and off a crystal of interest and visually checking the diffraction data to see which peaks appear and disappear with with the grain. These peaks are hand-selected and fed as input to a software package called LaueGo [62, 63], which is supported by the 34-ID-E beamline staff. LaueGo takes an input

list of energy ranges and a list of $\hat{\mathbf{q}}$ unit vectors for all peaks which are found on the detector, and returns a list of orientations by measuring the angular distances between all peaks and determining if any pairs match what would be expected for a certain crystal orientation. A list of all peaks indexed for a particular Laue pattern as well as the crystal orientation is returned. This technique was used to collect the dataset used in Chapter V.

While this method is suitable if a crystal has been pre-selected for measurement and is sufficiently isolated so that all the Bragg peaks on the Laue detector belong to it, it is not useful when there are many unknown crystals on a sample, or if there are many crystals in the beam at the same time. Thus, it was necessary to develop an automatic peak selection tool to accurately locate peaks and index them. Yueheng Zhang, a member of our research group, collaborated with me to make this tool. The first step was background subtraction and thresholding of the Laue dataset, to lower the likelihood that a noisy pixel was chosen as a Laue peak. Then the python package "scipy.ndimage" [64] was used to locate centro-symmetric objects in the dataset, returning a list of peaks and their positions on the detector. These peaks were then converted to $\hat{\mathbf{q}}$ unit vectors in reciprocal space, based on the detector position and orientation with respect to the sample.

When dealing with polycrytstals or small grains, it is also a surety that there will be many peaks on a single detector image due to the size of the incident x-ray beam. The Laue beam at 34-ID-C is $0.8\,\mu\text{m} \times 10\,\mu\text{m}$, meaning with a $\sim 1\,\mu$m grain size, tens of grains could be illuminated at the same time, resulting in hundreds of peaks from overlapping Laue patterns on the same detector frame. An example of such a dataset can be seen in Fig. 4.8, which is a Laue pattern from a Pt sample with sub-micron grain sizes.

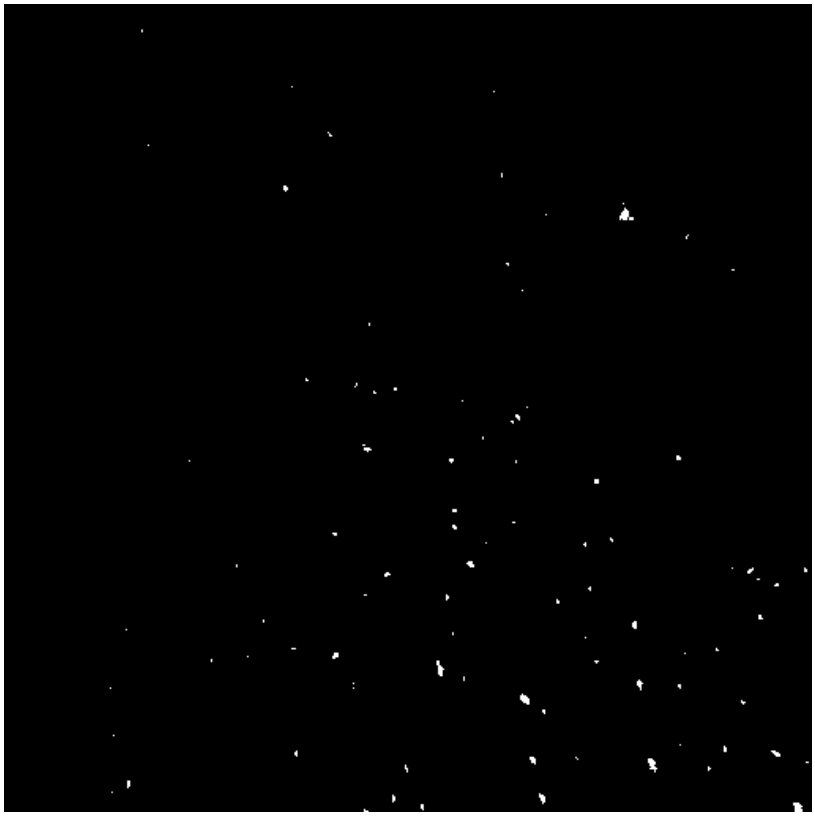

Figure 3.3: Pt Laue diffraction dataset. The many grains illuminated by the beam results in many overlapping Laue patterns, making it impossible to select peaks corresponding to the same Laue pattern by hand.

A brief study of the robustness of LaueGo was conducted to test this by adding randomly placed peaks to a known dataset. A Laue pattern of known orientation was chosen as the baseline for the study. These peaks were inputted to LaueGo along with a number of randomly placed peaks, and the results were logged. The number of noise peaks added was increased from 10 to 100, with steps of 10 peaks. For each of these steps, 100 sets of randomly placed peaks were generated and LaueGo called for each. The hit frequency, corresponding the number of times the known orientation was returned, was tracked over the course of this study. Additionally, the number of incorrect orientations, resulting from false positives as noise peaks were indexed, was tracked. Plots of these metrics can be seen in fig. 3.4.

It is clear that the number of peaks on the detector limits the likelihood that an orientation will be found. To remedy this, a colleague and I have built an automatic Laue indexing software, which repeatedly calls LaueGo for different frames of data. I wrote a

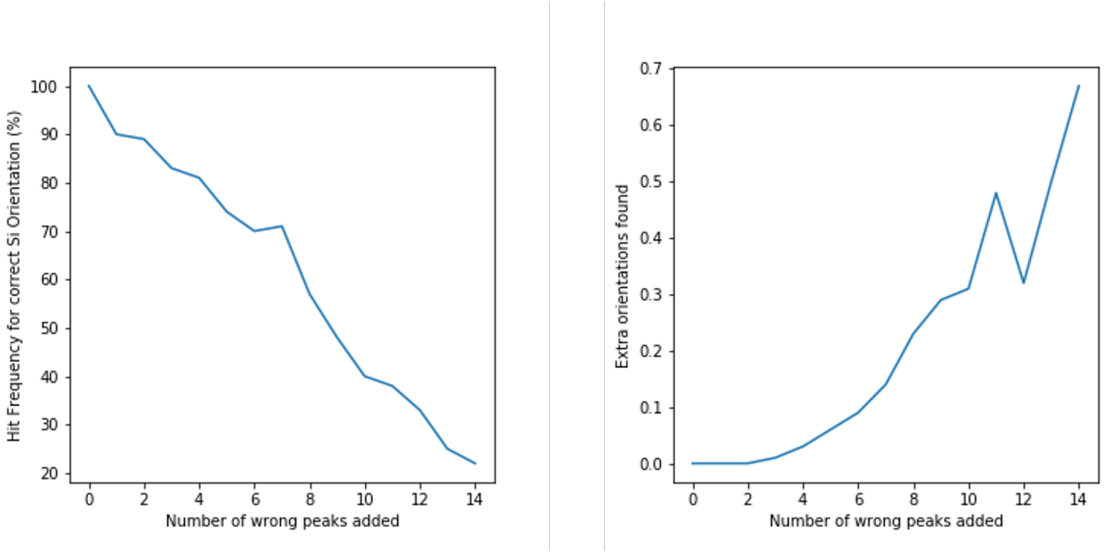


Figure 3.4: Plot of the average "hit rate" for LaueGo with increasing numbers of randomly placed "noise peaks" (Left). Plot of the average number of "false positives," where an orientation was returned from some of the peaks denoted as "noise".

package which locates all peaks on a detector image and divides them into random groups of a certain input size (usually $< 30$). These groups are then inputted to LaueGo for indexation, and orientations are saved based on a certain threshold in the confidence metric. This process is repeated for successive steps in the raster scan. With a step size of 100 nm and a beam width of 800 nm, it is expected that grains of the desired size ( 1 $\mu$m) should exist in 10-15 consecutive frames. This method has been used successfully to determine high confidence orientations at recent beamruns and will be explained in more depth in Chapter IV.

Unlike ff-HEDM, Laue scanning microscopy only returns orientation from grains on the surface of a sample. This is because the mean free path of 9 keV x-rays in metals is on the order of $\sim 1$ $\mu$m. After a list of orientations is returned, the misorientation must be calculated between each orientation in order to look for twin-related grains.

### 3.0.3 Finding Twin-related grains

Finding neighboring grains is difficult at the length-scales involved in BCDI. Neither of the above methods has the resolution to say with certainty that any two grains share a boundary. Unless known beforehand, finding neighboring grains is nearly impossible. Fortunately, annealing twins are readily found in FCC metals. Twin density is highest

for small grains in FCC metals [65–67] and have been measured several times with BCDI. Twins are, by definition, neighboring grains, and we can exploit the twin-misorientation relationship in FCC metals to locate pairs of these grains throughout the scanned volume of a sample.

For cubic materials, misorientations can be easily calculated using quaternion multiplication. A quaternion is an ordered set of four real numbers (q0, q1, q2, q3) making up a vector component and an angular component.

$$q = q_1 + \mathbf{i}q_2 + \mathbf{j}q_3 + \mathbf{k}q_4 \tag{3.1}$$

Their usefulness for misorientation calculation relies on the simplicity of quaternion multiplication.

$$pq = [p_1 q_1 - \mathbf{p} \cdot \mathbf{q}] + [p_1\mathbf{q} + q_1\mathbf{p} + \mathbf{p} \times \mathbf{q}] \tag{3.2}$$

Using quaternion multiplication, the following procedure is followed to find the misorientation $\alpha$ between quaternions $p_1$ and $p_2$.

1. Compute $q$ as the quaternion product of $p_1$ and the conjugate of $p_2$, $p_2^*$
2. Arrange $q$ so that $q_4 \geq q_3 \geq q_2 \geq q_1$
3. Choose the maximum value of the fourth component from these three variants
   (a) $(q_1, q_2, q_3, q_4)$
   (b) $(q_1 - q_2, q_1 + q_2, q_3 - q_4, q_3 + q_4)/\sqrt{2}$
   (c) $(q_1 - q_2 + q_3 - q_4, q_1 + q_2 - q_3 - q_4, -q_1 + q_2 + q_3 - q_4, q_1 + q_2 + q_3 + q_4)/2$
4. For unit quaternions, $q = \cos(\alpha/2) + \mathbf{r}\sin(\alpha/2)$, so $\alpha = 2\cos^{-1}(q_0)$

FCC twins share a $\Sigma 3$ grain boundary, constituting a 60° rotation about the (111) crystal plane, seen in Fig. 3.5. Once the misorientation is calculated between all grains, we can locate grains which are 60° misoriented from one another. From this much smaller list, the orientations can be compared to see if the misorientation is about a (111) plane.

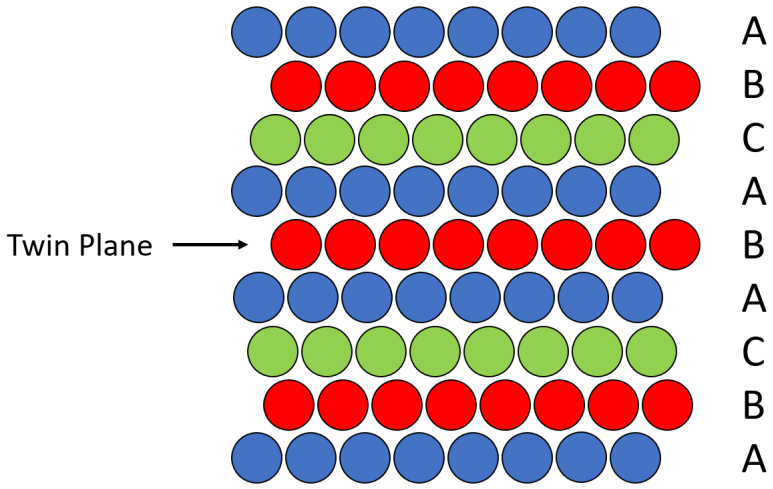


Figure 3.5: Σ3 twin boundary found in FCC metals. The twin and parent domains are misoriented by a 60 degree rotation about (111).

Once the orientations have been found, the BCDI measurements on each Bragg peak can be carried out easily, as the sample goniometer and detector can be driven to the correct motor positions to bring up the Bragg Peak. Because of the known misorientation of FCC twins, they present the most feasible multi-grain BCDI samples.

# CHAPTER IV

# Experiments

The goal of this work is to image strain fields around grain boundaries. Accomplishing this requires measuring BCDI datasets from at least three non-colinear reflections. Very few successful experiments with multiple reflections from the same grain have been conducted [23, 56, 68], so a learning curve was expected in sample design and experimental technique. To build up from single grain, single Bragg peak BCDI to multi-grain, multi-peak BCDI, the following experiments were proposed (in order of importance from least important to most important):

1. Measure multiple Bragg peaks from a single grain
2. Measure multiple Bragg peaks from neighboring grains
3. Measure multiple Bragg peaks from neighboring grains where a known event of interest has occurred
4. Measure multiple Bragg peaks from neighboring grains under load to map strain fields

To meet these experimental goals, the following samples were designed. When possible, samples were designed to meet the requirements of both the 1-ID and 34-ID-C beamlines at the APS.

## 4.1 Samples

### 4.1.1 De-wetted Au nanocrystals

The first two experiment designs have little utility from a materials science standpoint but are crucial for development of our algorithms and experimental techniques at the 34-ID-C

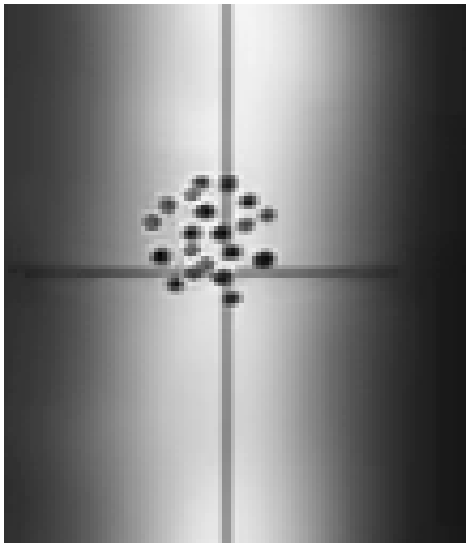

Figure 4.1: Confocal microscope image of section of Au patterned gold sample. The black spots are Au nanocrystals.

and 1-ID beamlines. The vast majority of phase retrieval work (and all of the existing literature on multi-peak phase retrieval) [24, 25] is validated on simulated data, which typically fails to capture the complexities involved in a real experiment. Collecting high-quality datasets to use for the CPR algorithm, as well as the forthcoming multi-grain reconstruction algorithm, was vital. De-wetted Au nanocrystals have been shown to give excellent diffraction patterns [38, 69] for BCDI, given their relatively low lattice strain. A patterned Au nano-crystal sample was prepared by sputtering Au onto Si and $Al_2O_3$ substrates and annealing until the Au de-wetted and coarsened into nano-crystals [70]. During the deposition process, Au atoms stack in the (111) crystal direction, given that the (111) plane is the closest-packed plane. This lends itself to Au twin formation as irregularities in the deposition process can lead to stacking faults, which form twin boundaries on annealing. Because of this, these samples are also ideal for collecting quality BCDI data from twinned grains. A microscope image of the patterned-Au on $Al_2O_3$ sample can be seen in Fig. 4.1

Recently, an AFM tip has been installed at the 34-ID-C beamline. With this in place, there is now the potential to find a twinned grain with Laue microscopy, locate it in the beamline microscope and load it, making these samples feasible for experiment goal 4. This will be discussed in Chapter VII.

### 4.1.2 Platinum Trench Samples

A significant challenge for experiment 4 is to load a grain without destroying it and be able to measure multiple peaks from it during loading. In an AFM tip experiment like the one described above, only one Bragg peak could be measured during one loading attempt. Because the AFM tip is not connected to the rotation stage at the 34-ID-C beamline, the grain is effectively pinned when it is being loaded by the AFM tip. This means that only one peak can be measured during loading, via a scan in energy, rather than a scan in $\theta$. Because of this, it would be beneficial to have a sample which could be loaded in a controlled manner, but without the use of a loading stage. We have designed a sample which consists of a line of Pt deposited into a channel which has a width and depth on the order of the coherence length of the beamline (800 nm $\times$ 800 nm). A schematic of this sample can be seen in 4.2. The trench serves two purposes. First, it provides a single line of Pt crystals, allowing for certainty as to the spatial location of crystals in the sample. Additionally, the coefficient of thermal expansion in Si is significantly smaller than that of Pt ($2.6 \times 10^{-6\,\circ}\mathrm{C}^{-1}$ to $8.8 \times 10^{-6\,\circ}\mathrm{C}^{-1}$) [71, 72]. Thus, upon heating, the Pt should expand more than the Si, inducing a compressive stress on the Pt grains. This allows us to strain only the Pt crystals in the sample without destroying them so that BCDI diffraction patterns can be captured from multiple peaks. To test this theory, a simulated trench sample was made, containing 20 cube grains with side lengths of 800 nm. The heating of the sample was simulated using an analysis code (MASSIF) [73], which uses the FFT method to calculate local micro-mechanical response to applied loads, ensuring that constitutive relations are satisfied at every voxel. The heating experiment was simulated by applying a uniform eigenstrain in each Pt grain (based on the coefficient of thermal expansion differential between the two materials) and allowing the stresses to equilibrate. The eigenstrain applied was calculated according to:

$$\varepsilon = (\alpha_{Si} - \alpha_{Pt}) \times \Delta T \tag{4.1}$$

where $\alpha_{Si}$ is the coefficient of thermal expansion for Si, $\alpha_{Pt}$ is the coefficient of thermal expansion, and $\Delta T$ is the temperature difference between the furnace temperature and room

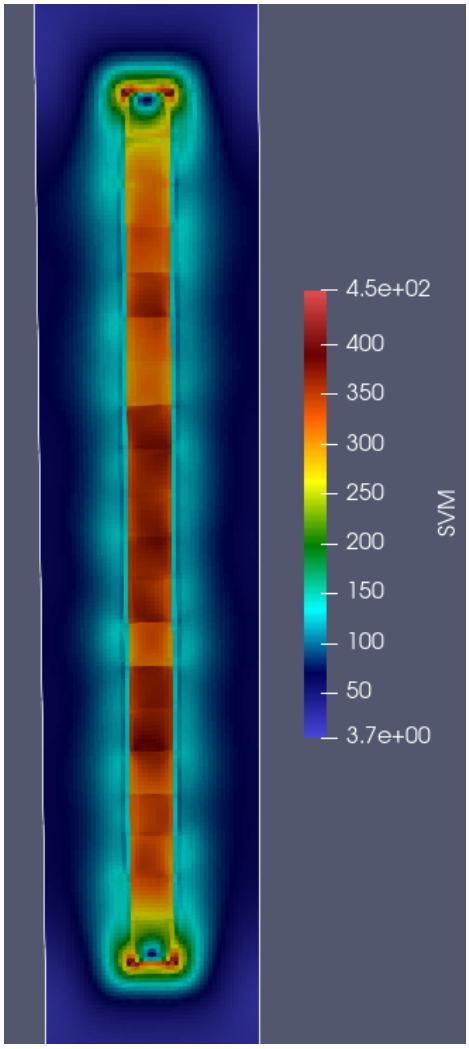


Figure 4.2: MASSIF simulation of the compressive stress imposed on the Pt trench by the Si substrate, as a result of the CTE difference between the two materials.

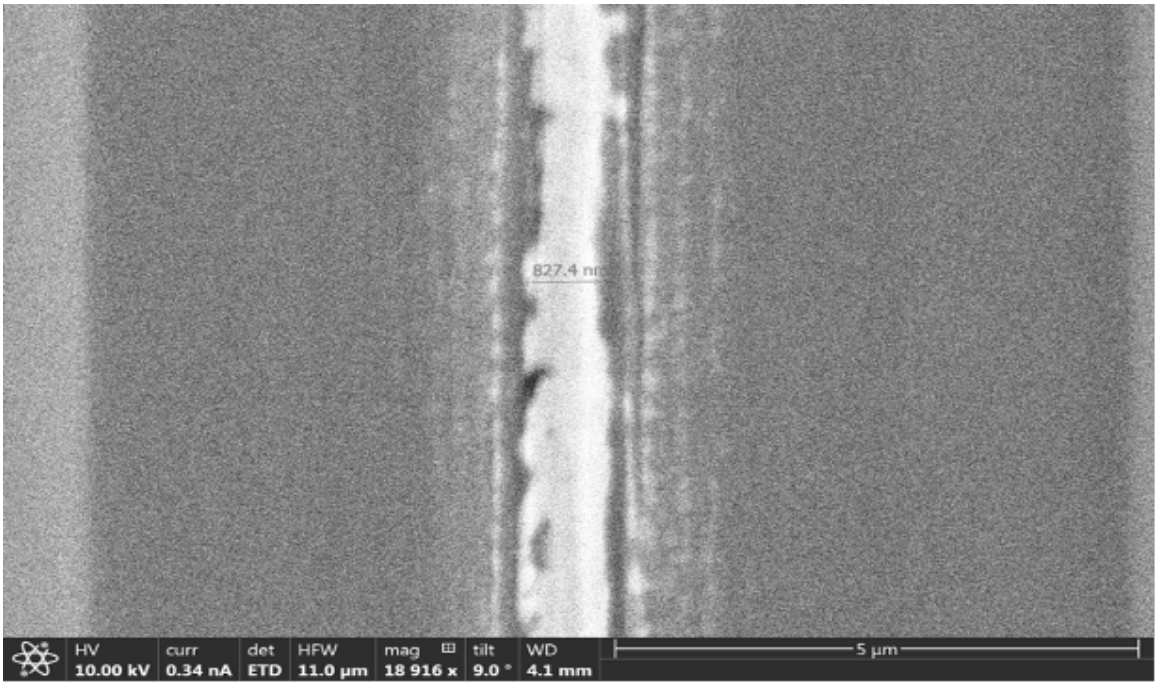


Figure 4.3: SEM image of Pt-trench sample. The goal is to create a line of grains which are within the coherence length of the beamlines at 34-ID and 1-ID.

temperature. This simulation shows that it is conceivable to generate a sizeable compressive stress on the sample ( 300 MPa) by heating only to 400 deg C.

The samples were created using a FEI Plasma Dual Beam FIB SEM with a $Xe^+$ plasma focused ion beam (PFIB) on a $< 100 >$ Si wafer. Three trenches were FIBed into the Si, with width and depths of $800 \times 1000$ nm, $600 \times 800$ nm, and $400 \times 600$ nm and length of 100 $\mu$m. Pt was FIB-deposited into the trenches, and the trenches were FIB-polished down so that the cross sections were $800 \times 800$ nm, $600 \times 600$ nm, and $400 \times 400$ nm respectively. This was to ensure a relatively flat surface at the top of the trench. The samples were annealed for 12 hours at 600 C, potentially providing many grains within the coherence length of both the 1-ID and 34-ID beamlines. A micrograph of a trench can be seen in 4.3. The hope of this sample was to create a sample which has a "bamboo" structure, with a line of grains side-by-side in a trench.

It can be seen that the Pt is confined to the trench with slight variations due to the limits of FIB polishing at this scale. Because the substrate is single-crystal Si, there will one set of peaks on the detector other than those from the Pt grains in the sample. If a polycrystalline substrate was used, Laue diffraction microscopy would be extremely difficult

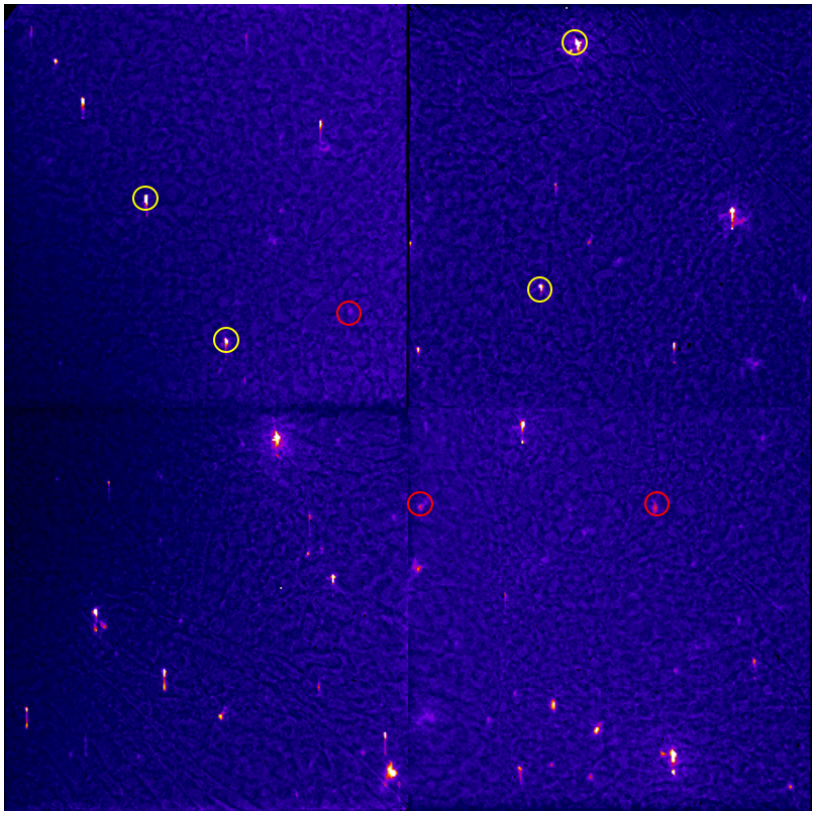

Figure 4.4: Example Diffraction Pattern with Pt and Si peaks. Example Pt peaks are circled in red and example Si peaks in yellow. It can be seen that the Pt peaks are significantly dimmer than the Si peaks. This makes it simpler to remove the Si peaks from the peak list for the automatic Laue indexing routine.

because it would be impossible to tell which peaks belonged to Pt and which peaks belonged to the substrate. As is, it is quite easy to differentiate the Si peaks from the Pt peaks, because the Si substrate, being a large single-crystal, is a strong scatterer, resulting in Laue peaks many orders of magnitude brighter than the Pt. An example can be seen in 4.4. At 34-ID, using a trench sample limits the number of Pt peaks on the detector at a given time, making indexation of Laue patterns more straightforward.

## 4.2 Experiments completed

### 4.2.1 Goal 1: Measure multiple Bragg peaks from a single grain

The first experimental goal serves as an important step in the process of combining Laue Diffraction and BCDI at the 34-ID-C beamline. A partner user proposal between our colleagues, CMU, and the 34-ID-C beamline staff worked to integrate these two techniques

at the beamline for the first time. In December 2019, an experiment was conducted on a patterned Au sample described above. Because the automatic laue indexing routine had not yet been developed, the confocal microscope was used to locate an isolated Au nanoparticle in the beam, and the beam was "twiddled" on and off of this location so that the peaks corresponding to the Laue pattern from this crystal could be found. These peaks were selected by hand and inputted to LaueGo, providing the orientation of the crystal. From this orientation, it was determined that four reflections were reachable by the detector, given the current beamline configuration. These reflections were $(\overline{1}\overline{1}1), (1\overline{1}1), (11\overline{1})$ and (200). The data was collected with angular steps from $-0.5^\circ$ to $0.5^\circ$ with a step size of $0.01^\circ$. This scan was repeated four times on each peak, with the Bragg peak being re-centered on the detector after each scan. All scans were then aligned and added together to be used for phase retrieval. The central slice of the diffraction patterns for each reflection can be seen in 4.5. This data was used to validate the CPR method. Results and analysis of this result can be found in chapter V.

### 4.2.2 Goal 2: Measure multiple Bragg peaks from neighboring grains to look at internal stress and strain fields

The second experimental goal exists for two purposes: proving that multi-grain experiments are possible at 34-ID-C by validating the Laue orientation mapping tool that has been developed, and providing a dataset for development of the multi-grain reconstruction code, which will likely be necessary for high-fidelity reconstructions in future multi-grain BCDI experiments. In September 2021, the first multi-grain experiment was successfully conducted at 34-ID-C. The Laue microscopy tool described in III was used to locate a twinned Au nanocrystal on the patterned Au sample. The two grains were located at the same position on the sample and had orientations of $[01\overline{1}][1\overline{1}\overline{1}]$ and $[10\overline{1}][1\overline{1}1]$, which constitute an exact FCC twin relationship by a $60^\circ$ rotation about a [111] axis. Six Bragg peaks were measured from each crystal. They can be seen in Figs. 4.6 and 4.7. The data was collected with angular steps from $-0.5^\circ$ to $0.5^\circ$ with a step size of $0.01^\circ$. This scan was repeated four times on each peak, with the Bragg peak being re-centered on the detector after each scan. All scans were then aligned and added together to be used for phase retrieval.

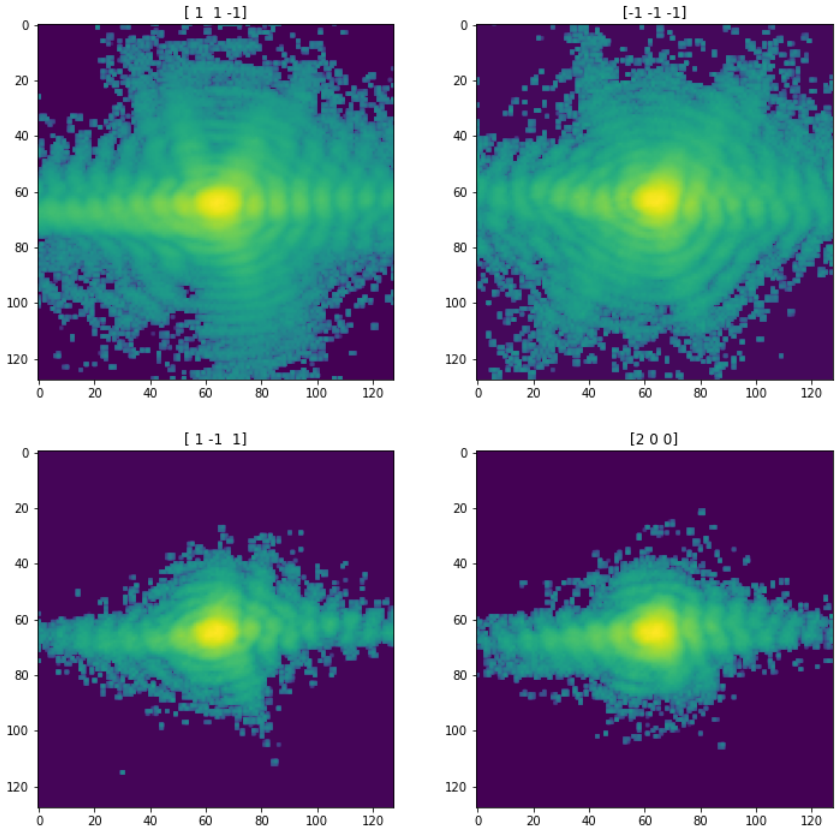


Figure 4.5: Central slice of diffraction patterns from 4 Au reflections. Intensity plotted on log scale, with peak max set to $10^7$ for all peaks.

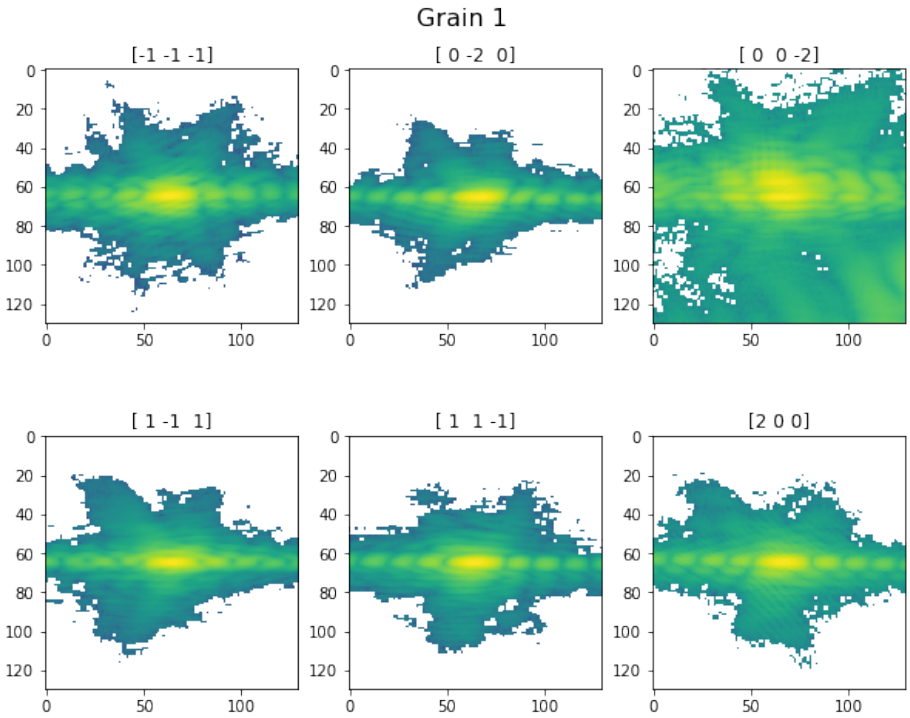


Figure 4.6: Central Frame of six Bragg peaks from Grain 1 of the twin dataset. Intensity plotted on log scale, with peak max set to $10^7$ for all peaks.

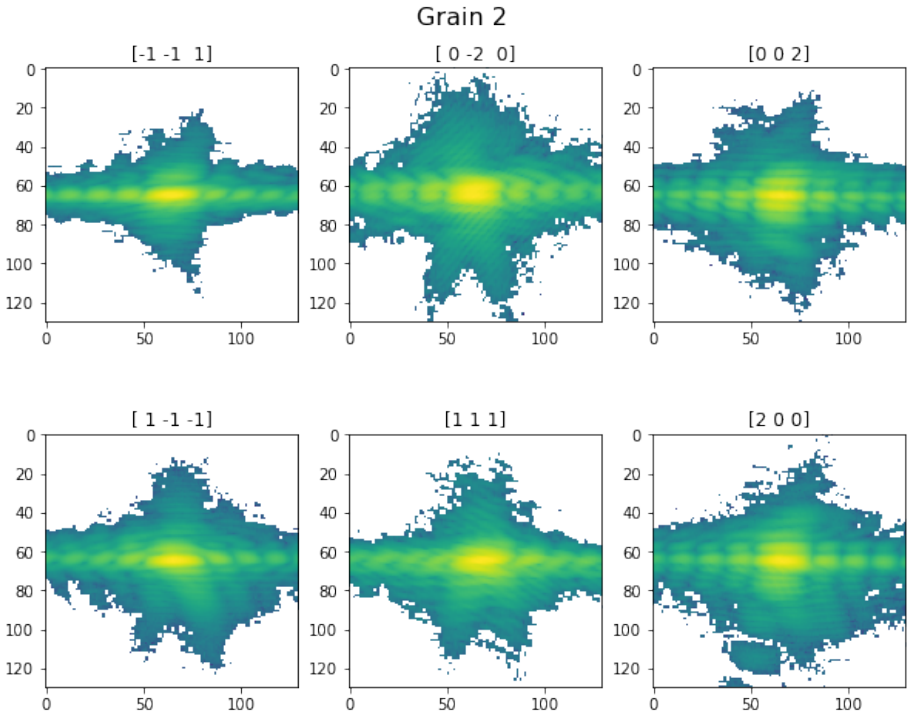


Figure 4.7: Central Frame of six Bragg peaks from Grain 2 of the twin dataset. Intensity plotted on log scale, with peak max set to $10^7$ for all peaks.

Analysis of this sample is underway, but preliminary results will be used to help validate the multi-grain reconstruction routine outlined in Chapter VI. To our knowledge, this is the first ever BCDI experiment where multiple peaks were measured from neighboring grains.

### 4.2.3 Measure multiple Bragg peaks from a single grain under load

In July 2021, a HE-BCDI experiment on a Pt-trench sample was conducted at 1-ID. X-ray tomography was used to locate the Pt trench in the sample and to align the beam. Then a ff-HEDM scan was collected to determine the orientations of all crystals in the sample, that one might be picked to study. A grain was selected and six Bragg peaks were collected from the sample using BCDI at room temperature. After this, the sample was heated to $160°C$ and the six Bragg peaks were collected again. The sample was then cooled back to room temperature so that the effect of heating on the internal structure could be observed. Figure 4.8 shows six Bragg peaks collected at room temperature. Analysis of this experiment is still underway and will be discussed in more detail in Chapter VII.

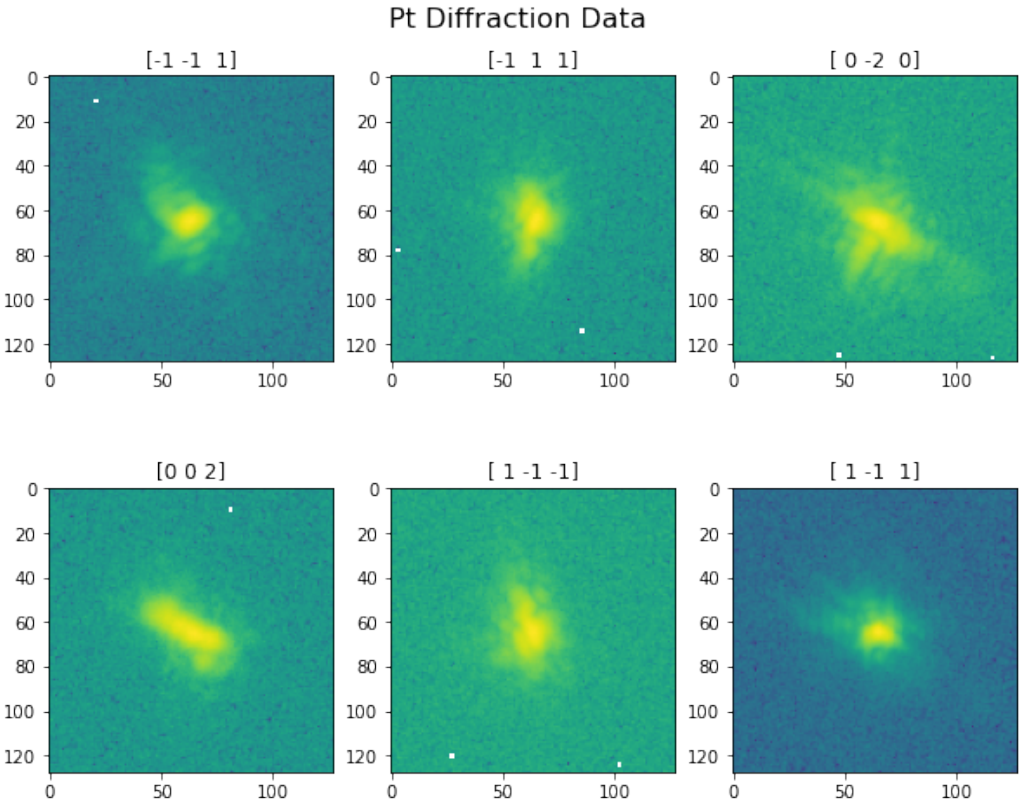


Figure 4.8: Central Frame of six Bragg peaks for the Pt trench sample collected at 1-ID. Diffraction patterns were collected at room temperature

### 4.2.4 Sources of Experimental Error

There are several sources of error typical to BCDI datasets. The first is partial coherence of the beam. Particularly at high energies, the x-ray beam cannot be assumed to be perfectly coherent. Additionally, measuring a particle larger than the coherence length (Eq. 2.9), scattering cannot be considered coherent. Because the coherence length at 1-ID is $\sim 235$ nm, many particles measured at this beamline are slightly larger than the coherence length. This reduced coherence leads to a blurring of the diffraction pattern and reduced fringe visibility, as can be seen if one compares the fringes in Fig. 4.5 and Fig. 4.8. The fully coherent intensity can be estimated by optimizing a 3-D Gaussian partial-coherence function to be convolved with the forward-modeled intensity $\hat{\psi}_i(\mathbf{q})$ during phase retrieval [74,75], but it cannot be guaranteed that the true coherent intensity will be found. Additionally, stray scattering on the detector adds noise to the data, and is usually handled by thresholding. Kinematic diffraction is typically assumed in BCDI, but especially for larger grains or multi-peak datasets dynamical diffraction may begin to influence the data and a refraction correction would be required for each Bragg peak. Other sources of experimental error include imperfections in the beam and particle drift from the crystal shifting slightly during measurement. All of these are common issues in BCDI and can be dealt with to some extent.

# CHAPTER V

# Multi Peak BCDI

As discussed in Chapter II, several multi-peak reconstruction algorithms have been developed and demonstrated on simulated data, but as yet, none have been deployed on experimental data, which has historically proven more difficult to reconstruct, due to imperfections in the datasets. This chapter details our own multi-peak reconstruction routine, along with the genetic algorithm in which it is used. We demonstrate its efficacy on simulated and experimental data and show improvement over independent phase retrieval in terms of reconstruction accuracy and consistency for reconstructing both both types of data. The work in sections 5.1 and 5.2 has been published in [76].

Additionally a brief study is made of reconstructing dislocations in multi-peak BCDI. Studying dislocations is a major goal of BCDI work [23, 77] and it will be important for any multi-peak phase retrieval routine to be able to handle the difficulties involved with dislocations in BCDI datasets. We demonstrate the ability of our routine to consistently reconstruct datasets with dislocations and the improved accuracy gained by using a genetic algorithm over conventional multi-peak BCDI.

## 5.1 Multi-Peak Reconstruction Methods

### 5.1.1 Coupled Phase Retrieval with ER/HIO

The coupled phase retrieval (CPR) approach we developed and deployed on simulated and experimental data is described in this chapter[1]. The strategy is composed of two major

[1]Text in sections 5.1 and 5.2 taken from Wilkin et al. [76]. 

components: an adaptation of the BCDI ER/HIO phase retrieval strategy in which a mechanism of coupling information from multiple Bragg peaks is introduced; and utilization of multiple instances of this modified ER/HIO strategy within the framework of a genetic algorithm, which is known to provide robustness against stagnation in the context of experimental data. A flow chart of the CPR algorithm utilized here is pictured in Fig. 5.1a. A CPR reconstruction consists of $J$ parallel constituent reconstructions (hereafter called "constituents") of $J$ Bragg peaks which have been interpolated onto a uniform grid and rotated into a common laboratory frame using the approach defined by Maddali et al. [21]. A sequence of fixed point iteration steps consisting of ER and HIO (hereafter called a "recipe") is used for each constituent. Every twenty iterations, the phase and amplitude values from each constituent $j$, ($\phi_j(\mathbf{x})$ and $\rho_j(\mathbf{x})$ from Eq. 2.11), are combined to calculate universal values $\overline{\rho}(\mathbf{x})$ and $\mathbf{u}(\mathbf{x})$, which are defined below. These values are then then used to seed the new phase and amplitude values ($\phi_j{}'(\mathbf{x})$ and $\rho_j{}'(\mathbf{x})$) for the next twenty iterations of each constituent.

During the combination step, the universal amplitude $\overline{\rho}(\mathbf{x})$ is calculated by averaging the $\rho_j(\mathbf{x})$ fields returned from each peak according to

$$\overline{\rho}(\mathbf{x}) = \frac{\sum_{j=1}^{J} \hat{\rho}_j(\mathbf{x})}{J}. \tag{5.1}$$

where $\hat{\rho}_j(\mathbf{x})$ is the real space amplitude for constituent $j$, normalized by its sum over all voxels. At specified iterations, shrinkwrap (Eq. 6.15) is applied to this universal amplitude $\overline{\rho}(\mathbf{x})$ (rather than to each constituent amplitude $\rho^j(\mathbf{x})$), and the universal support $\mathbf{S}$ is updated. This new support function is then used as the new real-space constraint for each constituent at all successive ER and HIO steps until shrinkwrap is applied again. This support refinement process effectively selects the morphology of one of the two phase retrieval twins [78] and enforces it on all constituents to the end.

Additionally, the universal displacement field $\mathbf{u}(\mathbf{x})$ is updated during the combination step, using the least-squares optimization proposed by Hoffman [23]. In this approach, $\mathbf{u}(\mathbf{x})$

is optimized on a voxel-by-voxel basis to minimize the loss function

$$L_n = \sum_{j=1}^{J} (\mathbf{u}_n \cdot \mathbf{G}_{j,hkl} - \phi_{j,hkl,n})^2, \tag{5.2}$$

where the subscript $n$ denotes a voxel in the reconstructed array. If the phases are consistent for a given image voxel across all constituents, $L$ is zero. More commonly, there will be inconsistencies in the constituent phases, and the loss function $L$ provides a way to find the most consistent displacement field in that pixel.

Our algorithm utilizes this strategy to reconcile inconsistencies in the constituent reconstructions in terms of $\mathbf{u}(\mathbf{x})$ every twenty iterations throughout the reconstruction process.

### 5.1.2 Genetic Algorithm

Single Bragg peak experimental BCDI data sets have been found to benefit from a guided phase-retrieval algorithm [7,79,80] approach, which improves the robustness of the solution. Aiming to leverage the benefits of such algorithms, we have adopted a similar strategy for the CPR approach presented here, based on the work of Ulvestad et al. [7]. Genetic algorithms (GA) are a family of methods which use the theory of natural selection to optimize a solution. A population of possible solutions ("individuals"), each possessing a set of attributes ("chromosome"), are evolved over a series of generations to produce the best possible solution. At each generation, the "fittest" individual is bred with all others, updating their chromosomes and creating a new generation of individuals. This process proceeds until the fittest individual sees negligible improvement from generation to generation. The work by Ulvestad etal. describes a genetic algorithm in which each individual is a reconstruction of the same Bragg peak, with $\psi(\mathbf{x})$ being the chromosome. The initial population of individuals in the first generation are seeded with a random-phase starting guess and a cube support, and phase retrieval is applied to each. The individual with the lowest $\chi^2$, Eq. 2.21, after phasing is selected as the 'fittest' and bred with all other individuals according to

$$\psi_m^{i+1} = \sqrt{\psi_f^i(\mathbf{x}) * \psi_m^i(\mathbf{x})}, \tag{5.3}$$

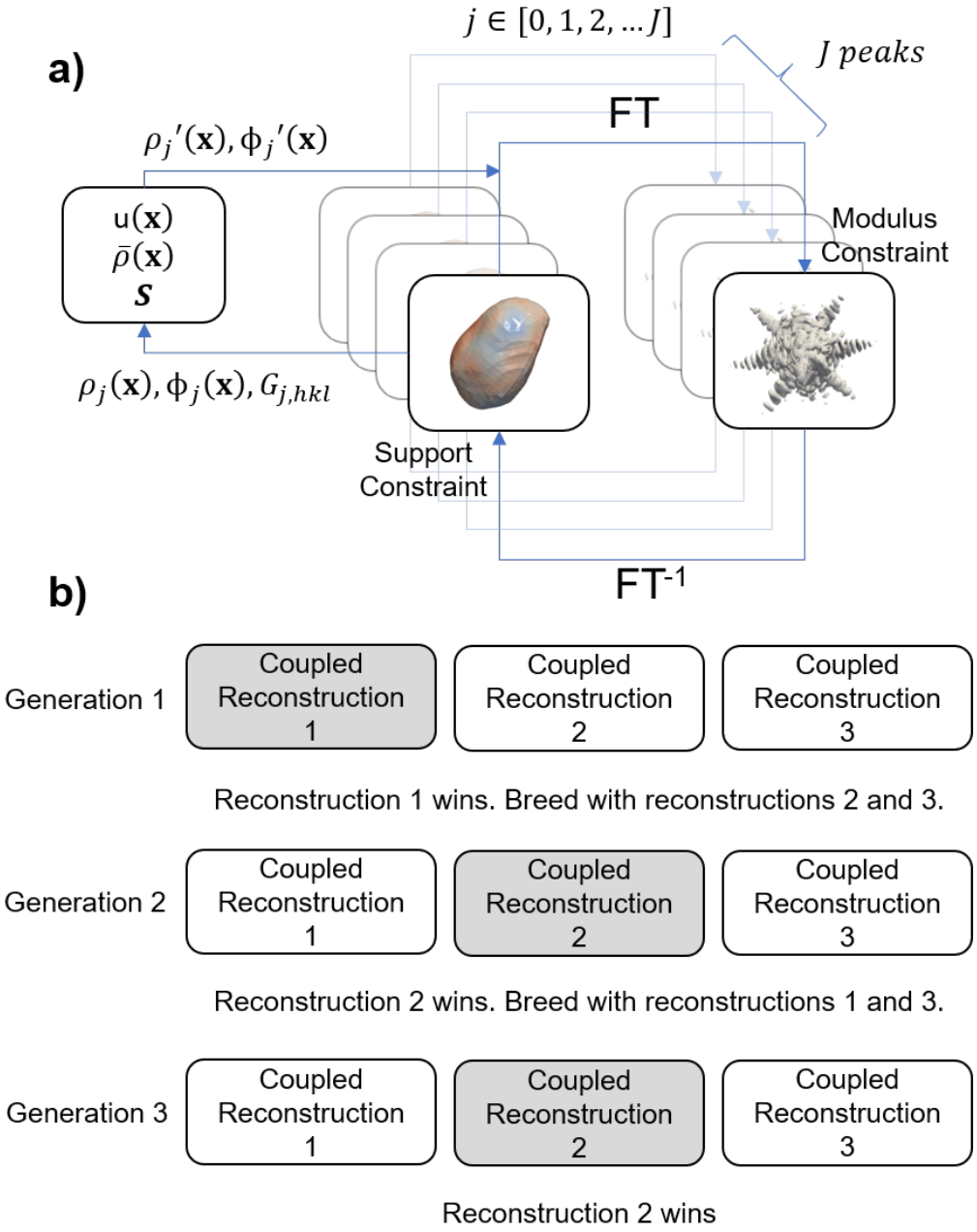


Figure 5.1: Schematic of the CPR routine (a) and CPR-GA (b). Each peak is put through a phase retrieval recipe including iterations of ER and HIO. At designated iterations during the recipe, the universal values $\mathbf{u}(\mathbf{x})$ and $\overline{\rho}(\mathbf{x})$ are computed from the most recent phases and amplitudes from each constituent. The new $\mathbf{u}(\mathbf{x})$ is projected along each $G_{j,hkl}$ vector to update the phase guess for each constituent $\phi_j{}'(\mathbf{x})$, and the new $\overline{\rho}(\mathbf{x})$ is used to update the amplitude guess $\rho_j{}'(\mathbf{x})$. At specified iterations, shrinkwrap is applied to the universal amplitude to update the universal support $\mathbf{S}$, which is used for all constituents. The CPR-GA depicted consists of three generations of three individuals. Individuals are instances of the CPR routine in (a). Individuals are bred with the fittest individual after each generation by averaging their $\mathbf{u}(\mathbf{x})$ and $\overline{\rho}(\mathbf{x})$ values.

where the subscript $f$ denotes the fittest individual, the subscript $m$ denotes one of the other individual reconstructions within generation $i$. Then, $\psi_m^{i+1}$ is used as the initial guess for individual $m$ and another round of phase retrieval is applied. This process is repeated for a specified number of generations, after which, the fittest individual is chosen as the final reconstruction. The state-of-the-art for independent phase retrieval (IPR) of multiple Bragg peaks consists of reconstructing each peak using this GA and finding the common $u(\mathbf{x})$ and $\bar{\rho}(\mathbf{x})$ from the final reconstructions using Eq.5.1 and Eq. 6.7 respectively. We will call this approach "IPR-GA."

In this work, we modify the above GA routine so that each individual is a CPR reconstruction and breeding is performed on the quantities $\bar{\rho}(\mathbf{x})$ and $\mathbf{u}(\mathbf{x})$. We will call this approach "CPR-GA." A flow chart showing the CPR-GA is shown in Fig. 5.1b for three individuals bred for three generations. For the first generation in this example, each of the three individuals is seeded with a random phase start and a cube object support on all its constituents. The CPR routine is executed on each individual, yielding three amplitudes $\bar{\rho}(\mathbf{x})$ and displacement fields $\mathbf{u}(\mathbf{x})$. The individual with the lowest $\chi^2 = \sum_j \chi_j^2$ (summed across all constituents) is selected as the fittest, and its amplitude and displacement are bred with all other individuals to seed the next generation of CPR reconstructions. Thus, the amplitudes and displacement fields of the $(i+1)$ generation of individual $m$ are defined by the breeding functions:

$$\bar{\rho}_m^{i+1}(\mathbf{x}) = \sqrt{\bar{\rho}_m^i(\mathbf{x}) * \bar{\rho}_f^i(\mathbf{x})} \tag{5.4}$$

and

$$\mathbf{u}_m^{i+1}(\mathbf{x}) = \frac{\mathbf{u}_m^i(\mathbf{x}) + \mathbf{u}_f^i(\mathbf{x})}{2}. \tag{5.5}$$

This pattern repeats for a specified number of generations until $\chi^2$ converges.

### 5.1.3 Confidence Metrics

When reconstructing multiple peaks, it is important that the constituents show good agreement with their measured diffraction patterns (low $\chi^2$) and with each other (low $L$). We

define a scalar $L$ for a multi-peak reconstruction as

$$L = \frac{\sum_{n=1}^{N} \bar{\rho}_n L_n}{\sum_{n=1}^{N} S_n}, \tag{5.6}$$

summing over all $N$ voxels in the 3D array describing the sample reconstruction space. In this expression, per-voxel $L_n$ values were weighted by the amplitude $\bar{\rho}_n$ (dampening the contribution of low-fidelity voxels to the total value), and normalized by the support volume $\sum_{n=1}^{N} S_n$. We also utilize the scalar value $\chi^2$ (defined in Eq. 2.21) to assess the reconstructions. $L$ and $\chi^2$ effectively act as fidelity metrics in real and reciprocal space respectively, and both will be considered when analyzing results.

### 5.1.4 Sampling Geometry and Interpolation

In BCDI, the diffraction pattern is sampled in three directions: detector x axis, detector y axis, and the scanning direction $\theta$. Each of these directions correspond to a vector in Fourier space, which we will call $q_1$, $q_2$, and $q_3$ respectively. The length of each vector is the sampling step size in that direction. In the x,y plane of the detector, the sampling step size is determined by the pixel pitch. Thus, $||q_1||$ and $||q_2||$ are typically equal. $||q_3||$, on the other hand, is derived from the step size in $\theta$ during the scan. Because the curvature of the Ewald's sphere is low at $9keV$ and the angular steps are small (typically $\sim 0.01°$), successive detector images are assumed to be parallel to one another and orthogonal to $q_3$. Together, $q_1$, $q_2$, and $q_3$ make up a set of sampling basis vectors which we will call $\mathbf{B}$. Typically, diffraction patterns are sampled on a non-orthogonal grid because the detector is not perfectly orthogonal to the diffracted beam $\mathbf{k}_f$. It is also common for $||q_3||$ to be larger than $||q_1||$ and $||q_2||$ as the detector usually oversamples the diffraction pattern at a higher rate than is necessary. Determination of these sampling bases is different for each BCDI beamline and out of the scope of this work. Methods for determining these bases are detailed in work by Maddali *et. al.* [21].

The fact that the data is sampled on a non-uniform, non-orthogonal grid means that any reconstruction of said data will be reconstructed on the same such frame, albeit in real space, rather than Fourier space. Thus, for visualization of a reconstruction, it is necessary

to represent the data on this sheared grid, rather than a regular, orthogonal one. Because different Bragg peaks are collected at different sample stage and detector positions, combining multiple reconstructions also requires an interpolation and rotation of each reconstruction from a unique sheared grid in the detector frame to a common orthogonal grid crystal frame. While this is perfectly feasible in the IPR method, the computational cost of interpolation becomes unwieldy in the CPR algorithm [25]. Interpolation post-reconstruction would require an interpolation step for every constituent during every combination step in the CPR algorithm, Additionally, the combined reconstruction would have to be interpolated back onto the sheared detector frame grid for the next round of phase retrieval for each constituent. This results in two interpolations per constituent for each combination step in the CPR routine, meaning hundreds of interpolations during the course of an entire routine. To remedy this, we perform the interpolation and rotation step on the raw dataset. By doing the interpolation in Fourier space, it only has to be done once, driving down the computational cost considerably. It is possible that interpolating the dataset itself results in artifacts in the final reconstruction, but it stands to reason that interpolating the data once is better than interpolating the reconstruction twice per iteration for thousands of CPR iterations. This will be discussed further in Chapter VII.

The rotation and interpolation step begins by selecting a voxel size for the new crystal-frame grid. If the sampling basis for peak $j$ is $\mathrm{B}_j$, the volume of a unit cell in the raw dataset in the detector frame is $\det(\mathbf{B}_j)$. The new grid must be uniform, so we choose a voxel size $l$ which is equal to

$$l = \sum_{j}^{J} \frac{\det(\mathrm{B}_j)^{(-1/3)}}{J}. \tag{5.7}$$

This should ensure that the diffraction pattern sampling rate is not increased or decreased during the interpolation step. Following the determination of the grid, the total reciprocal space range in each sampling direction for dataset $j$ is determined according to

$$\mathbf{r}_j = \mathrm{B}_j \mathbf{p}_j \tag{5.8}$$

where $\mathbf{p}_j$ is a $3 \times 1$ array containing the number of pixels in each dimension of the raw

dataset. A new orthogonal grid is constructed which spans $[0, r_m)$ (for $m \in x, y, z$) in each dimension with a step size of $l$. To save computational cost, it is simpler to interpolate from a uniform grid to a non-uniform grid. Because the known data points in the crystal-frame exist on a non-uniform grid and the unknown points on a uniform grid, the interpolation is best done in the detector frame, where the known points are on a uniform grid and the unknown points on a non-uniform grid. Each unknown crystal-frame grid point $\mathbf{x}_n$ is transformed back to the detector-frame according to

$$\mathbf{x}'_n = \mathrm{B}^{-1}\mathbf{x}_n \tag{5.9}$$

The raw data is then interpolated onto the new points $\mathbf{x}'_n$ (for $n \in [1, N]$) in the detector-frame. This step results in $J$ datasets in a common uniform grid, ready to be used for CPR.

## 5.2 Validation of CPR algorithm

The CPR-GA was validated using both simulated and experimental data sets. For the simulated data set, a 3D shape function of a nominally 400 nm gold nano-particle was extracted from a grain growth simulation performed with the SPPARKS Monte Carlo Potts Model [81] and decorated with a $\mathbf{u}(\mathbf{x})$ field. The phase fields of four Bragg reflections, $(1,1,1), (1,1,\bar{1}), (1,\bar{1},1)$ and $(\bar{1},1,1)$, were calculated and their Bragg peaks generated by taking the DFT of the object and squaring it's modulus (Eq. 2.13). The grain was zero-padded so that the diffraction patterns would be oversampled by a factor of 2. The peak intensity was scaled to a max photon count of $10^7$, and Poisson noise was then added on a pixel-by-pixel basis.

This data set was reconstructed using the IPR-GA and the new CPR-GA. For the IPR-GA, five generations of eight individuals were used, with the population being culled to the four best individuals after two generations. For each generation, all individuals were reconstructed using the following phase retrieval recipe [2] , which consisted of:

[2] A customized phase retrieval software [82] was used for all reconstructions.

1. 100 iterations of ER, update support after iterations 60 and 100
2. 60 iterations of HIO
3. 80 iterations of ER, update support every 40 iterations
4. 60 iterations of HIO
5. 100 iterations of ER, update support every 20 iterations
6. End of generation. Breed with fittest individual.

At the end of each generation, the displacement was calculated using the least-squares approach in Eq.6.7 with the fittest individuals from each peak.

For the CPR-GA, the recipe above was used for all constituents to evolve a single generation for each individual. For each CPR reconstruction in the CPR-GA, the universal values $\mathbf{u}(\mathbf{x})$ and $\overline{\rho}(\mathbf{x})$ were updated every 20 iterations during the recipe, and, at specified iterations, the support update operation was applied to the global support $\mathbf{S}$. Five generations of eight individuals were used for the CPR-GA, with the population being culled to the four best individuals after two generations. The number of generations was determined to ensure convergence in $\chi^2$, such that the $\chi^2$ decreases by a negligible amount from generation to generation [83].

An experimental data set was collected at the 34-ID-C beamline at the Advanced Photon Source (APS). Using Laue diffraction, four reflections, $(\bar{1},\bar{1},\bar{1}), (1,1,\bar{1}), (1,\bar{1},1)$, and $(2,0,0)$, were found for a Au nano-crystal de-wetted onto a Si(100) substrate [68]. BCDI measurements were taken for each reflection. The diffraction patterns corresponding to each reflection were interpolated onto a regular grid and rotated into the same reference frame [21]. The same reconstruction approach was used as for the simulated data. Six generations of eight individuals were used for both the CPR-GA and the IPR-GA, with the populations being culled to the four best individuals after two generations. The number of generations was chosen as the point at which the percent improvement in fitness between the best individual from the current generation and the best individual in the previous generation drops below 1%

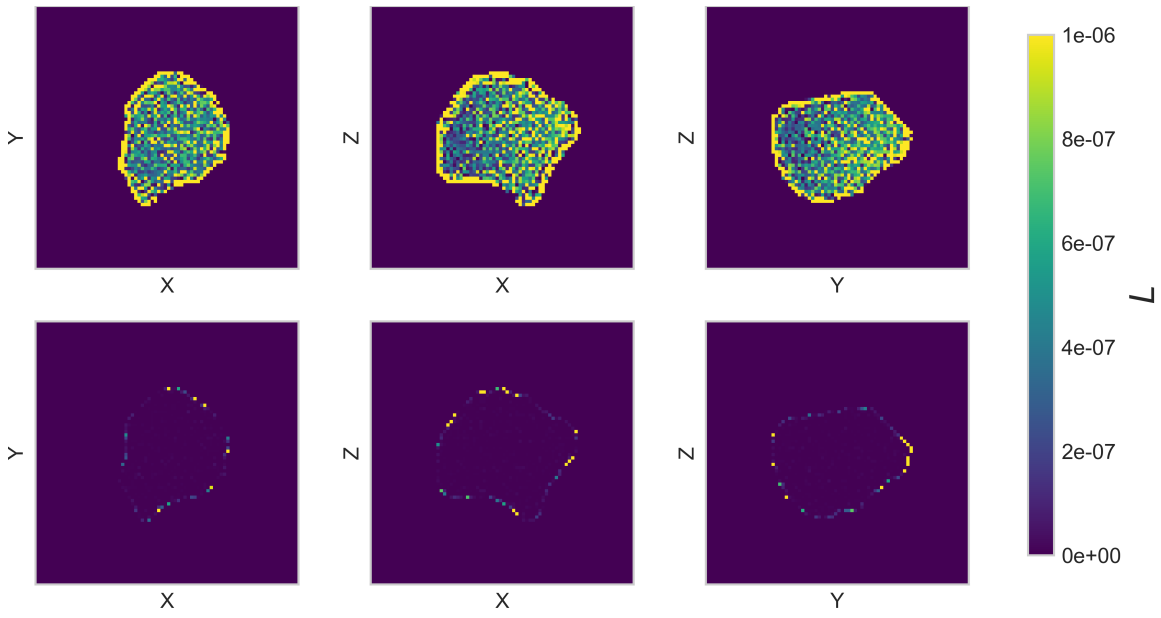


Figure 5.2: $L(\mathbf{x})$ map for IPR-GA (top) and CPR-GA (bottom) for the simulated data set. The best reconstructions were chosen for each method. Cross sections in the x-y, x-z and y-z planes are shown. The CPR-GA reconstruction shows lower $L$ values at nearly every voxel, suggesting good agreement between its constituents. $L$ values have been capped at $10^{-6}$ in order to visualize the values in the coupled reconstruction.

### 5.2.1 Validation of CPR on Simulated Data

In order to assess and compare the overall efficacy of the CPR-GA approach versus the IPR-GA approach over repeated instantiations, the simulated data sets were reconstructed 40 times using the IPR-GA and 40 times using the CPR-GA, each with different random starting guesses. In each of the 40 reconstruction runs, five generations of the GA were performed. A plot of confidence metrics averaged over all 40 runs is shown at each generation (Fig. 5.5). The plotted metrics for each method are the average $L$ and $\chi^2$ values at each generation normalized by the sum over all generations, $L_{tot}$ and $\chi^2_{tot}$ respectively.

By the end of five generations, the CPR-GA performed better in both $\frac{\chi^2}{\chi^2_{tot}}$ and $\frac{L}{L_{tot}}$ showing an improvement of $3.87 \times 10^{-2}$ in $\frac{\chi^2}{\chi^2_{tot}}$ and $6.66 \times 10^{-2}$ in $\frac{L}{L_{tot}}$ or 39.2% and 96.7% respectively. An $L$ map of the best reconstruction from each method can be seen in Fig. 5.2. The CPR-GA reconstruction shows lower $L$ at nearly every voxel.

Comparison of strain fields in the ground truth crystal and reconstructed crystal can be seen in Fig. 5.3. It is clear that the CPR-GA method was able to accurately recover the strain shape and magnitude with great accuracy.

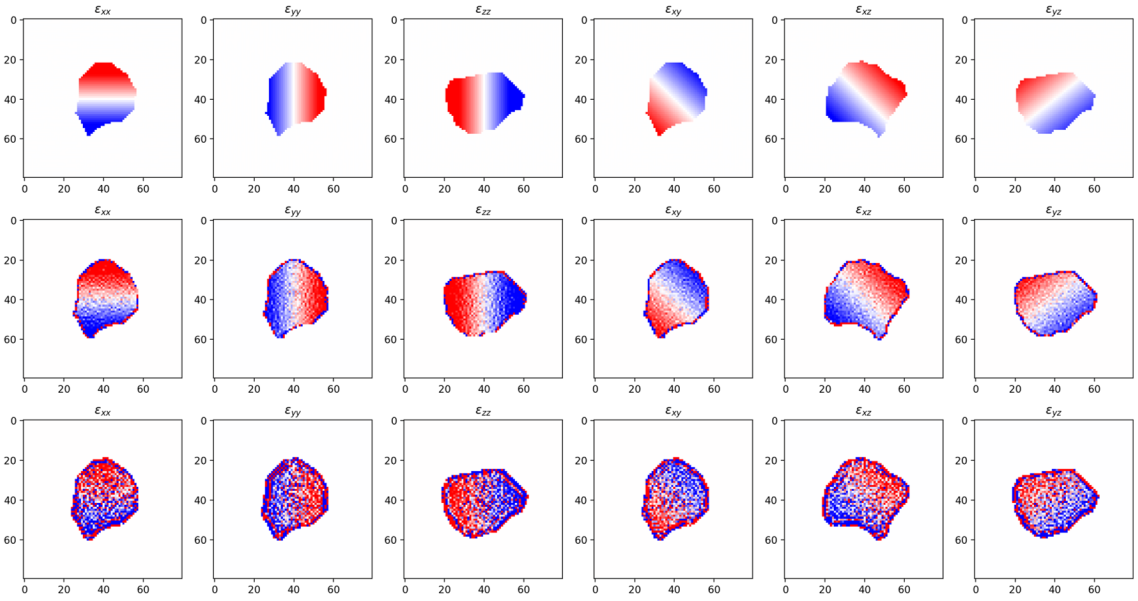


Figure 5.3: Comparison of strain fields in the ground truth crystal (top) and the best reconstructions using CPR-GA (middle) and CPR (bottom). Cross sections were chosen based on the direction of greatest strain gradient in the simulated crystal. It can be seen that CPR-GA produces more accurate strain fields than vanilla CPR.

### 5.2.2 Validation of CPR on Experimental Data

The experimental data sets were also reconstructed 40 times using both algorithms. An example CPR-GA reconstruction can be seen in Fig. 5.6. This result is physically plausible, as it is expected that the Au nano-crystal would be faceted and have a flat surface where it touches the Si substrate. The strain fields were calculated by differentiating the displacement field with respect to the sample-frame directions x, y, and z, given as

$$\varepsilon = \begin{bmatrix} \frac{du_x}{dx} & \frac{1}{2}\left(\frac{du_y}{dx} + \frac{du_x}{dy}\right) & \frac{1}{2}\left(\frac{du_z}{dx} + \frac{du_x}{dz}\right) \\ \frac{1}{2}\left(\frac{du_y}{dx} + \frac{du_x}{dy}\right) & \frac{du_y}{dy} & \frac{1}{2}\left(\frac{du_z}{dy} + \frac{du_y}{dz}\right) \\ \frac{1}{2}\left(\frac{du_z}{dx} + \frac{du_x}{dz}\right) & \frac{1}{2}\left(\frac{du_z}{dy} + \frac{du_y}{dz}\right) & \frac{du_z}{dz} \end{bmatrix}. \tag{5.10}$$

As seen in Fig. 5.4, the CPR-GA reconstruction shows lower $L$ values than the IPR-GA reconstruction throughout the crystal volume. A comparison of the error for each reconstruction method can be seen in Fig. 5.5. For the experimental data, the CPR-GA again performed better than the independent routine in both metrics, showing improvement of $4.1 \times 10^{-3}$ in $\frac{\chi^2}{\chi^2_{tot}}$ and $5.09 \times 10^{-2}$ in $\frac{L}{L_{tot}}$, improvements of 5.07%, and 53.23% respectively.

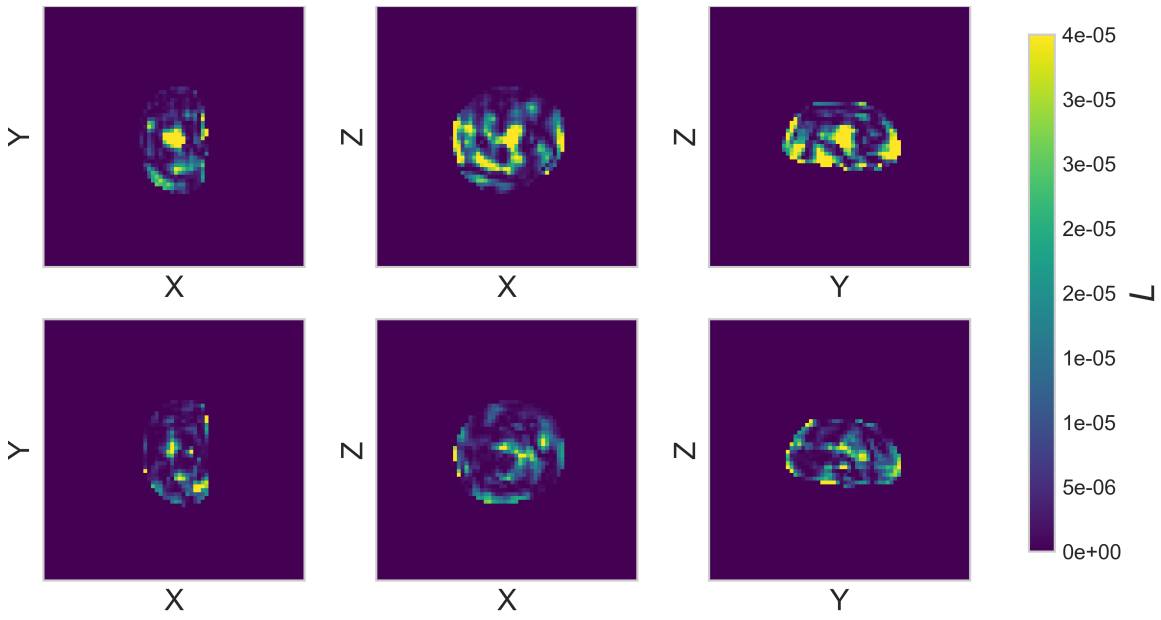


Figure 5.4: $L(\mathbf{x})$ map for IPR-GA (top) and CPR-GA (bottom) for the experimental data set. The best reconstructions were chosen for each method. Cross sections in the x-y, x-z and y-z planes are shown. The CPR-GA reconstruction shows lower $L$ values than the IPR-GA, suggesting good agreement between its constituents. $L$ values have been capped at $4 \times 10^{-5}$ in order to compare smaller values in the interior of the crystal.

While the $\frac{\chi^2}{\chi^2_{tot}}$ value converges for the IPR-GA, the $\frac{L}{L_{tot}}$ value actually increases gradually, suggesting that the constituents drift further apart with each generation. Conversely, the $\frac{L}{L_{tot}}$ for the CPR-GA stays constant as $\frac{\chi^2}{\chi^2_{tot}}$ converges. This demonstrates that, by combining reconstructions every 20 iterations, the CPR-GA effectively reduces $\frac{L}{L_{tot}}$ by sharing information from all Bragg peak measurements during phase retrieval, while the IPR-GA does not. Though less pronounced than for the simulated data, the improvements in both $\frac{L}{L_{tot}}$ and $\frac{\chi^2}{\chi^2_{tot}}$ for the experimental data demonstrate that the CPR-GA provides a more self-consistent estimate of $\mathbf{u}(\mathbf{x})$ than the IPR-GA.

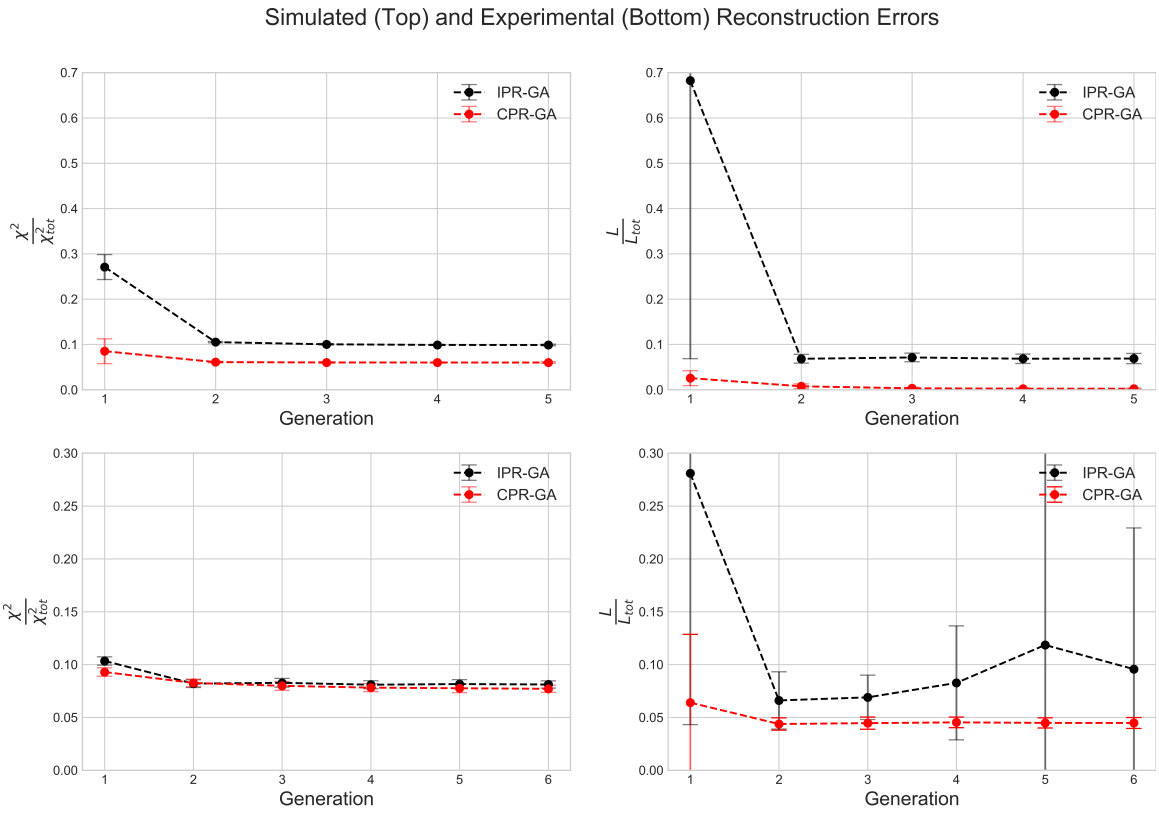


Figure 5.5: Comparison of the average $\frac{\chi^2}{\chi^2_{tot}}$ and $\frac{L}{L_{tot}}$ over 40 reconstructions of the simulated (top) and experimental (bottom) data sets using the independent and coupled routines. It is clear that the coupled routine performs favourably compared to the independent routine for both data sets. Spurious errors for the $\frac{L}{L_{tot}}$ values for the independent reconstruction reflect the fact that $\frac{L}{L_{tot}}$ is unconstrained in this method.

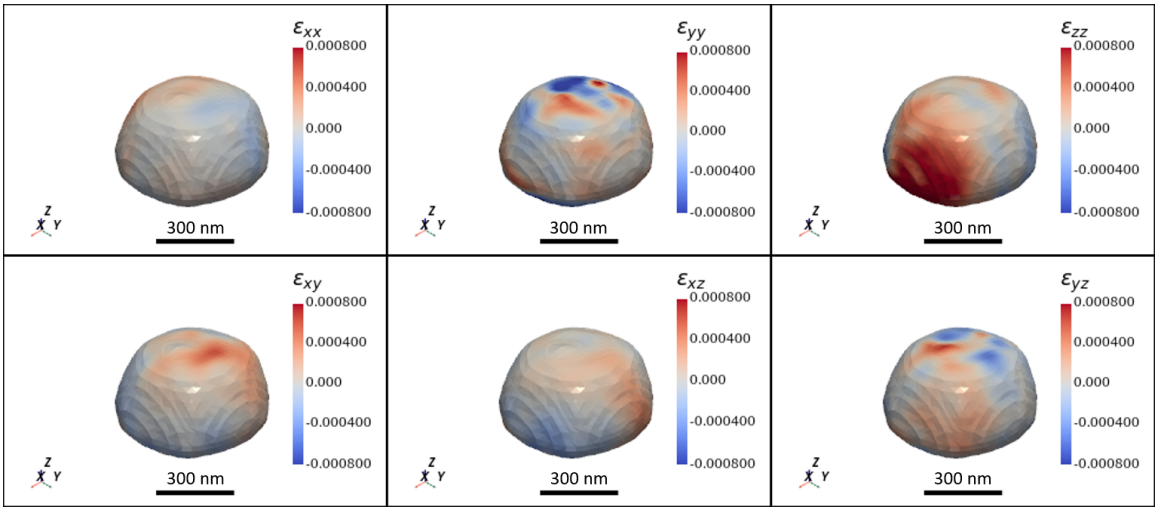


Figure 5.6: CPR-GA reconstruction of experimental Au nano-crystal on Si substrate. The strong facets and existence of a flat surface on the x-z plane agree with expectations.

## 5.3 Reconstructing Dislocations

Because the ultimate motivation behind our use of BCDI is the study of plasticity in polycrystals, we must address the reconstruction of dislocations and the difficulties introduced by their presence. As described in Chapter II, the Burger's vector of a dislocation represents the magnitude and direction of the lattice distortion caused by the dislocation. Because bonds have been broken at the core of the dislocation, there exists a local discontinuity in the lattice displacement field there. Given that BCDI voxels are tens of nanometers in length, the strain fields from the dislocation are only observed far from the core. Nevertheless, this discontinuity creates mathematical difficulties during phase retrieval. The displacement field around a screw dislocation can be seen in Fig. 5.7 and an edge dislocation in Fig. 5.8.

It can be seen that in both dislocation types, there is a discontinuity extending radially from the dislocation core to the edge of the crystal. This discontinuity is an artifact of Burger's vector construction. Because atoms about a dislocation are arranged in a helix, instead of parallel planes, the displacement field contains a discontinuity where the 360° helix segment ends. The displacement at this point is exactly $b$, which is the lattice distortion caused by the screw dislocation as the lattice displacement increases by $b$ with each rotation about the dislocation core. Locally, this displacement field is not actually discontinuous, given that each atom is only slightly displaced from its neighbors, but when viewed from the context of a single lattice plane, a discontinuity exists. The elastic strain is equal to $\frac{1}{2}[\nabla\mathbf{u}(\mathbf{x}) + [\nabla\mathbf{u}(\mathbf{x})]^T]$ . The gradient of a discontinuous displacement has no physical

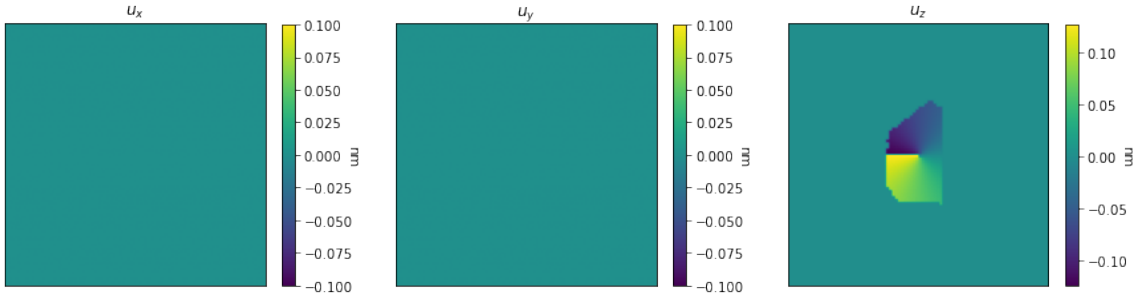


Figure 5.7: Cross section of the displacement field of a screw dislocation along the [110] axis. Because screw dislocations only displace atoms parallel to the Burger's vector, only one component of the displacement is nonzero.

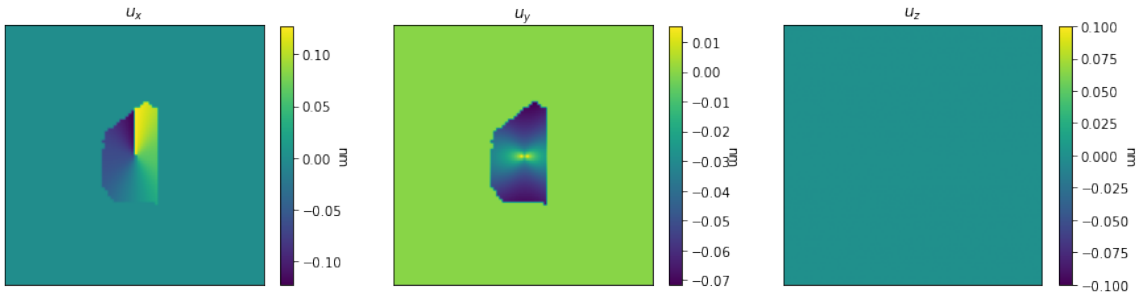


Figure 5.8: Cross section of the displacement field of a edge dislocation along the [110] axis. Edge dislocations have a component of displacement perpendicular to the burger's vector.

meaning, so it must be removed.

Hofmann et al. demonstrated a method for handling discontinuities in elastic strain on a reflection by reflection basis [23]. Their multi-peak reconstruction technique involved computing the gradient of the phase along each axis and combining this information to construct the elastic strain tensor. Because phase is the projection of the displacement along the scattering vector, the contribution of the Burger's vector to the phase can be given as $\mathbf{b} \cdot \mathbf{G}_{hkl}$. Any displacement of more than one lattice spacing $d$ will result in a phase wrap, where the phase range exceeds $2\pi$. Thus, the phases corresponding to reflections sensitive to the dislocation Burger's vector can have a range of $-\pi$ to $\pi$, resulting in a discontinuity. To correct for the discontinuity in phase gradient, two degenerate phase fields are constructed by adding and subtracting $\frac{\pi}{2}$ to $\phi$. This rotates the discontinuity clockwise and counterclockwise from its original position. The gradient of these fields is taken with respect to all axes and the final gradient array is assembled by taking the gradient of the smallest magnitude from the three options for each voxel.

A similar technique will be used here to deal directly with the displacement field returned from CPR. It is necessary to do this for the displacement instead of the phase because CPR constantly transforms between phase space and displacement space, and strain is only determined as a post processing step. Because it is impossible to correct the displacement field discontinuity itself, we must apply it at the end.

To correct the strain fields obtained from $\mathbf{u}(\mathbf{x})$, a constant $u_0$ is added to the displacement field. The values above the original maximum are shifted by $-range(\mathbf{u}(\mathbf{x}))$, rotating the displacement discontinuity. The same procedure is then applied using $-u_0$ as the con-

stant. We now have three degenerate displacement fields, which we will call $\mathbf{u}^0$, $\mathbf{u}^+$ and $\mathbf{u}^-$. The gradient of each of these fields will be taken and the voxel with the lowest strain magnitude in from each will be used to construct the lattice strain field. This procedure can be seen in Fig. 5.9. Example strain fields about a screw dislocation with the discontinuity and after the discontinuity has been reomved can be seen in Figs. 5.10) and 5.11.

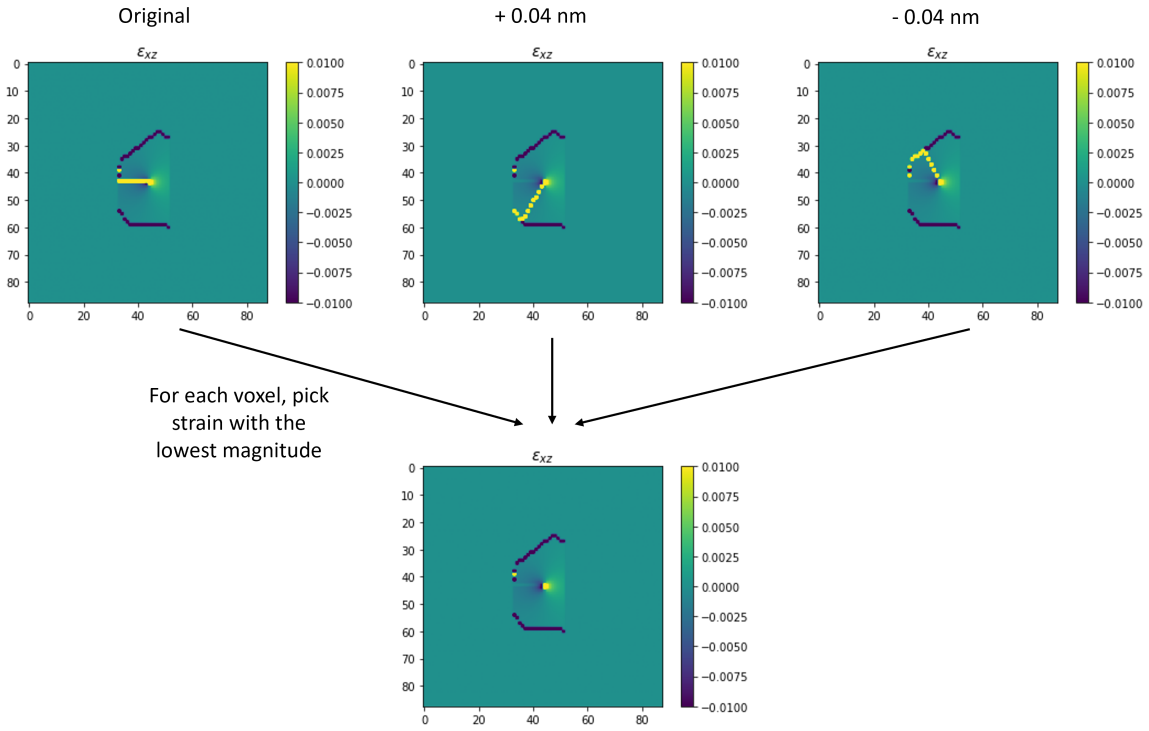


Figure 5.9: schematic of strain discontinuity removal based on the technique developed by Felix Hofmann.

It can be seen that this technique adequately removes the strain discontinuity and produces the correct strain fields about a screw dislocation. The difficulty with applying this technique is that the phases for each constituent reflection must be aligned such that the discontinuity is in the same position.

Because BCDI datasets are sensitive to a projection of the lattice displacement, certain Bragg reflections will not be sensitive to the dislocation at all. Take, for example, a $\frac{1}{2}[110]$ screw dislocation, with $b = \frac{a}{\sqrt{2}}$. The dislocation will not appear in the [002] reflection, nor in the $[1\bar{1}1]$ reflection because $\mathbf{b} \cdot \mathbf{G}_{hkl} = 0$. The reflections in which it does exist, however, contain projections of the burger's vector along the scattering vector. This means that the resulting phase field will contain a discontinuity where the displacement field does. For FCC

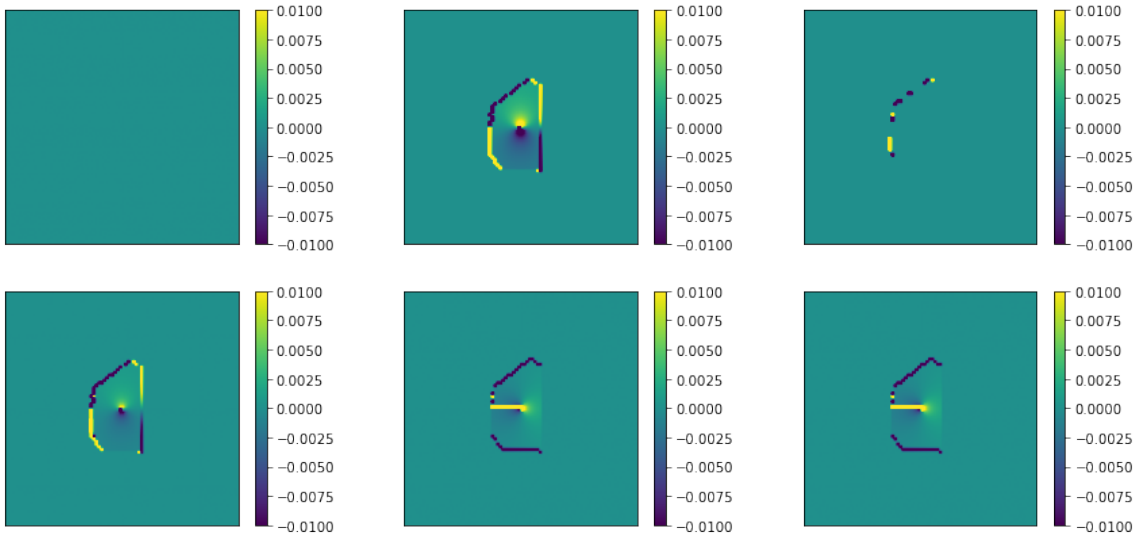


Figure 5.10: Six components of elastic strain tensor for displacement field around screw dislocation with discontinuity.

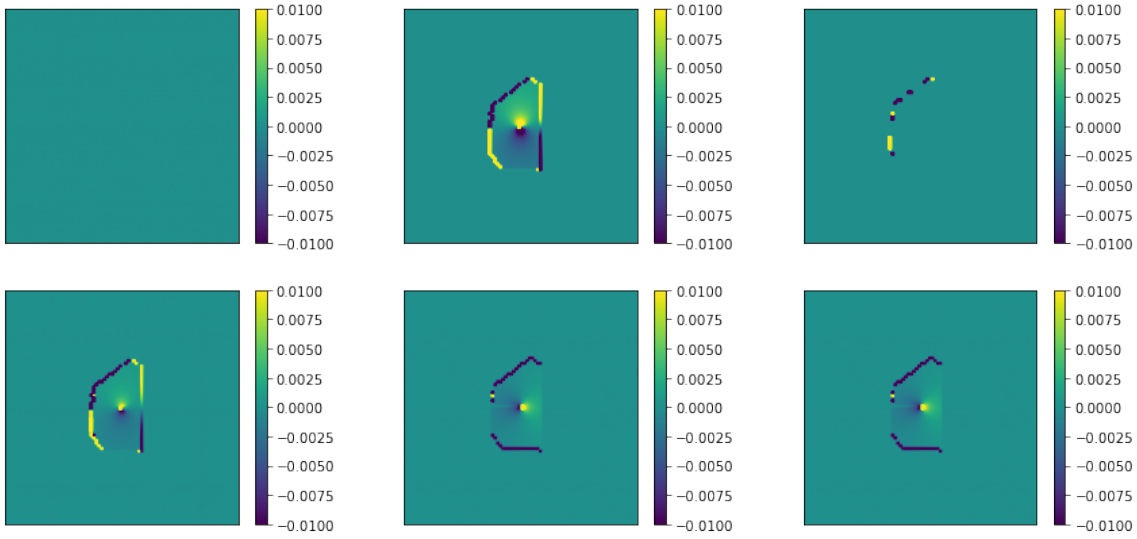


Figure 5.11: Six components of elastic strain tensor for displacement field around screw dislocation with discontinuity removed.

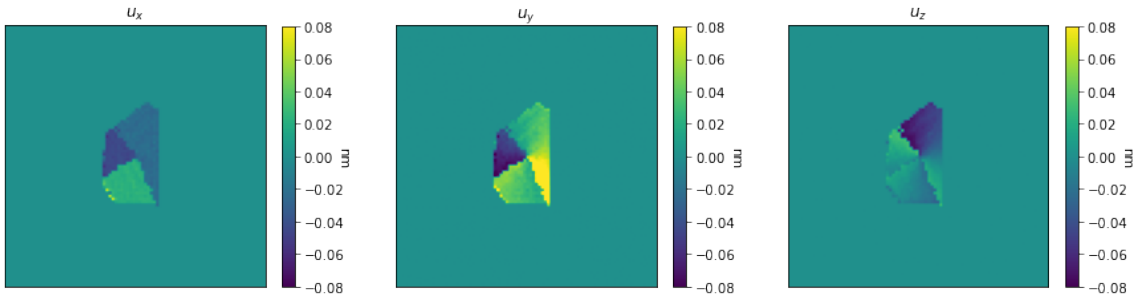


Figure 5.12: Multi-Peak reconstruction where the discontinuities in the phases of each constituent do not agree.

crystals, the most likely reflections that can be measured are the [200] and [111] families. Thus, the phases, given by $\phi(\mathbf{x}) = \mathbf{G}_{hkl} \cdot \mathbf{u}(\mathbf{x})$ will have an offset of $2\pi$ at the discontinuity for each reflection that contains the dislocation. This further complicates matters because phase-retrieval is agnostic to the location of the discontinuity. Given that lattice planes about a dislocation are indistinguishable due to their helical nature, the location of the phase discontinuity is not fixed and different phase retrieval results from different random starts will not necessarily contain phase discontinuities at the same locations.

It has already been demonstrated that CPR provides better reconstructions than IPR when reconstructing dislocations. Gao et al. [25] demonstrated that reconstructing multiple peaks simultaneously can force each constituent reconstruction to reach its global minimum; however, they discussed the difficulty in producing a displacement field which agrees with each reconstruction. This is because it is difficult to align the discontinuities in phase between the multiple reflections. When combining the phases, displacement fields with several discontinuities can be produced, as can be seen in Fig. 5.12. Because each constituent reconstruction is close to its global minimum, combining them doesn't always force the discontinuities to agree. As mentioned previously, the location of the discontinuity is arbitrary and has no bearing on the $\chi^2$ values for each constituent. Thus, it is possible for each constituent to reach its global minimum and still disagree with the other constituents with regard to the location of the phase discontinuity. Though each of the phases used to produce this displacement field are correct, their discontinuities do not align. This result is not physical and cannot easily be used to compute the elastic strain.

### 5.3.1 Comparison of CPR-GA and CPR for Reconstructing Dislocations

It was hypothesized in I that using the CPR-GA algorithm would help force the discontinuities to be consistent between each constituent reconstruction. If the least-squares error $L$ is used as the fitness criterion, and constituents are combined frequently during the CPR process, the individuals with the most agreement between constituents should consistently win. To test this, a multi-peak BCDI dataset was created with a screw dislocation and an edge dislocation. The displacement field about the screw dislocation core is given as

$$u_z = \frac{b}{2\pi} \tan^{-1} \frac{y}{x}, \tag{5.11}$$

where $u_z$ is the displacement in the direction parallel to the Burger's vector, $b$ is the magnitude of the Burger's vector $\mathbf{b}$, and $y$ and $x$ are the coordinates of points in the plane normal to $\mathbf{b}$ [28]. An FCC Cu crystal was used, so the simulated Burger's vector is $\frac{1}{2}[011]$ . This displacement field was then projected along $[111], [1\bar{1}1], [\bar{1}11], [002]$ and $[200]$, and used to simulate Bragg peaks. The phases associated with the forward-model of each reflection can be seen in Fig. 5.14. It can be seen that 3 of the peaks contain a phase field that spans $-\pi$ to $\pi$, because the projection of the Burger's vector along these g vectors results in a displacement of $d$ at the discontinuity line. The other two reflections are not sensitive to the dislocation because because $\mathbf{b} \cdot \mathbf{G}_{hkl} = 0$ for these reflections.

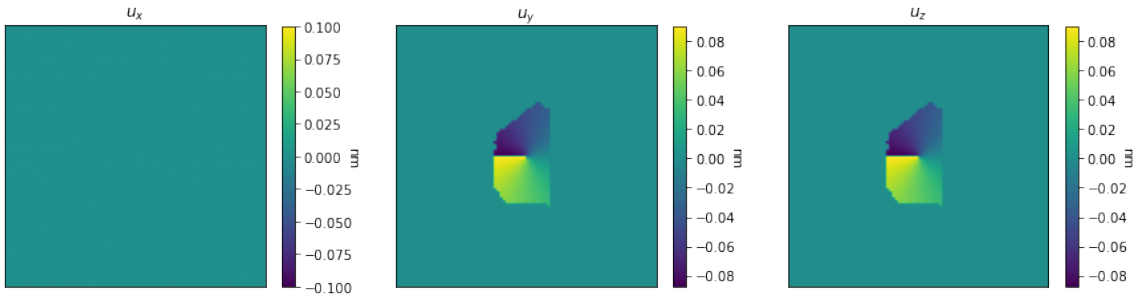


Figure 5.13: Cross section of [011] plane with three components of displacement shown in the crystal frame.

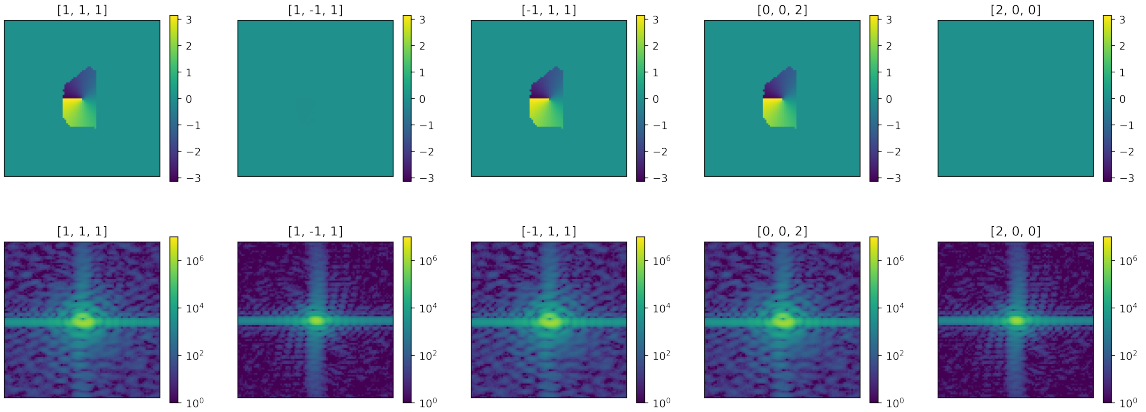


Figure 5.14: Cross section of the Phases associated with each simulated dataset (top) and their corresponding Bragg peaks (bottom) for a screw dislocation

Another simulated dataset was created for a is $\frac{1}{2}[110]$ edge dislocation. The [110] plane in the crystal is shown, with the displacements in the crystal frame. The displacement field about an edge dislocation is

$$u_x = \frac{b}{2\pi}\left[\tan^{-1}\frac{y}{x} + \frac{xy}{2(l-\nu)(x^2+y^2)}\right], \tag{5.12}$$

$$u_y = -\frac{b}{2\pi}\left[\frac{1-2\nu}{2(1-\nu)}\ln(x^2+y^2) + \frac{(x^2-y^2)}{4(1-\nu)(x^2+y^2)}\right], \tag{5.13}$$

where $b$ is the magnitude of the Burger's vector, and $\nu$ is Poisson's ratio for Cu [84, 85]. The same four reflections that were used for the screw dislocation were used for the edge dislocation. The displacement field in the crystal frame as well as the phases and datasets can be seen in Fig. 5.15 and Fig. 5.16 respectively.

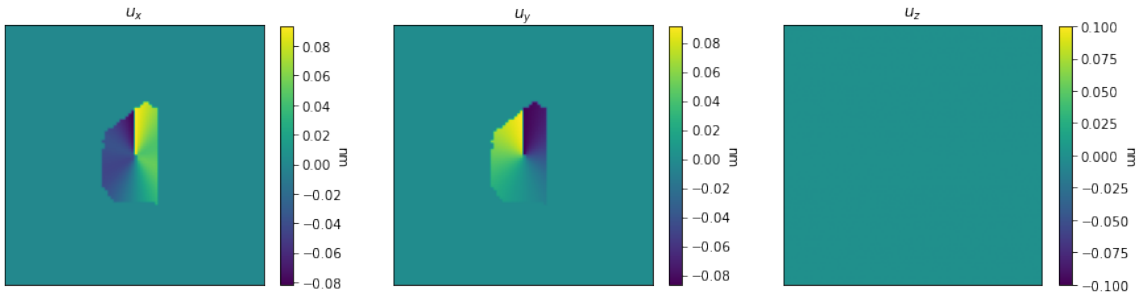


Figure 5.15: Cross section of [110] plane with three components of displacement shown in the crystal frame.

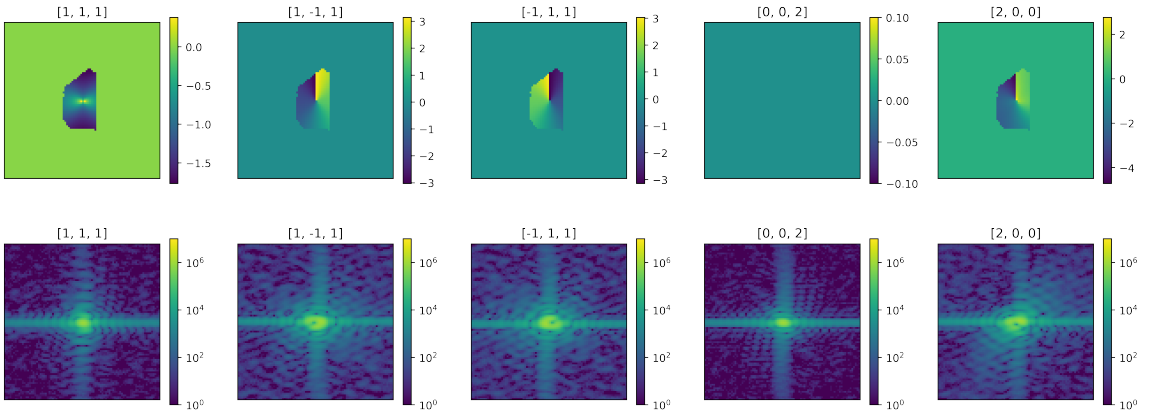


Figure 5.16: Cross section of the Phases associated with each simulated dataset (top) and their corresponding Bragg peaks (bottom) for a edge dislocation

Each dataset was scaled to a photon maximum of $10^6$ and Poisson noise was added. The datasets were forward modeled in a common frame so that the rotation and interpolation described in 5.1.4 was not necessary here. To test the improvement of CPR-GA over generic CPR, two recipes were chosen so that $\chi^2$ converged for each technique. The reconstruction recipes were adapted from the one used in 5.2 because preliminary trials showed that a longer recipe was required, with more frequent combination steps. The basic recipe consisted of 5 iterations of ER followed by 5 iterations of HIO, with constituents being combined every 5 iterations. Every 100 iterations, shrinkwrap was applied to $\overline{\rho}(\mathbf{x})$. For CPR, this procedure was applied for 6000 iterations. For CPR-GA, this procedure was applied for 250 iterations per generation. Eight generations were used, beginning with six individuals and culling to three after the fourth generation.

Thirty reconstructions were completed using each method. The results are displayed in Fig. 5.17. It can be seen that the CPR-GA outperforms the CPR in both $\chi^2$ and $L$ for both edge and screw dislocation cases. By using $L$ as the fitness metric in the GA, individuals with phase discontinuities closer together are favored, and over the course of several generations, the discontinuities are brought to the same location.

A plot of the best reconstructions of the edge dislocation and screw dislocation can be seen in Fig. 5.18 and Fig. 5.19. It must be noted that the best reconstructions from both the CPR and CPR-GA method look comparable to one another. The real benefit to using the CPR-GA is the consistency with which the correct result is returned. Though coupling

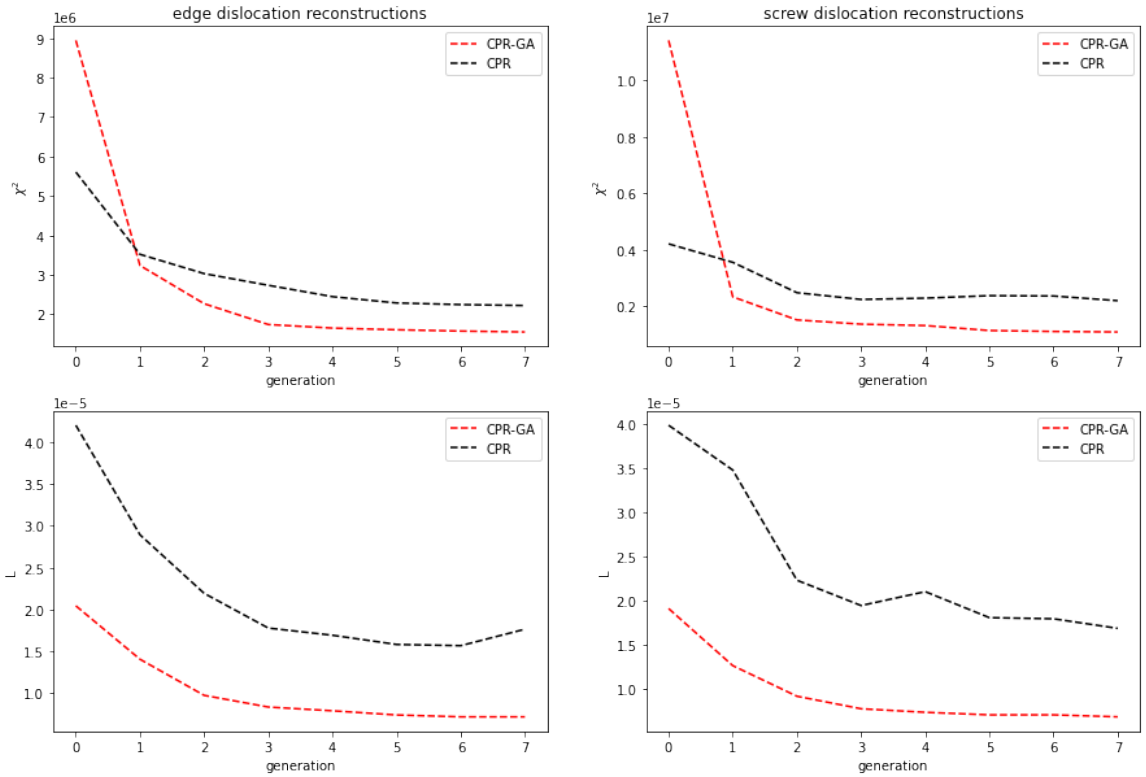


Figure 5.17: Comparison of CPR-GA to CPR for edge and screw dislocations. The plots show the average $\chi^2$ and $L$ values for each method over 30 reconstructions. Recipes of different lengths were required for both techniques to converge with respect to $\chi^2$. 6000 iterations were used for CPR and only 2000 iterations for CPR-GA (250 per generation). For the sake of comparison, the CPR error is recorded at eight equidistant points (every 750 iterations) and plotted next to the CPR-GA error after each generation. Thus, a "generation" in the CPR reconstruction is just 750 iterations of the recipe.

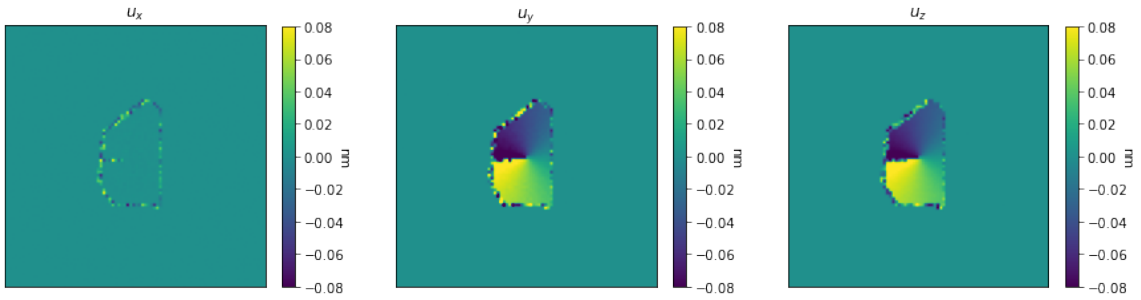


Figure 5.18: Cross section of the best screw dislocation reconstruction produced by CPR-GA. It can be seen that the discontinuity spans only one pixel, meaning each of the phases is in agreement.

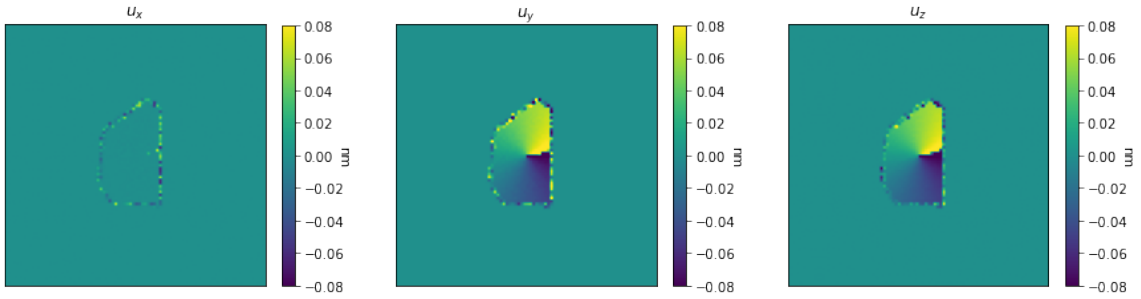


Figure 5.19: Cross section of the best screw dislocation reconstruction produced by vanilla CPR. It can be seen that the discontinuity spans only one pixel, meaning each of the phases is in agreement.

multiple peaks together helps to pull them out of local minima, the previous section showed the benefit of using the GA to ensure that the best result is reached much more frequently. Table 5.1 shows the $\chi^2$, $L$, and success rate for successful dislocation reconstruction. Vanilla CPR returned non-realistic displacement fields, like those seen in Fig. 5.12, 37% of the time for edge dislocations and 53% of the time for screw dislocations, while the CPR-GA only returned non-realistic displacement fields 10% and 3% of the time respectively. It is clear that, in addition to CPR-GA having lower $\chi^2$ and $L$ values on average, it is also more likely to produce the correct solution, *i.e.* where the discontinuity is aligned in all constituents.

For the edge dislocation reconstructions, the CPR-GA showed an improvement of 30.2% in $\chi^2$, 59.7% in $L$, and 26.7% in success rate. The performance gap between the two methods was even larger for screw dislocation reconstructions, where the CPR-GA showed an improvement of 50.8% in $\chi^2$, 59.7% in $L$, and 50% in success rate. This demonstrates that CPR-GA is a clear upgrade over vanilla CPR in its ability consistently reconstruct displacement fields about dislocations. As we move toward collecting datasets with dislocations, reconstructing objects with higher strain will become the norm and techniques such

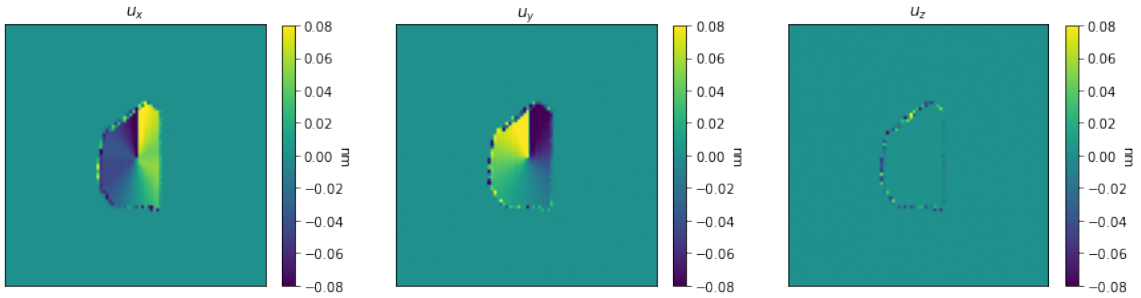


Figure 5.20: Cross section of the best edge dislocation reconstruction produced by CPR-GA. It can be seen that the discontinuity spans only one pixel, meaning each of the phases is in agreement.

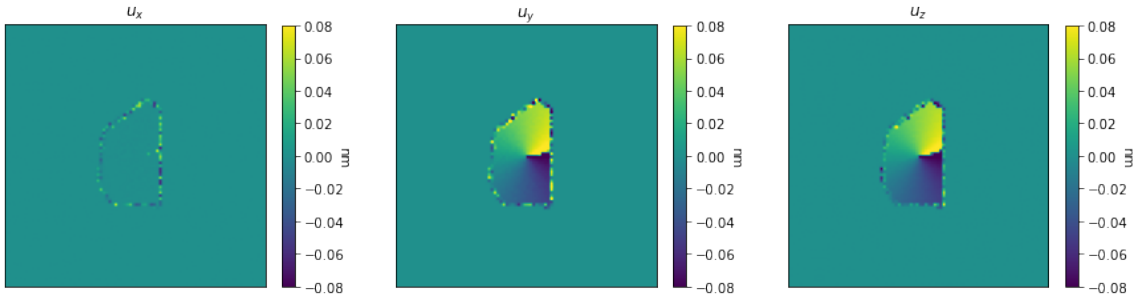


Figure 5.21: Cross section of the best edge dislocation reconstruction produced by vanilla CPR. It can be seen that the discontinuity spans only one pixel, meaning each of the phases is in agreement.

| Dislocation Type | Error metric | CPR | CPR-GA |
|---|---|---|---|
| Edge | $\chi^2$ | $2.22 \times 10^6$ | $1.55 \times 10^6$ |
| Edge | L | $1.76 \times 10^{-5}$ | $7.09 \times 10^{-6}$ |
| Edge | Success Rate | 63.33% | 90.00% |
| Scew | $\chi^2$ | $2.18 \times 10^6$ | $1.68 \times 10^6$ |
| Screw | L | $1.68 \times 10^{-5}$ | $6.79 \times 10^{-6}$ |
| Screw | Success Rate | 46.67% | 96.67% |

Table 5.1: Results from 30 reconstructions of edge and screw dislocation BCDI datasets using CPR and CPR-GA. CPR-GA shows clear improvement over vanilla CPR.

as CPR-GA will likely be needed to accurately resolve the strain and displacement fields.

It must be noted that higher order reflections, such as the [220] family, will produce phase fields with a double phase wrap and two discontinuities. One of these discontinuities should be able to be removed via phase unwrapping techniques, but it is not straightforward how this can be implemented in CPR techniques, as the early displacement fields may contain non-physical phase jumps in certain places which may not play well with phase-unwrapping algorithms. This is out of the scope of this work and will be discussed in Chapter VII.

## 5.4 Discussion

Several CPR routines already exist in the literature, and recent methods developed by Newton et al. [24] and Gao *et al.* [25] have sought to design phase retrieval approaches that utilize multiple Bragg peak data sets in different ways than the routine presented here. Newton et al. use a sequence of HIO steps interleaved with least-squares corrections to the displacement field $\mathbf{u}(\mathbf{x})$ similar to 6.7, and Gao et al. intermittently update $\mathbf{u}(\mathbf{x})$ using an iterative procedure inspired by the bisection method. What has not yet been addressed by these works is the applicability of CPR to experimental data. This is important to consider given that experimental BCDI data of multiple Bragg peaks inevitably contains artifacts from factors such as particle drift, imperfect beam/sample alignment, background scattering, etc. which are not present in simulated data sets and which may adversely effect the performance of CPR strategies.

To handle such imperfections in the data, GA approaches for independent phase-retrieval (like the IPR-GA in this work) are typically necessary to produce the best reconstructions [22], and as such, should be the benchmark by which any CPR approach is judged. In performing such a comparison for simulated and experimental data, we demonstrated that using a GA with a coupled routine is able to outperform an independent GA, contributing to the advancement of this family of techniques.

Additionally, it was demonstrated that the CPR-GA method here is effective for reconstructing the displacement fields of grains with dislocations. By using least-squares error as our fitness metric, we select the individual in each generation whose phases most closely agree with the displacement field and breed it with the others, resulting in reconstructions

with consistent dislocation discontinuity lines throughout all constituents. This agreement in discontinuity allowed these reconstructions to achieve lower $\chi^2$, meaning each constituent reconstruction was more accurate. This will be beneficial for the eventual study of grain boundary dislocations. It is well documented that reconstructing phases with dislocations is a challenging problem and that a genetic algorithm makes this task simpler. By extending this to coupled phase retrieval, we lay the groundwork for future reconstructions of experimental data of dislocations.

Given the nascent state of research in this field, it can be imagined that more sophisticated CPR strategies will be developed, and the use of genetic algorithms as implemented here promises to improve the robustness of such strategies in the context of experimental reconstructions.

Finally, this algorithm lays the groundwork for a similar Multi-Grain reconstruction algorithm which will be described in Chapter VI. Unless the full displacement field is reconstructed, no real study of grain boundary stress and strain can be conducted. These CPR and CPR-GA methods make it possible to accurately reconstruct the displacement fields, so the multi-grain reconstruction routine is theoretically possible.

CHAPTER VI

# Multi-Grain BCDI

## 6.1 Introduction

With the ability of modern coherent x-ray facilities to orient crystals at the beamline, potential exists for BCDI on neighboring grains within a microstructure or on isolated bicrystals. Such experiments would allow for the study inter-granular phenomena such as grain boundary dislocations, slip transmission, twinning, and grain boundary evolution under load. Single-reflection BCDI has been demonstrated as a tool for 3D imaging of dislocations and other defects, but at its best, can only provide projections of lattice strain, making it impossible to construct a meaningful strain field between two neighboring crystals. With the advent of multi-reflection BCDI, it is possible to retrieve the full displacement field, and thus the strain field, from individual grains, making it possible to study grain boundary phenomena. Typically, however, the boundary voxels of a crystal are difficult to resolve due to difficulties constraining the crystal volume. While this is inconsequential in single-crystal BCDI, when defects such as dislocations are studied primarily within the grain volume, it becomes problematic when studying bi-crystals and grain boundaries. One of the facets in each domain in a bi-crystal is necessarily a grain boundary, and inaccurate reconstructions at grain boundary voxels will significantly complicate the study of grain boundary strains.

To rectify this, we propose a multi-grain reconstruction method which takes advantage of grain boundary continuity conditions to improve reconstructions of neighboring grains. Just as the CPR algorithm took advantage of multiple Bragg peaks to further constrain single-grain reconstruction, this algorithm uses grain boundary morphology and displacement

field continuity to constrain the grain boundary voxels of each coupled reconstruction. In its current state, the algorithm we propose requires a flat grain boundary and knowledge of the grain boundary plane in each crystal. This assumption is not unreasonable for the types of bi-crystal datasets it is feasible to collect at current synchrotron sources. Given the coherence-length limits on grain size for BCDI at 1-ID and 34-ID at the APS (235 nm and 1 $\mu$m respectively), neither the Laue diffraction microscopy method at 34-ID nor far-field HEDM at 1-ID have the resolution to accurately provide a spatial map of any polycrystalline samples. This issue should be partially resolved after the APS-U, when the coherence length of each beamline will increase, but it is likely that determination of neighboring grain positions will remain difficult. Thus, there are currently two methods being pursued for studying grain boundaries using BCDI: using a FIB to carve and mount isolated bicrystals from a polycrystal with grain sizes $\sim 200\mu$m or de-wetting nanocrystals onto a single-crystal substrate.

In the case of the FIB-ed bi-crystal (described in chapter IV), it is relatively easy to orient and locate the bicrystals at the beamline because only two crystals are illuminated by the beam. Because of coherence-length requirements, the bicrystal contains only a small part of each crystal on either side of the grain boundary. The polycrystals from which these bicrystals are FIB-ed contain grain sizes above $200\mu$m, so the curvature at the grain boundary for an $800nm$ segment will be approximately planar and thus sufficient for our routine.

For twinned crystals all that is needed is an orientation list of all grains in the sample, which can be determined via HEDM or Laue diffraction. Each domain in the twin can be determined from an orientation list by calculating the misorientation between all crystals and searching for pairs misoriented by 60° about a [111] axis, as mentioned in Chapter III. The twin boundary is necessarily planar, though their may be steps in the surface. The de-wetted nanocrystals typically used for BCDI often contain twins with no steps and have been measured in several previous works [86, 87]. Given these realities, it is not unreasonable to assume a flat crystal boundary. While this is certainly an assumption which simplifies things considerably, it will be discussed in future sections how any new method for determining grain boundaries could easily be inserted into the described approach.

### 6.1.1 Boundary Conditions

The two boundary conditions considered in this approach are the continuity of displacement and the continuity of shape. BCDI measurements, with resolution in the tens of nanometers, measure the average behavior of tens of thousands of atoms. Thus we will assume a continuum mechanical regime for all material points within a single grain. The fundamental assumption of continuum mechanics is that the material volume is continuous at all points. This assumption fails at the atomic level, where atomic positions are discrete, but at the scales represented by voxels in BCDI reconstructions, thousands of atoms are described by a single value. According to small deformation theory, a deformation of a material point $\mathbf{x}$ within a body can be described by the continuous mapping

$$\mathbf{x}' = f(\mathbf{x}). \tag{6.1}$$

$\det\nabla f$ represents the volume per unit cell after deformation of the body. Because the body cannot penetrate itself and chirality must be conserved, $\det\nabla f \neq 0$ and $\det\nabla f > 0$, so $f(\mathbf{x})$ must be continuous [88]. It is helpful to write $f(\mathbf{x})$ as the sum of a reference position and displacement $\mathbf{x}' = \mathbf{x} + \mathbf{u}(\mathbf{x})$. From this formulation, it follows that $\mathbf{u}(\mathbf{x})$ must be continuous. If deformations are small and displacements are continuous and single-valued, elastic strain can be calculated from $\mathbf{u}(\mathbf{x})$ according to $\varepsilon = \frac{1}{2}[\nabla\mathbf{u}(\mathbf{x}) + [\nabla\mathbf{u}(\mathbf{x})]^{\mathbf{T}}]$. Upon this assumption are based all of the strain compatibility equations, and it is the fundamental building block for the theory of linear elasticity.

At the macroscale, materials are considered homogeneous, and microstructure is only accounted for in a statistical sense, given that a single volume element will contain many grains. At the length scale of BCDI, however, materials points are only considered homogeneous within each grain. Here, polycrystalline materials must be treated as composites, where different grains possess different elastic properties. The misorientation of lattices at the grain boundary mean that the elastic constants along a particular axis on either side of the grain boundary are different. Such an interface can be seen in fig. 6.1. In linear elasticity theory, the boundary conditions across a perfectly-bonded, composite interface (in 2D)

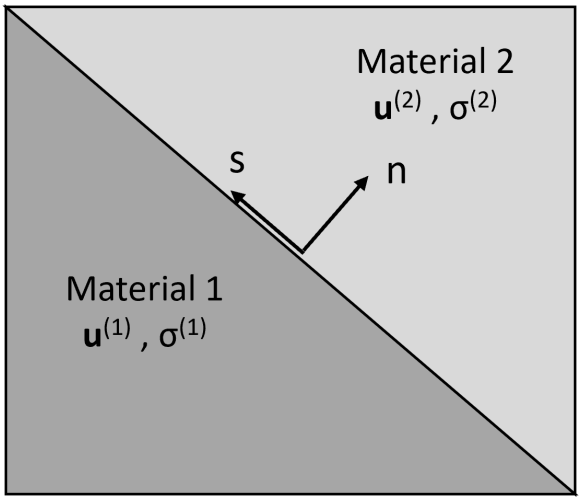


Figure 6.1: 2D composite interface, such as a grain boundary.

are as follows [89]:

$$u_n^{(1)} = u_n^{(2)} \qquad u_s^{(1)} = u_s^{(2)} \tag{6.2}$$

$$\sigma_n^{(1)} = \sigma_n^{(2)} \qquad \tau_s^{(1)} = \tau_s^{(2)} \tag{6.3}$$

Where $u_n^{(1)}$ and $u_n^{(2)}$ are the displacements normal to the boundary for grains 1 and 2, $u_s^{(1)}$ and $u_s^{(2)}$ are the displacements tangent to the boundary, $\sigma_n^{(1)}$ and $\sigma_n^{(2)}$ are the stresses normal to the boundary, and $\tau_s^{(1)}$ and $\tau_s^{(2)}$ are the shear stresses at the boundary. This extends to 3 dimensions by enforcing both components of displacement in the boundary as well as both shear stresses. If such an interface is perfectly bonded (no cracks, voids, or grain boundary sliding), then both displacements and tractions must be continuous across the grain boundary. A coherent twin boundary is one of the most perfectly bonded grain boundaries, given the one-to-one bonding of atoms across the boundary, so these conditions should hold. Of these two requirements, the displacement boundary condition is the simplest to use for multi-grain BCDI because displacement is readily available from CPR. If stress boundary conditions were used, gradients would have to be computed to find the stress, the stress fields would be aligned, and the new displacement fields would have to be found by numerical solving of the partial differential equations relating displacement to stress. This would be computationally costly and would likely lead to the propagation of error from numerical solvers. Given that we already operate in displacement space for multi-peak

phase retrieval, we will use the displacement continuity condition in our algorithm.

## 6.2 Multi-Grain BCDI

The multi-grain BCDI phase reconstruction approach we developed consists of two parallel CPR reconstructions which are intermittently brought into agreement at the grain boundary with regard to both shape and displacement fields. A diagram of the algorithm can be seen in Fig. 6.2. The basic steps are as follows:

1. Reconstruct both grains using CPR
2. add displacement ramp to account for grain-average strain
3. transform displacement field from crystal frame to sample frame
4. determine grain boundary and update supports
5. compute mean displacement offset to bring fields into agreement
6. Enforce local displacement continuity at each boundary voxel
7. transform displacement field from sample frame back to crystal frame
8. subtract displacement ramp
9. repeat using new $\mathbf{u}(\mathbf{x})$ and supports for CPR

The determination of the grain boundary without *a priori* knowledge is easily the most difficult step in this routine. For the sake of simplicity, we present a reconstruction technique for a coherent FCC twin, one of the most common grain boundary types in FCC metals. The advantages of using a twin system will be discussed in 6.2.3.

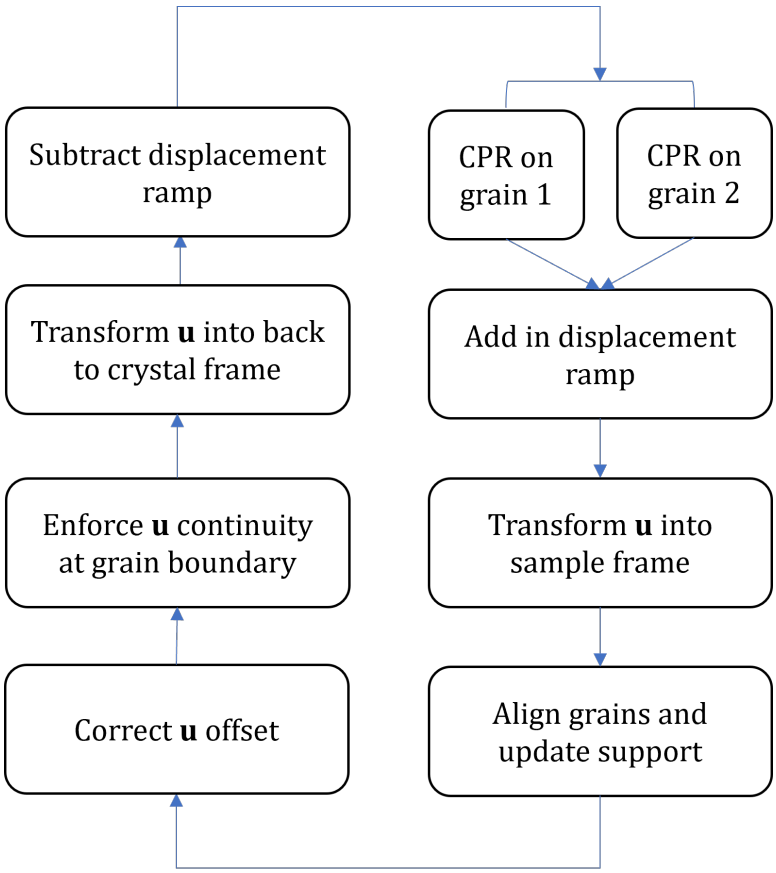


Figure 6.2: Multi-Grain BCDI algorithm

### 6.2.1 Correct Displacement Ramp

The first step involves adding in displacement ramps which are inherently missing from BCDI datasets. The displacement field returned from a CPR reconstruction corresponds to strain perturbations about the grain-average strain. Because the diffraction patterns are centered in the array during phase retrieval, we do not know how far the Bragg peak has shifted in $2\theta$ from its nominal unstrained position, and the phase ramps corresponding to the average change in lattice spacing for each reflection are lost. This results in a displacement field which is missing a linear displacement ramp, corresponding the grain-averaged strain. This rarely matters in the case of single grain BCDI but becomes important for multi-grain BCDI because displacement ramps must be accounted for to reproduce the correct displacement field across the boundary. The relationship between the actual displacement field $\mathbf{U}(\mathbf{x})$ and the one returned during CPR $\mathbf{u}(\mathbf{x})$ is given as

$$\mathbf{U}(\mathbf{x}) = \mathbf{u}^{vol}(\mathbf{x}) + \mathbf{u}(\mathbf{x}) \tag{6.4}$$

where $\mathbf{u}^{vol}(\mathbf{x})$ is the linear displacement ramp. $\mathbf{u}^{vol}(\mathbf{x})$ can be calculated by finding the change in the diffraction angle $2\theta$ for each measured reflection from BCDI. Bragg's law can be expressed as $d = \frac{\lambda}{2\sin(\theta)}$. So $\Delta d$, corresponding to the change in lattice parameter projected along the scattering vector, can be found according to

$$\Delta d = \frac{\lambda}{2\sin(\theta)} - d_0 \tag{6.5}$$

where $d_0$ is the distance between lattice planes int the unstrained crystal, $\lambda$ is the wavelength of the x-ray source, and $\theta$ is the scattering angle. This $\Delta d$ results in a phase ramp for each reflection measured in BCDI, which can be calculated on a discrete voxel-by-voxel basis as

$$\phi^{vol}_{hkl}(\mathbf{x}_n) = \frac{\Delta d}{d_0}(\mathbf{x}_n \cdot \mathbf{G}_{hkl}) = \mathbf{u}^{vol}(\mathbf{x}_n) \cdot \mathbf{G}_{hkl}, \tag{6.6}$$

where $\phi^{vol}_{hkl}(\mathbf{x}_n)$ is the projection of $\mathbf{u}^{vol}(\mathbf{x}_n)$ onto the scattering vector $\mathbf{G}_{hkl}$ at voxel $n$. Because we have more than three reflections, we perform ordinary least-squares to determine the best-fit $\mathbf{u}^{vol}(\mathbf{x}_n)$,

$$\mathbf{u}^{vol}(\mathbf{x}_n) = (g^T g)^{-1} g^T \tilde{\phi}^{vol}(\mathbf{x}_n) \tag{6.7}$$

where $\tilde{\phi}^{vol}(\mathbf{x}_n)$ is an $m \times 1$ array of the $\phi^{vol}_{hkl}(\mathbf{x}_n)$ values for all $m$ reflections, and $g$ is an $m \times 3$ matrix of all the $\mathbf{G}_{hkl}$ vectors for each reflection. This new $\mathbf{u}^{vol}(\mathbf{x})$ field is added to the reconstructed $\mathbf{u}(\mathbf{x})$ for each grain, giving the complete crystal-frame displacement $\mathbf{U}(\mathbf{x})$.

### 6.2.2 Reorientation of grains

To compare displacement fields, both grains must be in a common frame. BCDI datasets are not collected on a uniform grid, just as in section 5.1.4. For CPR, it was discussed that all reconstructions must be rotated into a common crystal frame and interpolated onto a common regular grid so that the phases can be combined to calculate $\mathbf{u}(\mathbf{x})$. Because CPR requires a transformation between the crystal frame of the reconstructed object and the

detector frames of the BCDI datasets each time $\mathbf{u}(\mathbf{x})$ is computed, it is simpler to rotate and interpolate the datasets themselves onto a common grid, rather than the reconstructed objects. In Multi-Grain BCDI, we will rotate all the datasets from each grain into a common orthogonal sample frame.

For ease of aligning both grains in a twin reconstruction, it is beneficial to construct a sample frame where the twin plane is normal to one of the axes of the frame, allowing us to easily enforce boundary conditions. An FCC twin system consists of two grains related to each other by a 60° twist about an axis in the [111] family. The orientation of each crystal must already be known in order to measure multiple Bragg peaks from each (as discussed in Chapter III), and the two orientations can be used to determine the common twin plane. The rotation matrices which transform grain one and grain two from their respective crystal frames to the sample frame are given as $o_1$ and $o_2$. In this routine the datasets will be transformed again so that the twin-plane normal $\hat{r}_{twin}$ is aligned with the [010] direction in the sample frame. This transformation is described by a rotation $\theta$ around the axis $\hat{a}$ given as follows:

$$\hat{a} = [010] \times \hat{r}_{twin}, \tag{6.8}$$

$$\theta = cos^{-1}([010] \cdot \hat{r}_{twin}). \tag{6.9}$$

An orientation matrix $o'$ can be assembled from $\hat{a}$ and $\theta$. Though the data has been rotated into the sample frame, the corresponding displacement fields $\mathbf{U}_1(\mathbf{x})$ and $\mathbf{U}_2(\mathbf{x})$ are necessarily given in the crystal frames of grains 1 and 2 respectively. The sample frame displacements are related to the crystal frame displacement by the following:

$$\mathbf{U}_1^s(\mathbf{x}_n) = o' o_1 \mathbf{U}_1^c(\mathbf{x}_n) \tag{6.10}$$

$$\mathbf{U}_2^s(\mathbf{x}_n) = o' o_2 \mathbf{U}_2^c(\mathbf{x}_n) \tag{6.11}$$

where the superscript $s$ denotes the sample frame and the superscript $c$ denotes the crystal frame and $n$ is a single voxel. $\mathbf{U}_1^s(\mathbf{x}_n)$ and $\mathbf{U}_2^s(\mathbf{x}_n)$ are now in the same reference frame and can be compared to one another at the boundary.

### 6.2.3 Determining Twin Boundary and Aligning Grains

Now that the grains have been transformed into a common sample frame, they must be aligned along the twin boundary. Because the orientation of each crystal is known, there remain only three degrees of freedom for alignment: translation in sample $x$, sample $y$ and sample $z$. For the FCC twin case assumed here, it is known *a priori* that the boundary between the two grains must be a single plane. Thus, one of the sides of each reconstructed grain must be a plane normal to sample $[0, 1, 0]$. To find the possible twin boundary planes, the $n$th discrete difference is taken across the reconstructed amplitudes $\overline{\rho}_1(\mathbf{x})$ and $\overline{\rho}_2(\mathbf{x})$ in the $[0, 1, 0]$ direction. This difference can be seen in Fig. 6.3.

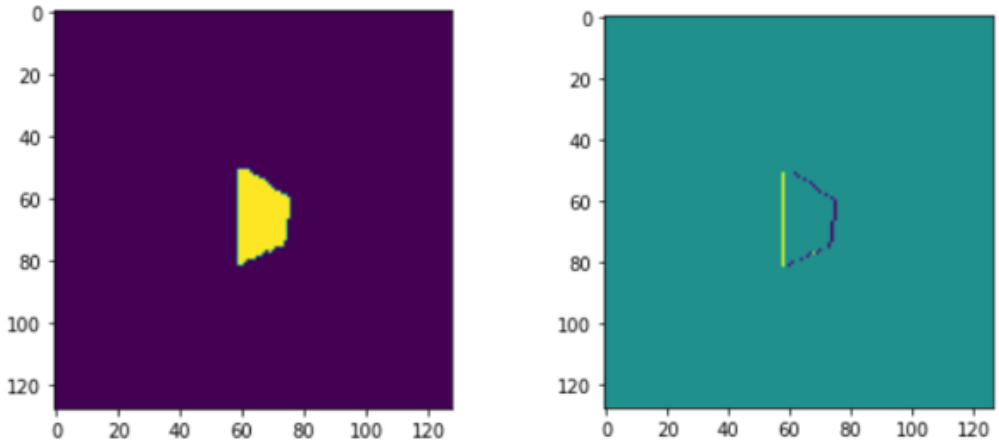


Figure 6.3: Cross section of Grain amplitude after nth difference is taken. It can be seen that the right boundary is clearly defined. This boundary is perfect and there are no low-amplitude voxels, but in a real dataset, these voxels would be bypassed due to the high intensity of the amplitude at the actual boundary.

Taking the $n$th difference across the twin plane normal direction provides a rough outline of the grain volume. The voxels corresponding to the largest and smallest values correspond to likely boundary voxels because they neighbor voxels with low amplitude. To find the most-likely twin boundaries in each grain, the sum of this difference matrix is then taken across the $x$ and $z$ dimensions of the reconstruction array, given as

$$h_i(y) = \sum_{x=0}^{N} \sum_{z=0}^{N} \text{diff}_y(\overline{\rho}(x, y, z)) \quad i \in [1, 2] \tag{6.12}$$

$h_i(y)$ is now a 1-D array of values whose maximum and minimum correspond to the $y$

coordinate of the two possible boundaries for grain $i$. One of these boundaries will not be the twin boundary, but both sides must be checked. By applying this technique to the amplitude, rather than the support, we aim to exclude low-fidelity voxels in the support near the grain boundary. The shrinkwrap [46] approach used to shrink the object support during phase-retrieval does not allow for precise determination of the grain boundary, and it is common to see spurious phase and displacement values at the boundary at voxels. This technique should avoid said voxels because of their low amplitudes and the high-amplitude boundary will be highlighted as the boundary where the largest difference between neighboring amplitudes occurs. An example of the possible boundaries in two grains can be seen in Fig. 6.4

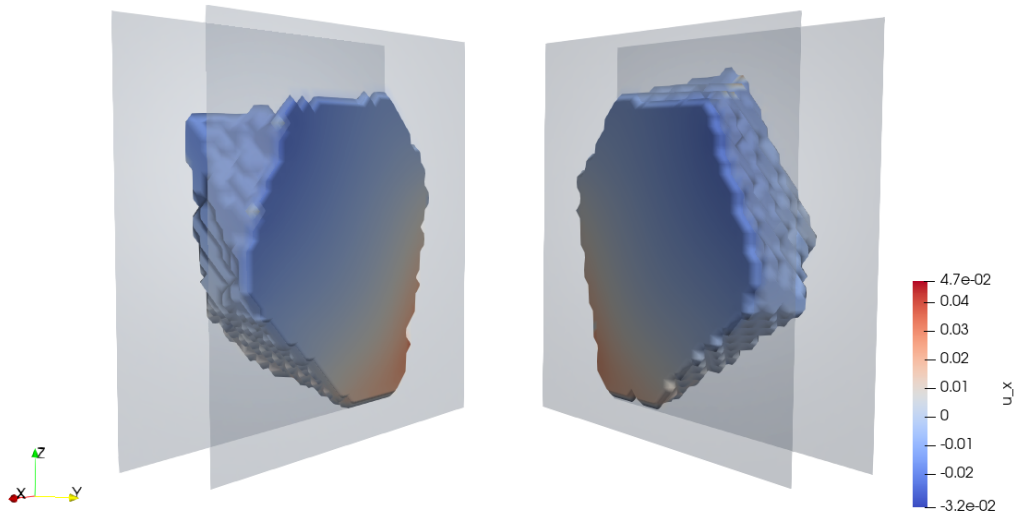


Figure 6.4: Example of boundary pair that does match

The two possible boundaries in each grain will be denoted by the superscripts $L$ and $R$, corresponding to the left and right sides of the grain in the sample frame. The four possible boundaries for grains 1 and 2 will be denoted by $b_1^L$,$b_1^R$, $b_2^L$ and $b_2^R$, which can be seen in Fig. 6.4. Because the orientation of the grains is fixed, there are only two possible boundary pairs: $b_1^L - b_2^R$ and $b_1^R - b_2^L$. These pairs can be seen in Figs. 6.5 and 6.6.

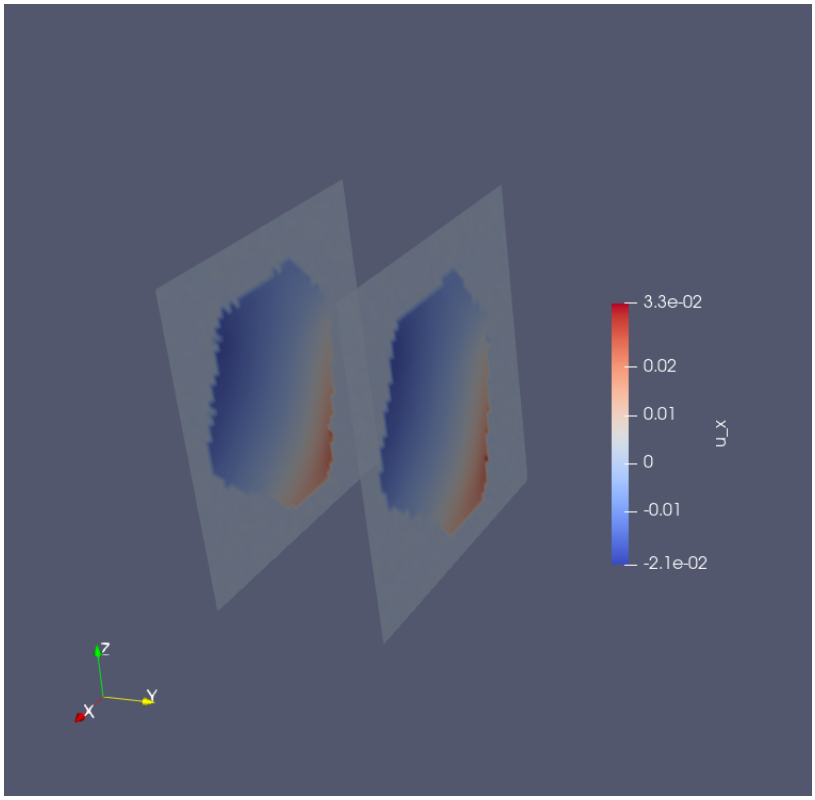


Figure 6.5: Example of boundary pair that does match

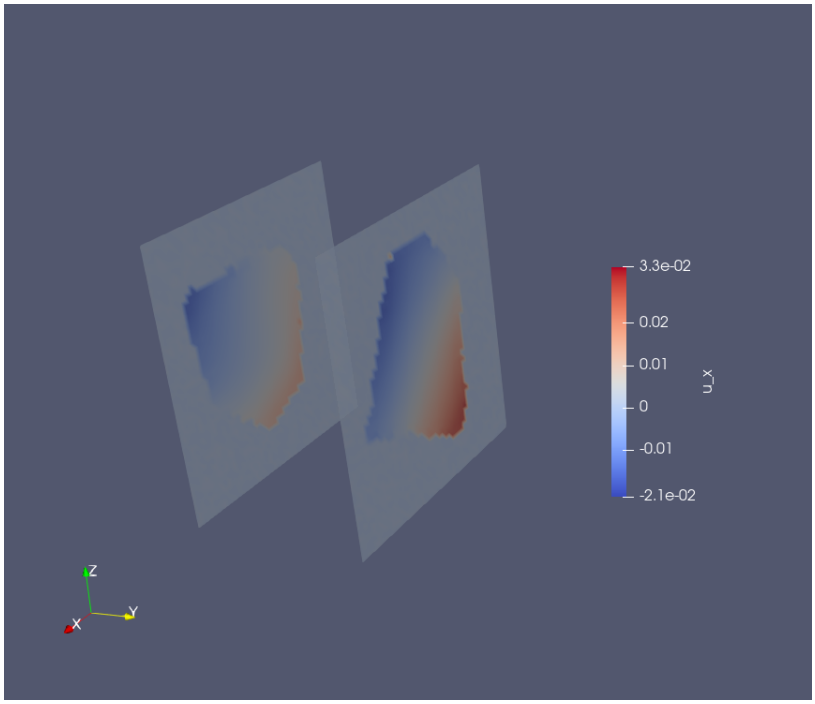


Figure 6.6: Example of boundary pair that does not match.

To determine which is the correct boundary pair, we make use of two interface conditions. The first requires that the shapes of the supports on either side of the interface must match, $S_1(x, b, z) \approx S_2(x, b, z)$, and the second requires that the displacement fields be continuous across the boundary. To easily match both conditions, we define a complex vector field, with the amplitude of each component being the support and the angle being the corresponding displacement component: $\mathbf{M}(\mathbf{x}) = [S(\mathbf{x})e^{iU_x(\mathbf{x})}, S(\mathbf{x})e^{iU_y(\mathbf{x})}, S(\mathbf{x})e^{iU_z(\mathbf{x})}]$. Because we only want to align the boundaries, we extract boundary objects $B^b(\mathbf{x}) = S^b(\mathbf{x})\mathbf{M}(\mathbf{x})$ by multiplying $\mathbf{M}(\mathbf{x})$ by a shape function containing only the boundary voxels: $S^b(\mathbf{x}) \;\; b \in b_1^L, b_1^R, b_2^L, b_2^R$. Because BCDI returns displacements which are zero-centered, displacements on opposite sides of the boundary will not be continuous without accounting for some constant displacement offset. For the purposes of alignment, the displacements in the $B^b(\mathbf{x})$ fields are centered about zero, meaning $B^1(\mathbf{x})$ should approximately equal $B^2(\mathbf{x})$ for the correct boundary pair.

To determine the optimum boundary pair, the cross correlation of each object $B^b(\mathbf{x})$ is taken with its corresponding object for the other boundary.

$$R_m(\xi) = B_m^1(\mathbf{x}) \star B_m^2(\mathbf{x}) \qquad m \in [x, y, z] \tag{6.13}$$

The sum of the maximum values across each cross-correlation matrix $R_m(\xi)$ serves as a fitness metric for each boundary pair. This value is calculated for all of the possible boundary pairs and the pair corresponding to the maximum fitness is selected. Using a common DFT registration trick [90], the distance between location of the maximum voxel in the cross-correlation array and the center of the array can be used as the translation required to move grain boundary 1 into alignment with grain boundary 2, $\vec{r}$ given as

$$\vec{r} = \frac{argmax(R_x) + argmax(R_y) + argmax(R_z)}{3}. \tag{6.14}$$

Grain 2 is then translated by the vector $\vec{r}$ so that it is aligned with Grain 1. The bicrystal is then centered in the array. To update the support functions of each grain, the overlapping

regions of the object amplitudes are corrected according to

$$S(\mathbf{x}) = \begin{cases} S_1(x,y,z), & \text{if } y < b_1, \\ S_2(x,y,z), & \text{otherwise.} \end{cases} \tag{6.15}$$

This ensures that the two grain domains do not overlap and that a clean grain boundary exists between the two crystals.

Phase retrieval twins also have to be accounted for. For each CPR reconstruction, there are two possible solutions, corresponding to two complex-conjugate phase-retrieval twins [78]. For every object $\mathbf{M}(\mathbf{x})$ there is a corresponding phase-retrieval twin $\mathbf{M}^*(\mathbf{x})$. It is impossible to tell, without *a priori* knowledge, which of these phase retrieval twins is the true object. In bi-crystal BCDI, it necessary to ensure that the support and displacement from grain 1 is consistent with those from grain 2 so that the relative orientation of the two grains is correct. In other words, $\mathbf{M}_1(\mathbf{x})$ must be aligned with $\mathbf{M}_2(\mathbf{x})$, and not $\mathbf{M}_2^*(\mathbf{x})$. Because it is impossible to tell which of the phase retrieval twins is which, it is necessary to compare the reconstruction of grain 1 with both possible phase-retrieval twins from grain 2 to see which alignment is best. This increases the possible boundary pairs from two to four ($b_1^L$ and $b_2^R$, $b_1^R$ and $b_2^L$, $b_1^L$ and $b_2^{*R}$, $b_1^R$ and $b_2^{*L}$).

### 6.2.4 Enforcing Displacement Field Continuity

Once the grains are aligned, the displacement continuity condition can be enforced by bringing the two displacement fields into accord. As previously mentioned, the displacement fields from BCDI are zero-centered. Before we can enforce displacement continuity, we must account for a global displacement offset between the two grains by shifting the displacement field in grain 2 by a constant $\Delta U$ such that the average displacements across the boundary are continuous. This means that $\overline{\mathbf{U}}_1(x, b_1 + 0.5\Delta y, z) = \overline{\mathbf{U}}_2(x, b_2 - 0.5\Delta y, z)$ where $b_1$ and $b_2$ are the $y$ positions of the left and right sides of the grain boundary, and $\Delta y$ is the step size in $y$. Because the displacement field is discrete-valued and cell-centered, we must extrapolate

to find these boundary values. Therefore

$$\mathbf{U}_1(x, b_1 + 0.5\Delta y, z) = 0.5\Delta y \frac{\mathbf{U}_1(x, b_1, z) - \mathbf{U}_1(x, b_1 - \Delta y, z)}{\Delta y} + \mathbf{U}_1(x, b_1, z) \tag{6.16}$$

$$\mathbf{U}_2(x, b_2 - 0.5\Delta y, z) = 0.5\Delta y \frac{\mathbf{U}_2(x, b_2, z) - \mathbf{U}_2(x, b_2 + \Delta y, z)}{\Delta y} + \mathbf{U}_2(x, b_2, z) \tag{6.17}$$

$$\Delta U = \frac{\sum_{x=1}^{N}\sum_{z=1}^{N} \mathbf{U}_1(x, b_1 + 0.5\Delta y, z)}{\sum_{x=1}^{N}\sum_{z=1}^{N} S_1(x, b_1 + 0.5\Delta y, z)} - \frac{\sum_{x=1}^{N}\sum_{z=1}^{N} \mathbf{U}_2(x, b_2 - 0.5\Delta y, z)}{\sum_{x=1}^{N}\sum_{z=1}^{N} S_2(x, b_2 - 0.5\Delta y, z)} \tag{6.18}$$

$\Delta U$ is then added to every voxel in $\mathbf{U}_2(\mathbf{x})$, bringing the grain displacement fields into alignment. A plot of the displacement values for a single path across the grain boundary can be seen in Fig. 6.7. This ensures that the average displacement is continuous across the grain boundary, but it does not enforce continuity at every grain boundary voxel. To enforce this condition, every boundary voxel is corrected individually according to

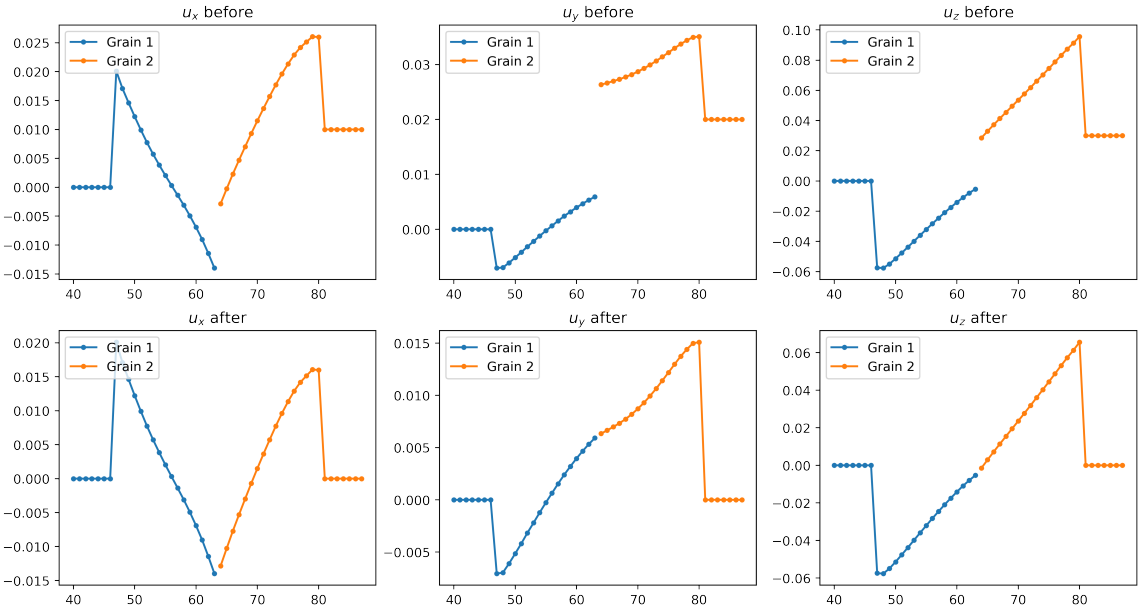


Figure 6.7: A single line of the Displacement Field before and after accounting for displacement offsets.

$$\Delta U(x_n, z_n) = \mathbf{U}_1(x_n, b_1 + 0.5\Delta y, z_n) - \mathbf{U}_2(x_n, b_2 - 0.5\Delta y, z_n), \tag{6.19}$$

$$\mathbf{U}_1(x_n, b_1, z_n) = \mathbf{U}_1(x_n, b_1, z_n) - 0.5\Delta U(x_n, z_n), \tag{6.20}$$

$$\mathbf{U}_2(x_n, b_2, z_n) = \mathbf{U}_2(x_n, b_2, z_n) + 0.5\Delta U(x_n, z_n), \tag{6.21}$$

so that continuity holds at every voxel. An alignment on simulated crystals can be seen in Fig. 6.8. This updates the guess for the displacement field, pulling each reconstruction closer to the true solution. It is hypothesized that over several iterations throughout the multi-grain reconstruction algorithm, the two grains should agree more and more closely.

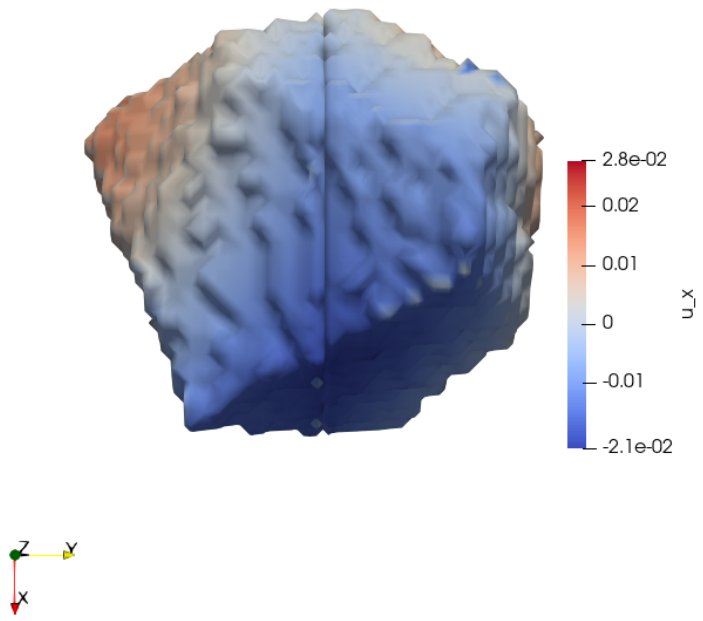


Figure 6.8: x-component of the displacement field in aligned crystal

After the completion of this step, $\mathbf{U}_1(\mathbf{x})$ and $\mathbf{U}_1(\mathbf{x})$ are transformed back into their respective crystal frames and the displacement ramps for each $\mathbf{u}_1^{vol}$ and $\mathbf{u}_2^{vol}$ are subtracted out. The resulting displacement fields are now used to seed the next round of CPR and the Multi-Grain BCDI algorithm repeats.

## 6.3 Validation of Multi-Grain Algorithm

### 6.3.1 Validation on Simulated Data

It was hypothesized in Chapter II that by reconstructing the two grains simultaneously and applying the alignment procedure at specified iterations throughout the process, recon-

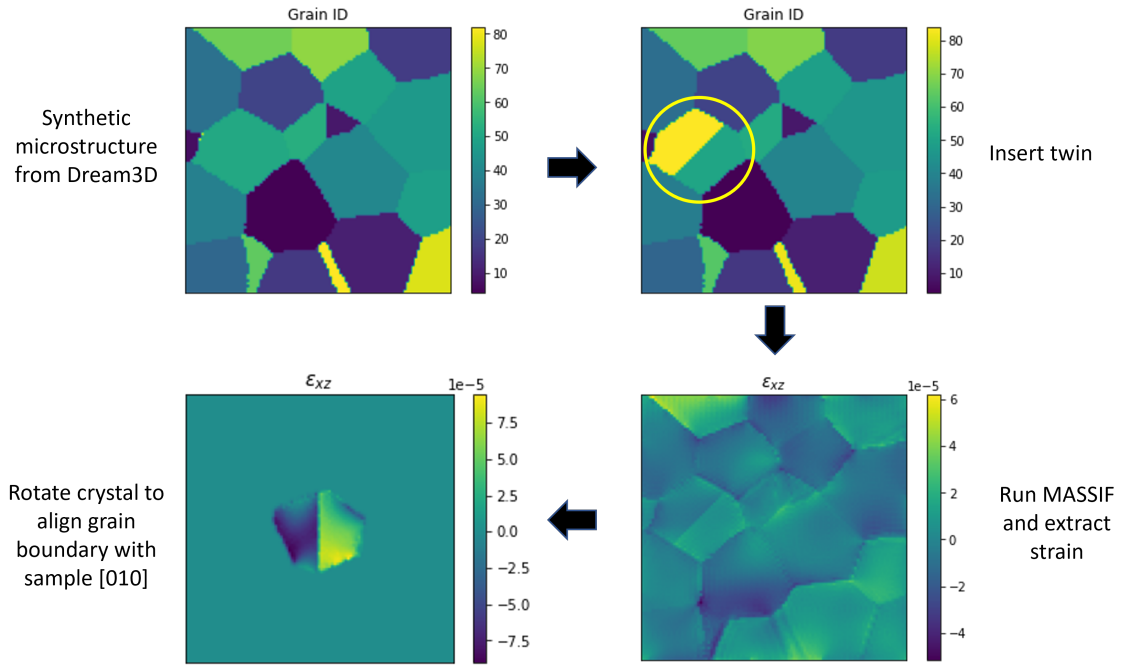


Figure 6.9: Workflow to create synthetic grain with realistic strain fields

struction fidelity can be improved by 10%. This hypothesis was tested by comparing 100 reconstructions where this alignment was applied throughout the CPR reconstruction recipe to 100 reconstructions where alignment was only applied after CPR as a post-processing step.

A synthetic dataset was created using Dream3D software to simulate a polycrystalline microstructure. To simulate a twin, an 800 nm grain was selected from within the microstructure, bisected along its $[1, 1, 1]$ plane, and the orientation of one half of the grain was rotated 60° about the plane normal, giving a coherent FCC twin. A macroscopic strain of $3 \times 10^{-4}$ was applied, and the MASSIF micro-mechanical analysis code [73, 91] was used to calculate the local strain field within the microstructure. The twin grains were extracted from the microstructure and rotated so that the twin boundary was orthogonal to the $[0, 1, 0]$ direction in the sample frame. The elastic strain is also transformed into this sample frame (Fig. 6.10).

MASSIF enforces stress equilibrium at every voxel in the mircrostructure volume. The only accessible outputs from the code are stress and strain. Since displacement fields are needed in order to forward-model a BCDI dataset, we must infer the displacement fields from

the strain fields. As a reminder, elastic strain is related to displacement according to $\varepsilon = \frac{1}{2}[\nabla \mathbf{u}(\mathbf{x}) + [\nabla \mathbf{u}(\mathbf{x})]^{\mathbf{T}}]$. Solving the differential equation to calculate the exact displacement from strain is difficult due to the large number of partial derivatives contained in the elastic strain tensor. To sidestep this, given the computational resources available, an optimization problem was constructed and solved using the Adam optimizer in TensorFlow 2.7 [92]. The cost function constructed is as follows:

$$\Omega = \sum_{n=0}^{N} (\frac{1}{2}[\nabla \mathbf{u}_n + [\nabla \mathbf{u}_n]^{\mathbf{T}}] - \varepsilon_n)^2 \tag{6.22}$$

where $n$ is the index of a single voxel in the array. Minimizing this cost function results in a displacement field which produces the appropriate strain field. The optimized displacement field can be seen in Fig. 6.10 It can be seen in Fig. 6.11 and Fig. 6.12 that the strain field calculated from the inferred displacement field matches the MASSIF strain field well. To determine the displacement ramp, the average strain was calculated for each grain and the optimization routine used to calculate the corresponding displacement field for each grain. These displacement ramps were then subtracted from each of the displacement fields. An example displacement ramp can be seen in Fig. 6.13

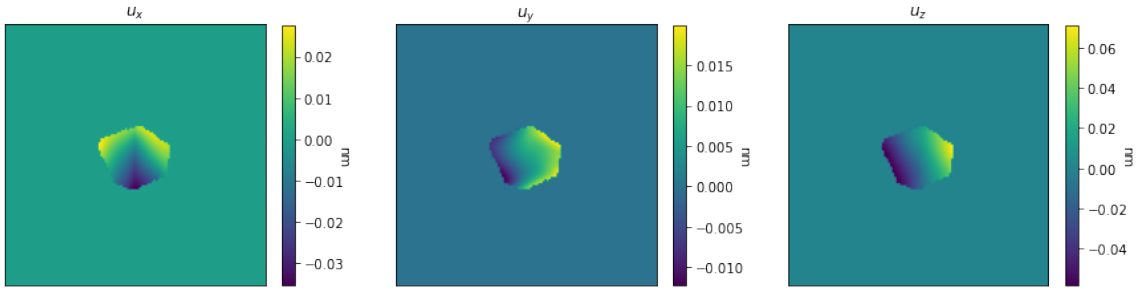


Figure 6.10: Optimized displacement field inferred from MASSIF strain

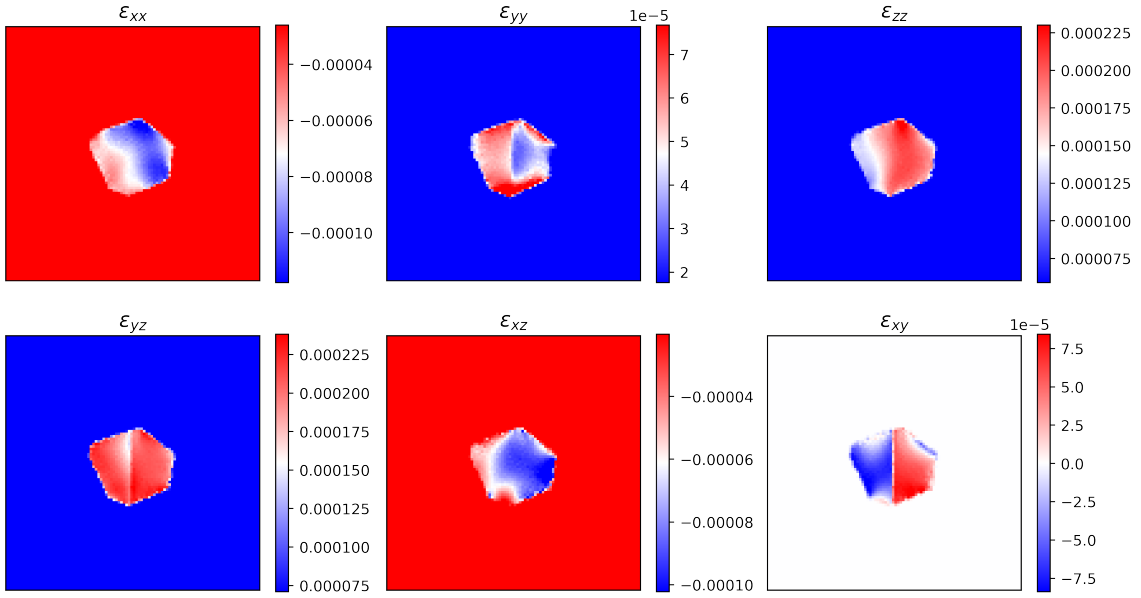


Figure 6.11: Strain field from MASSIF

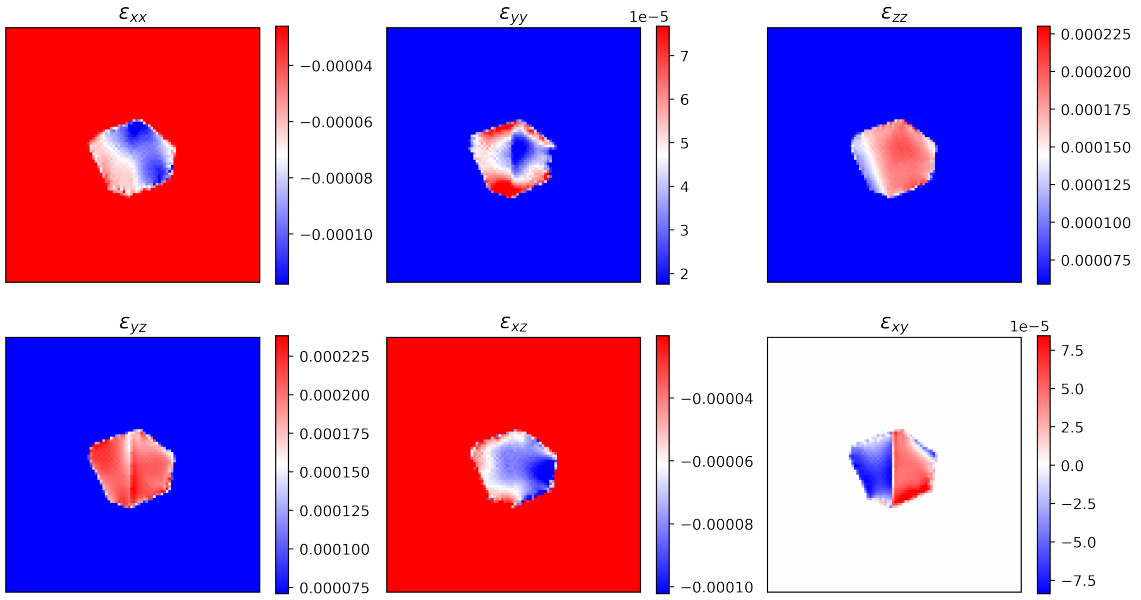


Figure 6.12: Strain field from optimized displacement field. Matches well with MASSIF strain

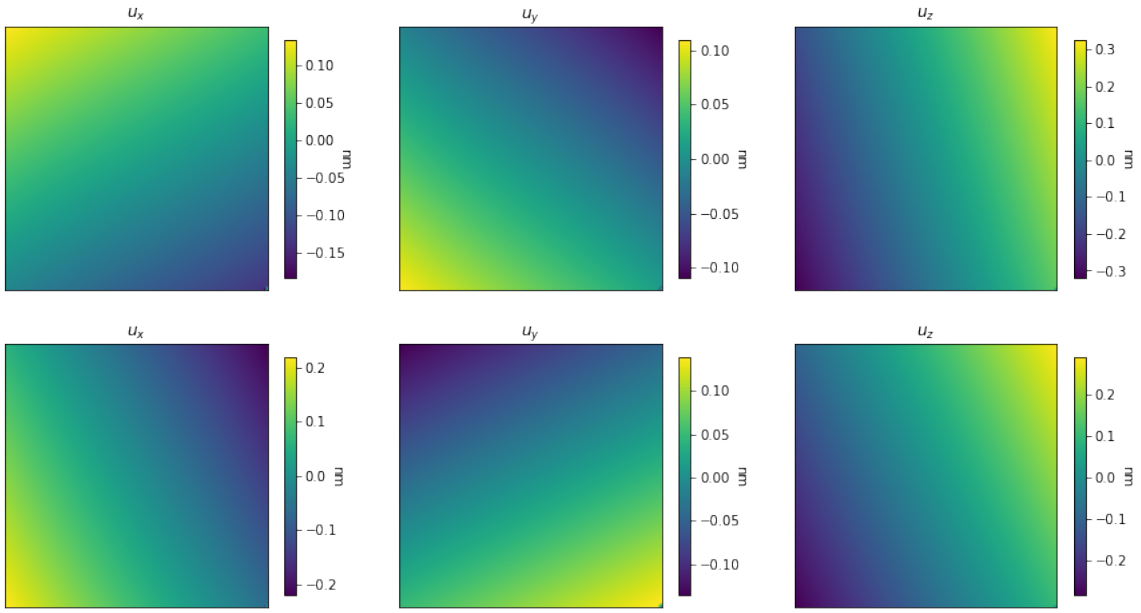


Figure 6.13: Displacement ramps for Grain 1 (top) and Grain 2 (bottom).

The displacement fields were then used to forward-model Bragg peaks for multi-grain BCDI. For the sake of simplicity, the peaks were forward-modeled by taking the FT of the grains in the sample frame, removing the requirement to rotate and interpolate each dataset. As this is a phantom dataset, and the rotation and interpolation steps have been well-documented, this simplification does not subtract meaningfully from the validation. The maximum photon count in each crystal was scaled to $10^6$ and Poisson noise was added. The following CPR recipe was used for the validation reconstructions.

1. 20 iterations of ER
2. 20 iterations of HIO
3. 50 iterations of ER
4. 20 iterations of HIO
5. 50 iterations of ER

This recipe was repeated 5 times. Constituents were combined and shrink-wrap applied every 20 iterations. To determine whether there is benefit to applying the twin-alignment iteratively, two reconstruction scenarios were tested. In the first, the CPR recipe was applied

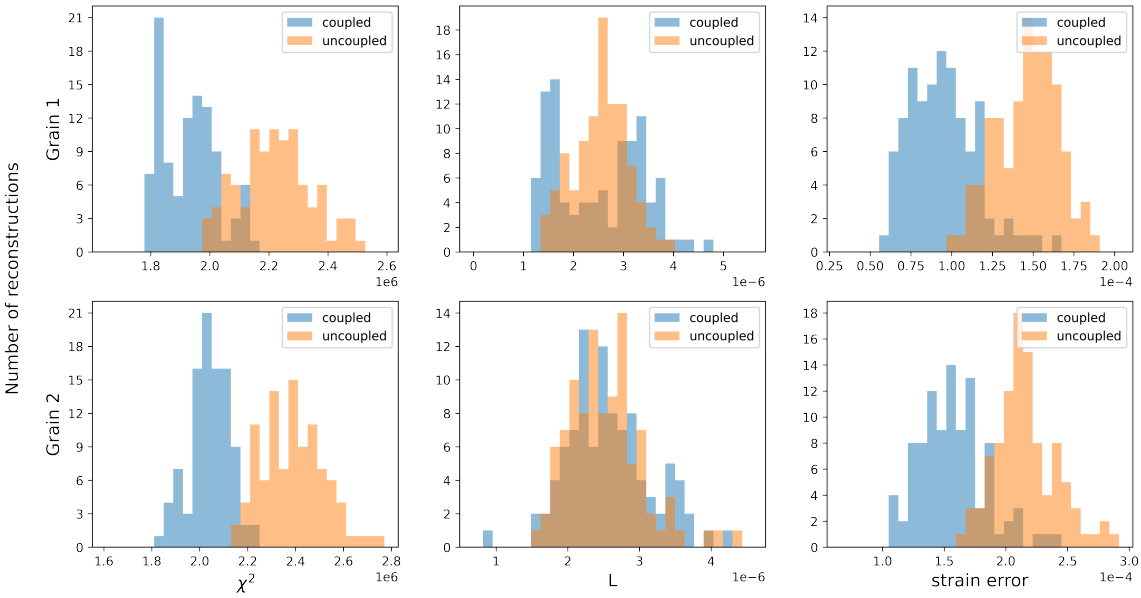


Figure 6.14: Histograms comparing $\chi^2$,$L$, and strain error for 100 reconstructions using the coupled (blue) and uncoupled (orange) techniques. Values for grain 1 are on the top and values for grain 2 are on the bottom. The coupled technique shows marked improvement in both $\chi^2$ and strain error for both grain 1 and grain 2, without sacrificing $L$.

to each grain, and the alignment routine was performed as a post-processing step. This will be called the "uncoupled" approach. In the second, the twin alignment was enforced five times throughout the CPR recipe (after the completion of each recipe segment listed above). this will be called the "coupled" approach. If there is a benefit to coupling two grains during reconstruction, it should appear over the course of 100 reconstructions.

The results of 100 reconstructions using the coupled and uncoupled methods can be seen in Fig. 6.14. The three error metrics show the error between the simulated diffraction pattern and the ground truth ($\chi^2$), the agreement between the $\mathbf{u}$ field and the phases of all constituents in the CPR reconstruction ($L$), and the error between the reconstructed strain fields and the ground truth strain fields (strain error). The strain is used due to the difficulties in centering displacement fields because of the spurious displacement values on the boundary of the reconstructed crystals. By computing the error in the strain fields, we bypass this issue. It can be seen that for both grain 1 and grain 2, $\chi^2$ and the strain error are lower than that for the uncoupled reconstruction, which is as expected. A table showing a comparison of the three error metrics can be seen in 6.1.

The coupled approach shows an improvements of 13.1% for grain 1 and 14.0% for grain

| | coupled grain 1 | uncoupled grain 1 | coupled grain 2 | uncoupled grain 2 |
|---|---|---|---|---|
| $\chi^2$ | $1.93 \times 10^6$ | $2.22 \times 10^6$ | $2.06 \times 10^6$ | $2.39 \times 10^6$ |
| L | $2.57 \times 10^{-6}$ | $2.59 \times 10^{-6}$ | $2.63 \times 10^{-6}$ | $2.53 \times 10^{-6}$ |
| strain error | $9.47 \times 10^{-5}$ | $1.46 \times 10^{-4}$ | $1.59 \times 10^{-4}$ | $2.16 \times 10^{-4}$ |

Table 6.1: Comparison of average error for the coupled and uncoupled reconstruction methods for 100 reconstructions.

2 in $\chi^2$, demonstrating that it minimizes the Fourier space error and steers the constituents in each CPR reconstruction closer to their global minima. It also shows improvements of 35.1% for grain 1 and 26.4% for grain 2 in strain error, demonstrating that it reconstructs the correct real-space strain field more accurately than the uncoupled method. Interestingly, $L$ showed an improvement of 0.6% for grain 1 and a worsening of $-3.0\%$ for grain 2. Because we have the ground truth to compare to, L is less interesting to us here, but it is notable that $L$ does not correlate with better reconstructions as it did in the CPR tests.

### 6.3.2 Preliminary Validation on Experimental Data

A twinned crystal experimental dataset was also collected using a combination of Laue diffraction microscopy and Multi-Peak Bragg Coherent Diffraction Imaging, as shown in chapter IV. The crystals share a [111] twin boundary which is parallel to the laboratory $y$ axis. The central frame of the rotated and interpolated datasets can be seen in Figs 4.6 and 4.7.

Due to the presence of aliens (stray peaks from other crystals which overlap with part of a BCDI dataset), Only four peaks were used from each peak, $[\overline{1}1\overline{1}], [0\overline{2}0], [1\overline{1}1], [11\overline{1}]$ for grain 1 and $[\overline{1}1\overline{1}], [0\overline{2}0], [111], [200]$ for grain 2. While this is not ideal, four Bragg peaks is enough to over-constrain the displacement reconstruction, and should suffice for a preliminary reconstruction. For future reconstructions, these aliens could be removed.

The basic unit of the CPR reconstruction recipe used for each grain was as follows:

1. 20 iterations of ER
2. 10 iterations of HIO
3. 10 iterations of ER

| | coupled | uncoupled |
|---|---|---|
| $\chi^2$ | $1.57 \times 10^9$ | $1.56 \times 10^9$ |
| L | $7.94 \times 10^{-5}$ | $1.36 \times 10^{-4}$ |

Table 6.2: Comparison of average error between the coupled and uncoupled multi-grain reconstruction methods for 10 reconstructions of the the twin-grain experimental data.

This was repeated a total of 70 times, with CPR constituents being combined every 40 iterations (after one of these units). The datasets were reconstructed 10 times using the uncoupled approach and the coupled approach. For the coupled approach, the twin alignment procedure was performed after iterations 400, 800, 1200, 2000, and 2800, and boundary conditions were enforced.

A comparison of the multi-grain reconstruction methods can be seen in Table 6.2. The error metrics have been summed over both grains.

The coupled method decreased $L$ by 41.5% and increased $\chi^2$ by 0.7% compared to the uncoupled method. Ten reconstructions is hardly enough of a sample size to make firm conclusions, and coupled multi-grain reconstruction recipes have not been optimized at this point. Thus, all results reported here are preliminary and require further testing. Nevertheless, the large improvement shown in $L$ between the two methods suggests that intermittently enforcing boundary conditions at the interface of the two grains results in better agreement between the phases and the displacement in each grain. The best two reconstructions from each method can be seen in Fig. 6.15 and the worst reconstructions can be seen in Fig. 6.16. The reconstructions are viewed such that the grain boundary is parallel to the vertical axis in the center of the array.

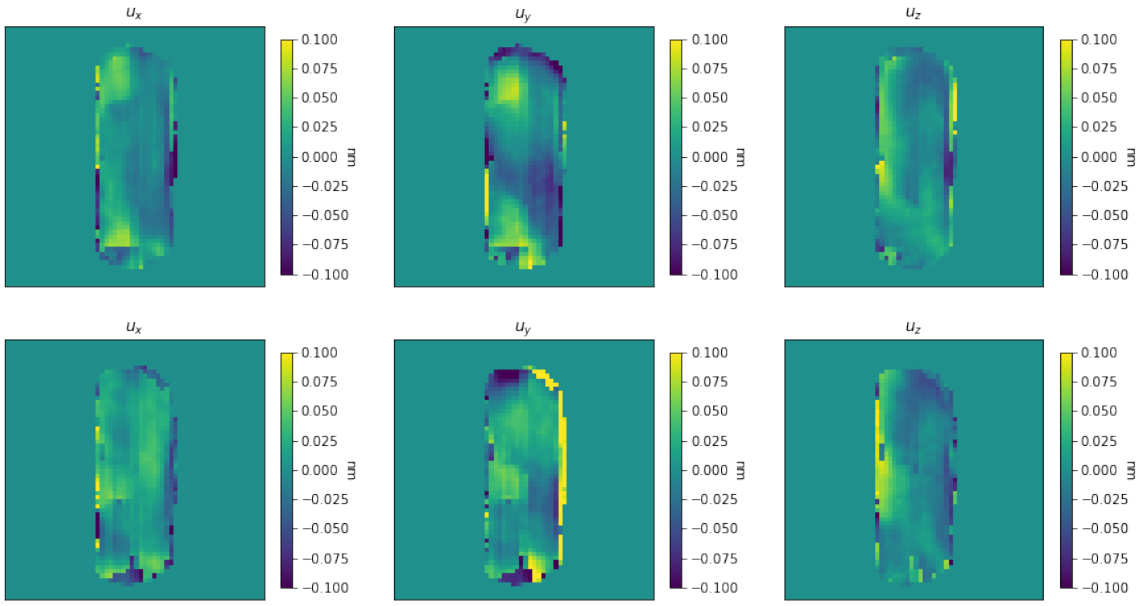


Figure 6.15: Plots of the displacement fields for the best reconstructions using the coupled (top) and uncoupled (bottom) multi-grain reconstruction methods.

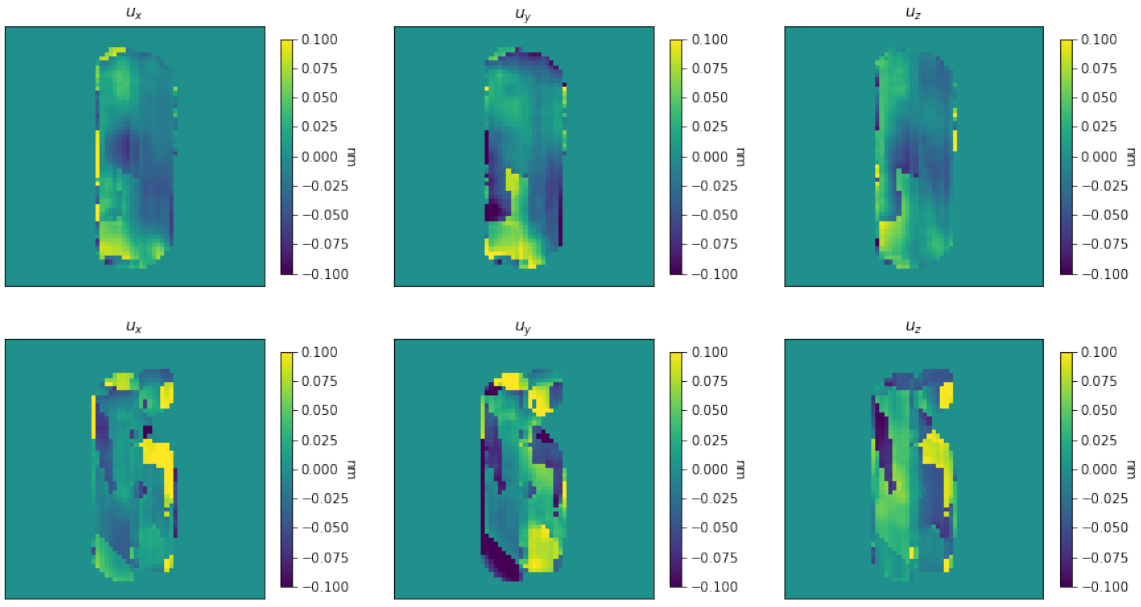


Figure 6.16: Plots of the displacement fields for the worst reconstructions using the coupled (top) and uncoupled (bottom) multi-grain reconstruction methods.

It can be seen that while the best reconstructions contain plausible results, with smoothly varying displacement fields, only the coupled method shows a plausible solution for the worst reconstruction. Displacement fields with large discontinuities like the one seen in Fig. 6.16 were found in five of the ten uncoupled reconstructions.

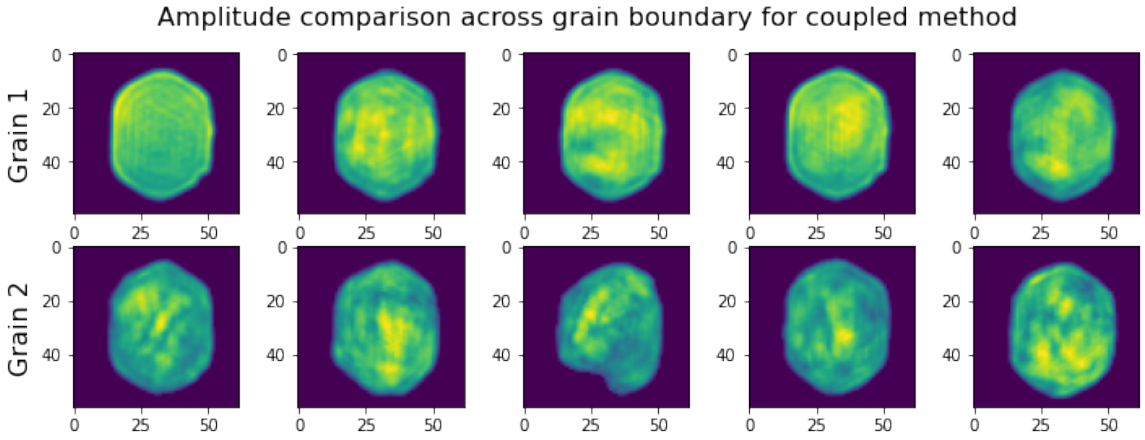


Figure 6.17: Plots of the grain boundary amplitudes for Grain 1 and Grain 2 from five reconstructions using the coupled method.

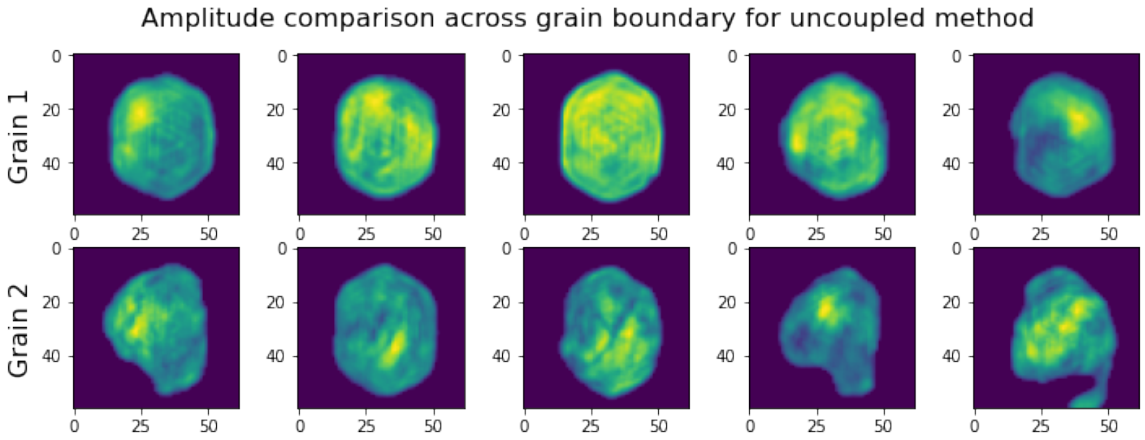


Figure 6.18: Plots of the grain boundary amplitudes for Grain 1 and Grain 2 from five reconstructions using the uncoupled method.

It is also helpful to compare continuity of shape across the grain boundary. This can be most easily seen by looking at the amplitude in the boundary voxels for Grain 1 and Grain 2, as in Figs 6.17 and 6.18. The coupled reconstruction shows more consistent amplitude intensity throughout the grain volume for both grains, typically a sign of a good reconstruction [77]. Additionally, it can be seen that the amplitudes on either side of the boundary match better for the coupled method than the uncoupled method, engendering higher confidence in these reconstructions, as the twin boundary should be shared between the two grains. Finally, a 3D plot of the displacement field from the best reconstruction can be seen in Fig. 6.19. The crystal shapes appear to match up well and there are apparent continuities in displacement visible across the grain boundary.

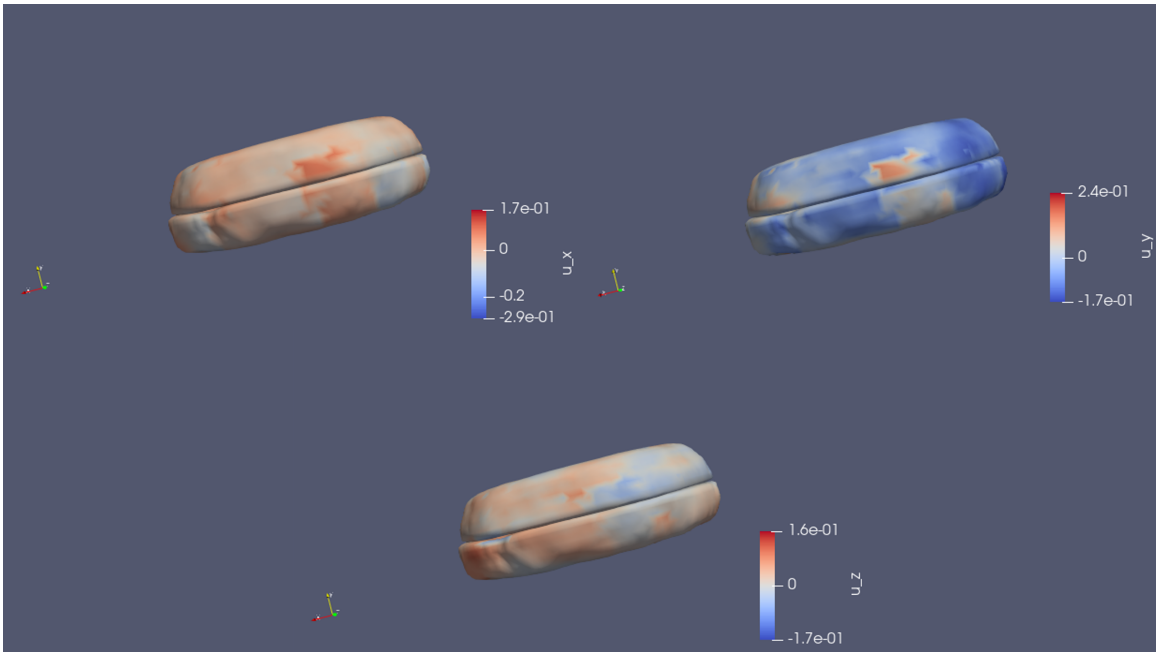


Figure 6.19: Plots of the grain boundary amplitudes for Grain 1 and Grain 2 from five reconstructions using the uncoupled method.

Though these results are preliminary, they suggest a clear improvement in multi-grain reconstruction quality for the coupled method over the uncoupled method.

## 6.4 Discussion

In this work, we demonstrated the first multi-grain alignment technique, which aligns twins along the grain boundary and adjusts the border displacement fields so that they are continuous across the grain boundary. This algorithm is the first of its kind and will hopefully be the foundation on which other BCDI grain alignment procedures are built. We have demonstrated the feasibility of collecting multi-grain datasets with our Au nanocrystalline twin sample. As experimental preparation techniques improve, bi-crystal samples for multi-grain BCDI should be cleaner and less FIB-damaged, allowing for datasets to be collected that are not twins. These datasets will require a different grain boundary identification technique than the one proposed here, but the principle of aligning grains based on continuity of shape and displacement should stand.

The results showed that coupling the reconstructions of multiple grains leads to more accurate reconstructions of each grain. By enforcing a common grain boundary and displace-

ment continuity, extra constraints are provided for phase retrieval, pulling the reconstruction toward the true object. To the author's knowledge, this is the first coupled two-grain reconstruction approach and represents the first step toward a generalized approach on non-twin grains. The method for updating the object support, as well as the method for enforcing displacement continuity should scale to more complicated approaches.

Preliminary reconstructions of experimental data reinforce the claim that reconstruction quality can be improved by coupling reconstruction of multiple grains. Reconstructions using the coupled technique showed improved consistency, showing clear improvement in $L$ though the $\chi^2$ error is virtually indistinguishable from the uncoupled routine. This multi-peak experimental data on twin grains is the first of its kind and work remains to optimize coupled multi-grain reconstruction for experimental data.

For BCDI to become a true polycrystal characterization technique, it will be necessary to reconstruct neighboring grains with high fidelity. Grain boundaries remain a source of many unanswered questions in materials science, and 3D imaging of grain boundary displacements (and thus elastic strains) will be essential to the validation of various theoretical models. With the typical low confidence of boundary voxels in BCDI reconstructions, these studies would be difficult. This routine presents a first step toward high-fidelity two-grain reconstructions, and promises to legitimize BCDI as a microstructure analysis tool.

## 6.5 Code Availability

Both the Multi-Peak and Multi-Grain codes were written in Python and are available on GitHub at https://github.com/mattwilkin/Phaser/tree/coupled_phaser.

# CHAPTER VII

# Future Work

## 7.1 Experimental Methods

### 7.1.1 Multi-Grain BCDI at 1-ID

Future work remains in the development of multi-grain BCDI at 1-ID. Better Pt trench samples must be produced with grains at the scale needed for BCDI. We hypothesize that Pt should twin very readily upon annealing and that there should be a multiplicity of twins in the sample. Using the knowledge that FCC twin misorientation, we can quickly search through the orientation list to locate twin-related grains. We will then attempt to collect BCDI scans from multiple peaks from a parent grain and its twin. After this, the sample will be loaded mechanically through heating. Calculations show that we should be capable of inducing a stress of 400 MPa at temperatures of $\sim 300^{\circ}C$. This will potentially allow us to view strain fields at grain boundaries under compression.

The Multi-Peak experiment described in Chapter IV should be a good baseline to see the extent to which we can deliver a sufficient load to Pt grains in the trench to move dislocations. The multi-peak reconstruction routine requires partial-coherence correction to be able to adequately reconstruct the partially-coherent data collected at 1-ID. Multi-peak reconstructions with partial-coherence correction have not yet been optimized and work must be done to determine optimal reconstruction recipes for partially coherent data. Preliminary reconstructions can be seen in Fig. 7.1.

This is a promising result and it remains to be seen if useful information can be gleaned from reconstructions before and after heating. Nevertheless, the completion of the experiment and the preliminary reconstruction of the data suggests that heating measurements

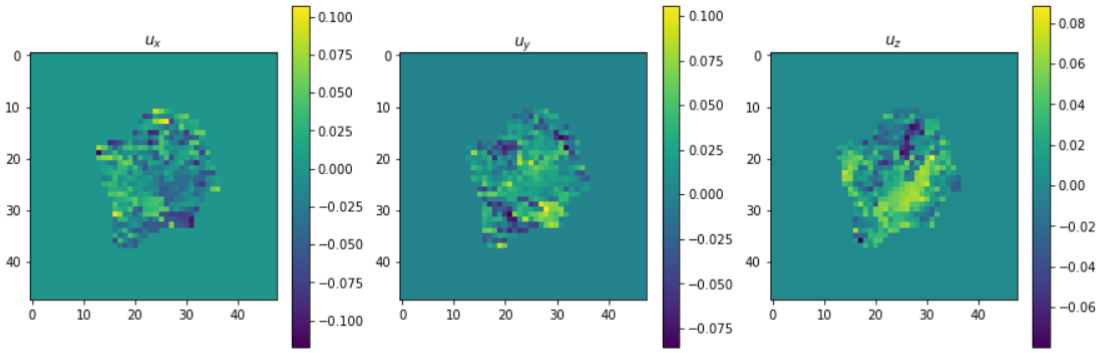


Figure 7.1: Twinned Au nano-crystal on Si substrate. The parent and twin domains were both indexed and measured using BCDI.

can be a success at 1-ID. After the APS-U, the 1-ID beamline should be more well-equipped for BCDI, with significantly improved coherence, allowing for larger grains to be measured and the potential to couple BCDI with other high energy imaging techniques such as Near-field HEDM [93–95].

### 7.1.2 Multi-Grain BCDI 34-ID

Collaboration has begun with a research group at the University of Lorraine to characterize slip transmission across grain boundaries. The group have developed a technique for identifying locations where slip traces cross grain boundaries [96]. We have proposed a novel sample design in which a bi-crystal is cut out of the sample where a slip plane has crossed a grain boundary using a FIB. The final sample will be a pillar with two grains within the coherence length of the 34-ID-C beamline. Early work has been performed on a Cu bicrystal, but it was found that the sample was severely damaged under the FIB. An SEM image of the Cu bi-crystal sample can be seen in 7.2.

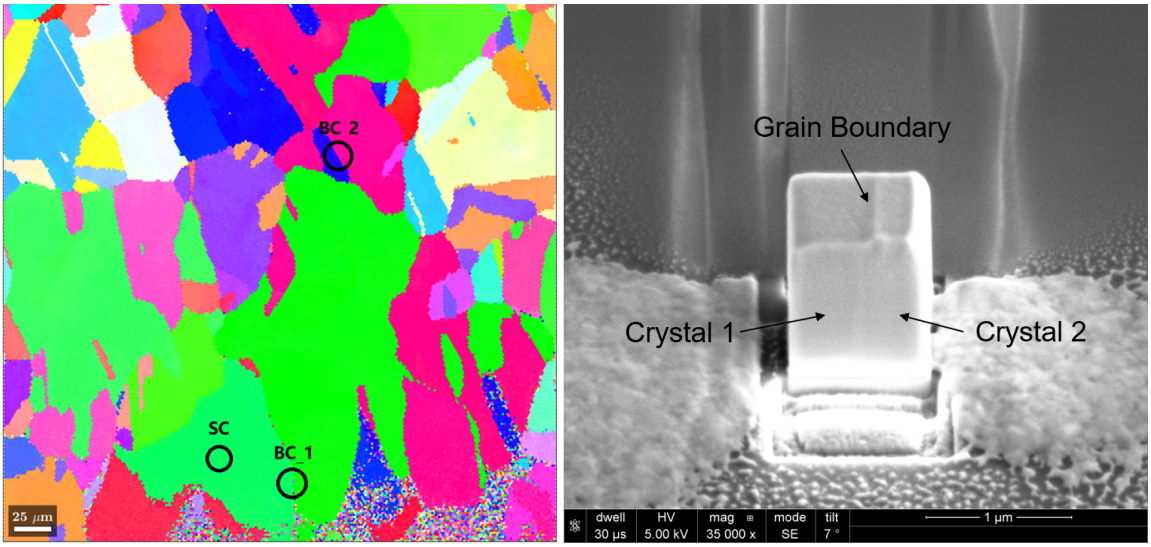


Figure 7.2: FIBed Cu bicrystal sample

We have obtained access to a $\beta$-stabilized Ti sample which has been loaded under uniaxial tension. There are several competing theories as to how $\beta$ Ti behaves under load and we intend to use BCDI to help validate these models. This sample has been examined using a novel EBSD technique and areas of interest have been determined. We will FIB out a pillar around the grain boundary containing the area of interest on either side of the grain boundary. This bi-crystal sample will be placed in the pink beam at 34-ID and the Laue patterns for each crystal will be found, giving us the grain orientations. These orientations will be used to locate multiple Bragg peaks from each grain, and the result will be reconstructed to examine strain fields at the grain boundary, to help validate theoretical plasticity models about slip transmission.

### 7.1.3 Sample Design

Future work remains in sample preparation. Techniques for reducing FIB damage, possibly by milling at lower energies, or performing a FIB polish to the surface of the pillars will potentially preserve crystallinity in the $\beta$ stabilized titanium samples we have received. Additionally, better Pt deposition techniques are being explored, either through lithography or E-beam Pt deposition. Several micrographs also seem to show that the CTE differential between Pt and Si may be too large for proper grain growth to occur in the sample. The Pt appears to be "squeezed" out of the trench in cases where the temperature is significantly

higher than 600 C. Images of a sample annealed at 900 C for 10 h can be seen in 7.3 Based on our calculations, the stress on the Pt at 900 C should be  750 MPa. Solutions are currently being explored to find another substrate material which will reduce compression of the Pt sample and allow for more annealing.

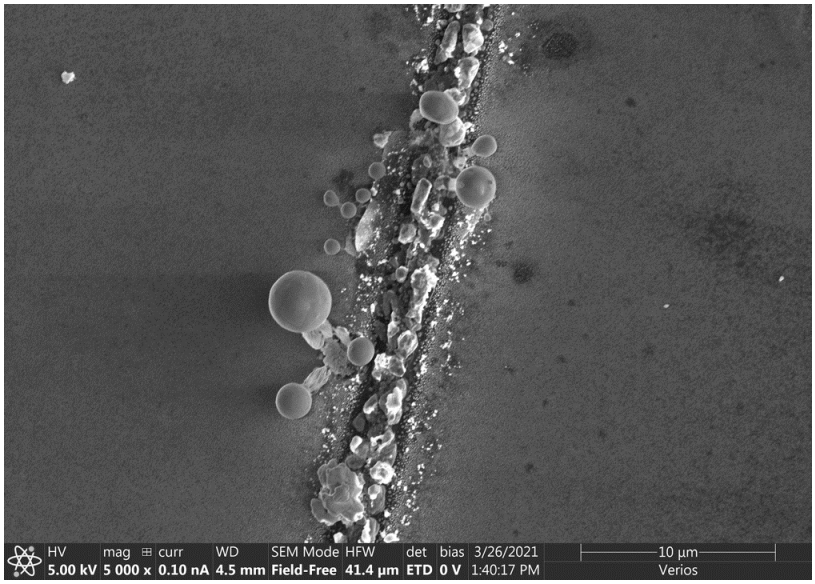


Figure 7.3: Pt trench after annealing at 900 C. The Pt has been pushed out of the trench due to an induced compressive stress of  750 MPa.

## 7.2 Reconstruction Routines

### 7.2.1 Multi-Grain Algorithm Generalization

The Multi-Grain technique is currently designed to reconstruct coherent twins with a completely flat boundary. It was discussed in Chapter  VI that the determination of the grain boundary is the only portion of the routine which limits the general application to all neighboring grains. Work must be done on the image registration to determine which facet of each crystal is the grain boundary facet. After this, the DFT registration and displacement continuity criteria can be used to align the grains, just as in the coherent twin case.

### 7.2.2 CPR-GA Improvements

It would also be helpful to increase the robustness of the GA by including mutation and more complex breeding routines. More diversity could be introduced to the population by breeding randomly, breeding with individuals from previous iterations, or randomly

mutating the displacement fields after each generation. This could prevent the GA from converging too early, where all individuals remain trapped in the same local minimum. The $\chi^2$ error metric could also be normalized by accounting for Poisson noise at each voxel, such that a perfect fit gives a $\chi^2 = 1$. This would make $\chi^2$ a real statistical function. Alternatively, metrics such as the phase retrieval transfer function could be used.

It is possible that the use of $\chi^2$ results in over-fitting, where the reconstructed volume is larger than the actual volume, resulting in extra parameters. Recent work has shown that using free Poisson log likelihood [97] can help prevent over-fitting by setting aside a 'free set' of voxels during application of the modulus constraint during error reduction and HIO, similar to using training and validation sets in data science. Using this method should minimize bias and provide a better estimate of error during CPR.

Partial coherence correction will also need to be accounted for. Two possible paths could be explored: storing partial coherence functions for each data-set during CPR and coupling the partial coherence functions to determine the common function in the lab frame. The first path is relatively simple, requiring only that the current paramters defining the Gaussian partial coherence convolution kernel be passed from iteration to iteration during CPR. The second is more complicated but promises higher potential reward. Partial coherence is a function of the incoming beam, and the 3D partial coherence function could hypothetically be determined from each of the constituent functions during CPR. This would lead to a more accurate partial coherence function and better reconstructions.

## 7.3 Analyzing the Twin-Grain dataset

As discussed in Chapter VI, the multi-grain reconstructions shown in the experimental validation section are preliminary. For multi-peak datasets, we found that a genetic algorithm was needed in order to reconstruct multi-peak datasets consistently. This may well be the case for multi-grain datasets as well. Not enough time has been spent reconstructing the data to be sure that the reconstructions shown in chapter VI are the best possible reconstructions, and work needs to be done to implement phase-unwrapping and partial coherence correction into the routine.

The twin grain dataset could potentially be used to validate theoretical models for grain

boundary stress and strain. It remains to be seen what sort of reconstruction quality can be achieved, but such analysis would be unique, given the resolution of BCDI.

## CHAPTER VIII

# Conclusions

Experimental validation is needed for theoretical models of dislocation transmission at grain boundaries. By providing 3D strain fields with nanometer resolution, multi-grain BCDI promises to provide a window into this phenomenon, potentially revealing accurate strain information around dislocations at grain boundaries. In this work, significant progress, both experimentally and computationally, has been made toward realizing multi-grain BCDI as a viable experimental method. The conclusions of this work are as follows:

1. For multi-grain strain comparison, it is necessary to recover the full strain tensor (via the displacement) in each grain. By adapting a genetic algorithm for reconstructing a single Bragg peak to our coupled algorithm (CPR), we were able to achieve displacement field reconstructions that were more self-consistent in terms of both simulated and experimental data sets, showing improvements of 96.6% in $L$ and 39.2% in $\chi^2$ for simulated data and 53.2% in $L$ and 5.1% in $\chi^2$. This partially supports our first hypothesis, though the improvement in $\chi^2$ was below the 10% prediction. Though not alone in the coupled reconstruction domain, by demonstrating the approach on experimental data, we establish the viability of such approaches for future of coherent x-ray experiments.

2. Reconstructing accurate dislocation displacement fields from multi-peak datasets using coupled phase retrieval methods requires that all constituent reconstructions contain a phase discontinuity in the same location. It was demonstrated that using a genetic algorithm with CPR improved the success rate of dislocation reconstruction by 50% for screw dislocations and 26.7% for edge dislocations, supporting hypothesis

2.

3. It was proposed that reconstructing neighboring grains simultaneously and enforcing boundary conditions in grain shape and displacement could improve reconstruction accuracy and consistency by 10% in all metrics. Analysis on simulated data showed average improvements of 13.5% in $\chi^2$ and 30.8% in strain error, while seeing a worsening of 1.2% in $L$. Preliminary results with experimental data saw an improvement of 41.5% in $L$ and a worsening of 0.7% in $\chi^2$. This Hypothesis was partially supported, with the potential to be fully supported with optimization of multi-grain reconstruction recipes. This work lays the groundwork for future multi-grain BCDI and the study of grain boundaries through coherent x-ray imaging.

# BIBLIOGRAPHY


[1] BESAC. Directing matter and energy: Five challenges for science and the imagination.

[2] BESAC. Science for energy technology: Strengthening the link between basic research and industry.

[3] BESAC. Challenges at the frontiers of matter and energy: Transformative opportunities for discovery science.

[4] BESAC. Basic research needs for transformative manufacturing.

[5] Ian Robinson and Ross Harder. Coherent x-ray diffraction imaging of strain at the nanoscale. *Nature materials*, 8(4):291–298, 2009.

[6] Allison Yau, Wonsuk Cha, Matthew W Kanan, G Brian Stephenson, and Andrew Ulvestad. Bragg coherent diffractive imaging of single-grain defect dynamics in polycrystalline films. *Science*, 356(6339):739–742, 2017.

[7] A Ulvestad, MJ Welland, W Cha, Y Liu, JW Kim, R Harder, E Maxey, JN Clark, MJ Highland, H You, et al. Three-dimensional imaging of dislocation dynamics during the hydriding phase transformation. *Nature materials*, 16(5):565–571, 2017.

[8] V Favre-Nicolin, F Mastropietro, J Eymery, D Camacho, YM Niquet, BM Borg, ME Messing, Lars-Erik Wernersson, RE Algra, EPAM Bakkers, et al. Analysis of strain and stacking faults in single nanowires using bragg coherent diffraction imaging. *New Journal of Physics*, 12(3):035013, 2010.

[9] JN Clark, X Huang, R Harder, and IK Robinson. High-resolution three-dimensional partially coherent diffraction imaging. *Nature communications*, 3(1):1–6, 2012.

[10] Wenge Yang, Xiaojing Huang, Ross Harder, Jesse N Clark, Ian K Robinson, and Ho-kwang Mao. Coherent diffraction imaging of nanoscale strain evolution in a single crystal under high pressure. *Nature communications*, 4(1):1–6, 2013.

[11] Jianwei Miao, Richard L Sandberg, and Changyong Song. Coherent x-ray diffraction imaging. *IEEE Journal of selected topics in quantum electronics*, 18(1):399–410, 2011.

[12] Mathew J Cherukara, Wonsuk Cha, and Ross J Harder. Anisotropic nano-scale resolution in 3d bragg coherent diffraction imaging. *Applied Physics Letters*, 113(20):203101, 2018.

[13] Mathew J. Cherukara, Reeju Pokharel, Timothy S. O'Leary, J. Kevin Baldwin, Evan Maxey, Wonsuk Cha, Jorg Maser, Ross J. Harder, Saryu J. Fensin, and Richard L. Sandberg. Three-dimensional X-ray diffraction imaging of dislocations in polycrystalline metals under tensile loading. *Nature Communications*, 9(1):3776, dec 2018.

[14] Gene E Ice, Ben C Larson, Wenge Yang, John D Budai, Jonathan Zachary Tischler, JWL Pang, RI Barabash, and Wei Liu. Polychromatic x-ray microdiffraction studies of mesoscale structure and dynamics. *Journal of synchrotron radiation*, 12(2):155–162, 2005.

[15] Yu-Feng Shen, S Maddali, D Menasche, A Bhattacharya, GS Rohrer, and RM Suter. Importance of outliers: A three-dimensional study of coarsening in $\alpha$-phase iron. *Physical Review Materials*, 3(6):063611, 2019.

[16] Jin Zhang, Yubin Zhang, Wolfgang Ludwig, David Rowenhorst, Peter W Voorhees, and Henning F Poulsen. Three-dimensional grain growth in pure iron. part i. statistics on the grain level. *Acta Materialia*, 156:76–85, 2018.

[17] TR Bieler, Philip Eisenlohr, Chun Zhang, HJ Phukan, and MA Crimp. Grain boundaries and interfaces in slip transfer. *Current Opinion in Solid State and Materials Science*, 18(4):212–226, 2014.

[18] Bogdan Alexandreanu, Bulent H Sencer, Visit Thaveeprungsriporn, and Gary S Was. The effect of grain boundary character distribution on the high temperature deformation behavior of ni–16cr–9fe alloys. *Acta materialia*, 51(13):3831–3848, 2003.

[19] Michael D Sangid, Tawhid Ezaz, Huseyin Sehitoglu, and Ian M Robertson. Energy of slip transmission and nucleation at grain boundaries. *Acta materialia*, 59(1):283–296, 2011.

[20] CW Zhao, YM Xing, CE Zhou, and PC Bai. Experimental examination of displacement and strain fields in an edge dislocation core. *Acta materialia*, 56(11):2570–2575, 2008.

[21] Siddharth Maddali, Peng Li, Anastasios Pateras, Daniel Timbie, Nazar Delegan, AL Crook, Hope Lee, Irene Calvo-Almazan, Dina Sheyfer, Wonsuk Cha, et al. General approaches for shear-correcting coordinate transformations in bragg coherent diffraction imaging. part i. *Journal of Applied Crystallography*, 53(2), 2020.

[22] Felix Hofmann, Nicholas W Phillips, Ross J Harder, Wenjun Liu, Jesse N Clark, Ian K Robinson, and Brian Abbey. Micro-beam laue alignment of multi-reflection bragg coherent diffraction imaging measurements. *Journal of synchrotron radiation*, 24(5):1048–1055, 2017.

[23] Felix Hofmann, Nicholas W Phillips, Suchandrima Das, Phani Karamched, Gareth M Hughes, James O Douglas, Wonsuk Cha, and Wenjun Liu. Nanoscale imaging of the full strain tensor of specific dislocations extracted from a bulk sample. *Physical Review Materials*, 4(1):013801, 2020.

[24] Marcus Newton. Concurrent phase retrieval for imaging strain in nanocrystals. *Physical Review B-Condensed Matter and Materials Physics*, 2020.

[25] Yuan Gao, Xiaojing Huang, Hanfei Yan, and Garth J Williams. Bragg coherent diffraction imaging by simultaneous reconstruction of multiple diffraction peaks. *Physical Review B*, 103(1):014102, 2021.

[26] Ziyi Wang, Oleg Gorobtsov, and Andrej Singer. An algorithm for bragg coherent x-ray diffractive imaging of highly strained nanocrystals. *New Journal of Physics*, 22(1):013021, 2020.

[27] M. A. Groeber, B. K. Haley, M. D. Uchic, D. M. Dimiduk, and S. Ghosh. 3d reconstruction and characterization of polycrystalline microstructures using a fib-sem system. *Materials Characterization*, 57(4-5):259–273, 2006. Groeber, M. A. Haley, B. K. Uchic, M. D. Dimiduk, D. M. Ghosh, S.

[28] Derek Hull and David J Bacon. *Introduction to dislocations*. Butterworth-Heinemann, 2001.

[29] Peter M Anderson, John P Hirth, and Jens Lothe. *Theory of dislocations*. Cambridge University Press, 2017.

[30] Egon Orowan. Zur kristallplastizität. i. *Zeitschrift für Physik*, 89(9-10):605–613, 1934.

[31] Michael Polanyi. Über eine art gitterstörung, die einen kristall plastisch machen könnte. *Zeitschrift für Physik*, 89(9):660–664, 1934.

[32] Geoffrey Ingram Taylor. The mechanism of plastic deformation of crystals. part i.—theoretical. *Proceedings of the Royal Society of London. Series A, Containing Papers of a Mathematical and Physical Character*, 145(855):362–387, 1934.

[33] JD Livingston and B Chalmers. Multiple slip in bicrystal deformation. *Acta Metallurgica*, 5(6):322–327, 1957.

[34] Z Shen, RH Wagoner, and WAT Clark. Dislocation and grain boundary interactions in metals. *Acta metallurgica*, 36(12):3231–3242, 1988.

[35] Zebang Zheng, Daniel S Balint, and Fionn PE Dunne. Investigation of slip transfer across hcp grain boundaries with application to cold dwell facet fatigue. *Acta Materialia*, 127:43–53, 2017.

[36] Devin W Adams, David T Fullwood, Robert H Wagoner, and Eric R Homer. Atomistic survey of grain boundary-dislocation interactions in fcc nickel. *Computational Materials Science*, 164:171–185, 2019.

[37] Dimitry Terentyev, Alexander Bakaev, A Serra, F Pavia, KL Baker, and N Anento. Grain boundary mediated plasticity: The role of grain boundary atomic structure and thermal activation. *Scripta Materialia*, 145:1–4, 2018.

[38] Ian K Robinson, Ivan A Vartanyants, GJ Williams, MA Pfeifer, and JA Pitney. Reconstruction of the shapes of gold nanocrystals using coherent x-ray diffraction. *Physical review letters*, 87(19):195505, 2001.

[39] David Sayre. Some implications of a theorem due to shannon. *Acta Crystallographica*, 5(6):843–843, 1952.

[40] C.E. Shannon. *Prec. Inst. Radio Engrs.*, 37:10, 1949.

[41] Jianwei Miao, David Sayre, and HN Chapman. Phase retrieval from the magnitude of the fourier transforms of nonperiodic objects. *JOSA A*, 15(6):1662–1669, 1998.

[42] Jianwei Miao and David Sayre. On possible extensions of x-ray crystallography through diffraction-pattern oversampling. *Acta Crystallographica Section A: Foundations of Crystallography*, 56(6):596–605, 2000.

[43] Ralph W Gerchberg. A practical algorithm for the determination of phase from image and diffraction plane pictures. *Optik*, 35:237–246, 1972.

[44] James R Fienup. Reconstruction of an object from the modulus of its fourier transform. *Optics letters*, 3(1):27–29, 1978.

[45] James R Fienup. Phase retrieval algorithms: a comparison. *Applied optics*, 21(15):2758–2769, 1982.

[46] Stefano Marchesini, H He, Henry N Chapman, Stefan P Hau-Riege, Aleksandr Noy, Malcolm R Howells, Uwe Weierstall, and John CH Spence. X-ray image reconstruction from a diffraction pattern alone. *Physical Review B*, 68(14):140101, 2003.

[47] Stefano Marchesini. Invited article: A unified evaluation of iterative projection algorithms for phase retrieval. *Review of scientific instruments*, 78(1):011301, 2007.

[48] James R Fienup. Reconstruction of a complex-valued object from the modulus of its fourier transform using a support constraint. *JOSA A*, 4(1):118–123, 1987.

[49] HD Coughlan, C Darmanin, NW Phillips, F Hofmann, JN Clark, RJ Harder, DJ Vine, and B Abbey. Radiation damage in a micron-sized protein crystal studied via reciprocal space mapping and bragg coherent diffractive imaging. *Structural Dynamics*, 2(4):041704, 2015.

[50] HD Coughlan, C Darmanin, HJ Kirkwood, NW Phillips, D Hoxley, JN Clark, DJ Vine, F Hofmann, RJ Harder, E Maxey, et al. Bragg coherent diffraction imaging and metrics for radiation damage in protein micro-crystallography. *Journal of synchrotron radiation*, 24(1):83–94, 2017.

[51] Stéphane Labat, Marie-Ingrid Richard, Maxime Dupraz, Marc Gailhanou, Guillaume Beutier, Marc Verdier, Francesca Mastropietro, Thomas W Cornelius, Tobias U Schulli, Joel Eymery, et al. Inversion domain boundaries in gan wires revealed by coherent bragg imaging. *ACS nano*, 9(9):9210–9216, 2015.

[52] Andrew Ulvestad, Kiran Sasikumar, Jong Woo Kim, Ross Harder, Evan Maxey, Jesse N Clark, Badri Narayanan, Sanket A Deshmukh, Nicola Ferrier, Paul Mulvaney, et al. In situ 3d imaging of catalysis induced strain in gold nanoparticles. *The journal of physical chemistry letters*, 7(15):3008–3013, 2016.

[53] Dongjin Kim, Myungwoo Chung, Jerome Carnis, Sungwon Kim, Kyuseok Yun, Jinback Kang, Wonsuk Cha, Mathew J Cherukara, Evan Maxey, Ross Harder, et al. Active site localization of methane oxidation on pt nanocrystals. *Nature communications*, 9(1):1–7, 2018.

[54] Johannes Ihli, Jesse N Clark, Alexander S Côté, Yi-Yeoun Kim, Anna S Schenk, Alexander N Kulak, Timothy P Comyn, Oliver Chammas, Ross J Harder, Dorothy M Duffy, et al. Strain-relief by single dislocation loops in calcite crystals grown on self-assembled monolayers. *Nature communications*, 7(1):1–8, 2016.

[55] Ana Katrina C Estandarte, Christopher Michael Lynch, Marianne Monteforte, Jonathan Rawle, Chris Nicklin, and Ian Robinson. Bragg coherent diffraction imaging of iron diffusion into gold nanocrystals. *New Journal of Physics*, 20(11):113026, 2018.

[56] Felix Hofmann, Edmund Tarleton, Ross J Harder, Nicholas W Phillips, Pui-Wai Ma, Jesse N Clark, Ian K Robinson, Brian Abbey, Wenjun Liu, and Christian E Beck. 3d lattice distortions and defect structures in ion-implanted nano-crystals. *Scientific reports*, 7(1):1–10, 2017.

[57] Marcus C Newton, Steven J Leake, Ross Harder, and Ian K Robinson. Three-dimensional imaging of strain in a single zno nanorod. *Nature materials*, 9(2):120–124, 2010.

[58] Joel V Bernier, Robert M Suter, Anthony D Rollett, and Jonathan D Almer. High-energy x-ray diffraction microscopy in materials science. *Annual Review of Materials Research*, 50:395–436, 2020.

[59] Aditi Bhattacharya, Yu-Feng Shen, Christopher M Hefferan, Shiu Fai Li, Jonathan Lind, Robert M Suter, and Gregory S Rohrer. Three-dimensional observations of grain volume changes during annealing of polycrystalline ni. *Acta Materialia*, 167:40–50, 2019.

[60] Siddharth Maddali, Marc Allain, Wonsuk Cha, Ross Harder, J-S Park, Peter Kenesei, Jonathan Almer, Youssef Nashed, and Stephan O Hruszkewycz. Phase retrieval for bragg coherent diffraction imaging at high x-ray energies. *Physical Review A*, 99(5):053838, 2019.

[61] Siddharth Maddali, J-S Park, Hemant Sharma, Sarvjit Shastri, Peter Kenesei, Jonathan Almer, Ross Harder, Matthew J Highland, Y Nashed, and Stephan O Hruszkewycz. High-energy coherent x-ray diffraction microscopy of polycrystal grains: Steps toward a multiscale approach. *Physical Review Applied*, 14(2):024085, 2020.

[62] Wenjun Liu, Gene E Ice, Bennett C Larson, Wenge Yang, Jonathan Z Tischler, and JOHN D Budai. The three-dimensional x-ray crystal microscope: A new tool for materials characterization. *Metallurgical and Materials Transactions A*, 35(7):1963–1967, 2004.

[63] Wenjun Liu and Gene E Ice. X-ray laue diffraction microscopy in 3d at the advanced photon source. In *Strain And Dislocation Gradients From Diffraction: Spatially-resolved Local Structure And Defects*, pages 53–81. World Scientific, 2014.

[64] James R Weaver. Centrosymmetric (cross-symmetric) matrices, their basic properties, eigenvalues, and eigenvectors. *The American Mathematical Monthly*, 92(10):711–717, 1985.

[65] Marc A Meyers and Lawrence E Murr. A model for the formation of annealing twins in fcc metals and alloys. *Acta metallurgica*, 26(6):951–962, 1978.

[66] H Gleiter. The formation of annealing twins. *Acta metallurgica*, 17(12):1421–1428, 1969.

[67] S Mahajan, CS Pande, MA Imam, and BB Rath. Formation of annealing twins in fcc crystals. *Acta materialia*, 45(6):2633–2638, 1997.

[68] Anastasios Pateras, Ross Harder, Wonsuk Cha, Jonathan G. Gigax, J. Kevin Baldwin, Jon Tischler, Ruqing Xu, Wenjun Liu, Mark J. Erdmann, Robert Kalt, Richard L. Sandberg, Saryu Fensin, and Reeju Pokharel. Combining Laue diffraction with Bragg coherent diffraction imaging at 34-ID-C. *Journal of Synchrotron Radiation*, 27(5):1430–1437, sep 2020.

[69] Anastasios Pateras, Ross Harder, Wonsuk Cha, Jonathan G Gigax, J Kevin Baldwin, Jon Tischler, Ruqing Xu, Wenjun Liu, Mark J Erdmann, Robert Kalt, et al. Combining laue diffraction with bragg coherent diffraction imaging at 34-id-c. *arXiv preprint arXiv:2002.11859*, 2020.

[70] Claudia Manuela Müller and Ralph Spolenak. Dewetting of au and aupt alloy films: a dewetting zone model. *Journal of Applied Physics*, 113(9):094301, 2013.

[71] Hiromichi Watanabe, Naofumi Yamada, and Masahiro Okaji. Linear thermal expansion coefficient of silicon from 293 to 1000 k. *International journal of thermophysics*, 25(1):221–236, 2004.

[72] David R Lide. *CRC handbook of chemistry and physics*, volume 85. CRC press, 2004.

[73] Ricardo A Lebensohn, Anand K Kanjarla, and Philip Eisenlohr. An elasto-viscoplastic formulation based on fast fourier transforms for the prediction of micromechanical fields in polycrystalline materials. *International Journal of Plasticity*, 32:59–69, 2012.

[74] Siddharth Maddali, Irene Calvo-Almazan, Jonathan Almer, Peter Kenesei, J-S Park, Ross Harder, Youssef Nashed, and SO Hruszkewycz. Sparse recovery of undersampled intensity patterns for coherent diffraction imaging at high x-ray energies. *Scientific reports*, 8(1):1–10, 2018.

[75] Nicolas Burdet, Xiaowen Shi, Daniel Parks, Jesse N Clark, Xiaojing Huang, Stephen D Kevan, and Ian K Robinson. Evaluation of partial coherence correction in x-ray ptychography. *Optics express*, 23(5):5452–5467, 2015.

[76] Matthew J Wilkin, Siddharth Maddali, Stephan O Hruszkewycz, Anastasios Pateras, Richard L Sandberg, Ross Harder, Wonsuk Cha, Robert M Suter, and Anthony D Rollett. Experimental demonstration of coupled multi-peak bragg coherent diffraction imaging with genetic algorithms. *Physical Review B*, 103(21):214103, 2021.

[77] A Ulvestad, Y Nashed, Guillaume Beutier, M Verdier, SO Hruszkewycz, and M Dupraz. Identifying defects with guided algorithms in bragg coherent diffractive imaging. *Scientific reports*, 7(1):1–9, 2017.

[78] Manuel Guizar-Sicairos and James R Fienup. Understanding the twin-image problem in phase retrieval. *JOSA A*, 29(11):2367–2375, 2012.

[79] C C Chen, J Miao, C W Wang, and T K Lee. Application of optimization technique to noncrystalline x-ray diffraction microscopy: Guided hybrid input-output method. *Physical Review B*, 76(6):64113, 2007.

[80] Jesse N Clark, Johannes Ihli, Anna S Schenk, Yi-Yeoun Kim, Alexander N Kulak, James M Campbell, Gareth Nisbet, Fiona C Meldrum, and Ian K Robinson. Three-dimensional imaging of dislocation propagation during crystal growth and dissolution. *Nature materials*, 14(8):780–784, 2015.

[81] Theron M Rodgers, Jonathan D Madison, and Veena Tikare. Simulation of metal additive manufacturing microstructures using kinetic monte carlo. *Computational Materials Science*, 135:78–89, 2017.

[82] Siddharth Maddali. Phaser: Python-based bcdi phase retrieval for cpu and gpu, dec 2020.

[83] Randy L Haupt and Sue Ellen Haupt. *Practical genetic algorithms*. John Wiley & Sons, 2004.

[84] FRN Nabarro. Theory of crystal dislocations dover publications. *Inc., New York*, 264, 1987.

[85] Cristian Teodosiu. The elastic field of point defects. In *Elastic Models of Crystal Defects*, pages 287–316. Springer, 1982.

[86] Andrew Ulvestad, Jesse N Clark, Ross Harder, Ian K Robinson, and Oleg G Shpyrko. 3d imaging of twin domain defects in gold nanoparticles. *Nano letters*, 15(6):4066–4070, 2015.

[87] Jérôme Carnis, Aseem Rajan Kshirsagar, Longfei Wu, Maxime Dupraz, Stéphane Labat, Michaël Texier, Luc Favre, Lu Gao, Freddy E Oropeza, Nimrod Gazit, et al. Twin boundary migration in an individual platinum nanocrystal during catalytic co oxidation. *Nature communications*, 12(1):1–10, 2021.

[88] Morton E Gurtin. *An introduction to continuum mechanics*. Academic press, 1982.

[89] Martin H Sadd. *Elasticity: theory, applications, and numerics*. Academic Press, 2009.

[90] Manuel Guizar-Sicairos, Samuel T Thurman, and James R Fienup. Efficient subpixel image registration algorithms. *Optics letters*, 33(2):156–158, 2008.

[91] Ricardo A Lebensohn and CN Tomé. A self-consistent anisotropic approach for the simulation of plastic deformation and texture development of polycrystals: application to zirconium alloys. *Acta metallurgica et materialia*, 41(9):2611–2624, 1993.

[92] Diederik P Kingma, Shakir Mohamed, Danilo Jimenez Rezende, and Max Welling. Semi-supervised learning with deep generative models. In *Advances in neural information processing systems*, pages 3581–3589, 2014.

[93] Yu-Feng Shen, He Liu, and Robert M Suter. Voxel-based strain tensors from near-field high energy diffraction microscopy. *Current Opinion in Solid State and Materials Science*, 24(4):100852, 2020.

[94] Kelly E Nygren, Darren C Pagan, Joel V Bernier, and Matthew P Miller. An algorithm for resolving intragranular orientation fields using coupled far-field and near-field high energy x-ray diffraction microscopy. *Materials Characterization*, 165:110366, 2020.

[95] Aditi Bhattacharya, Yu-Feng Shen, Christopher M Hefferan, Shiu Fai Li, Jonathan Lind, Robert M Suter, Carl E Krill III, and Gregory S Rohrer. Grain boundary velocity and curvature are not correlated in ni polycrystals. *Science*, 374(6564):189–193, 2021.

[96] Meriem Ben Haj Slama, Vincent Taupin, Nabila Maloufi, Kaustubh Venkatraman, Anthony D Rollett, Ricardo A Lebensohn, Stephane Berbenni, Benoît Beausir, and Antoine Guitton. Electron channeling contrast imaging characterization and crystal plasticity modelling of dislocation activity in ti21s bcc material. *Materialia*, 15:100996, 2021.

[97] Vincent Favre-Nicolin, Steven Leake, and Yuriy Chushkin. Free log-likelihood as an unbiased metric for coherent diffraction imaging. *Scientific reports*, 10(1):1–8, 2020.